APPLIED COMPUTATIONAL ELECTROMAGNETICS SOCIETY JOURNAL

December 2017
Vol. 32 No. 12
ISSN 1054-4887

The ACES Journal is abstracted in INSPEC, in Engineering Index, DTIC, Science Citation Index Expanded, the Research Alert, and to Current Contents/Engineering, Computing & Technology.

The illustrations on the front cover have been obtained from the research groups at the Department of Electrical Engineering, The University of Mississippi.

THE APPLIED COMPUTATIONAL ELECTROMAGNETICS SOCIETY
http://aces-society.org

EDITORS-IN-CHIEF

Atef Elsherbeni
Colorado School of Mines, EE Dept.
Golden, CO 80401, USA

Sami Barmada
University of Pisa, ESE Dept.
56122 Pisa, Italy

ASSOCIATE EDITORS-IN-CHIEF: REGULAR PAPERS

Mohammed Hadi
Kuwait University, EE Dept.
Safat, Kuwait

Alistair Duffy
De Montfort University
Leicester, UK

Wenxing Li
Harbin Engineering University
Harbin 150001, China

Maokun Li
Tsinghua University
Beijing 100084, China

Antonio Musolino
University of Pisa
56126 Pisa, Italy

Abdul Arkadan
Marquette University, ECE Dept.
Milwaukee, WI 53201, USA

Salvatore Campione
Sandia National Laboratories
Albuquerque, NM 87185, USA

Marco Arjona López
La Laguna Institute of Technology
Torreon, Coahuila 27266, Mexico

Paolo Mezzanotte
University of Perugia
I-06125 Perugia, Italy

Luca Di Rienzo
Politecnico di Milano
20133 Milano, Italy

Rocco Rizzo
University of Pisa
56123 Pisa, Italy

ASSOCIATE EDITORS-IN-CHIEF: EXPRESS PAPERS

Lijun Jiang
University of Hong Kong, Dept. of EEE
Hong, Kong

Shinichiro Ohnuki
Nihon University
Tokyo, Japan

Kubilay Sertel
The Ohio State University
Columbus, OH 43210, USA

Steve J. Weiss
US Army Research Laboratory
Adelphi Laboratory Center (RDRL-SER-M)
Adelphi, MD 20783, USA

William O'Keefe Coburn
US Army Research Laboratory
Adelphi Laboratory Center (RDRL-SER-M)
Adelphi, MD 20783, USA

Jiming Song
Iowa State University, ECE Dept.
Ames, IA 50011, USA

Amedeo Capozzoli
Univerita di Napoli Federico II, DIETI
I-80125 Napoli, Italy

Yu Mao Wu
Fudan University
Shanghai 200433, China

Maokun Li
Tsinghua University, EE Dept.
Beijing 100084, China

EDITORIAL ASSISTANTS

Matthew J. Inman
University of Mississippi, Electrical Engineering Dept.
University, MS 38677, USA

Shanell Lopez
Colorado School of Mines, Electrical Engineering Dept.
Golden, CO 80401, USA

EMERITUS EDITORS-IN-CHIEF

Duncan C. Baker
EE Dept. U. of Pretoria
0002 Pretoria, South Africa

Robert M. Bevensee
Box 812
Alamo, CA 94507-0516, USA

Allen Glisson
University of Mississippi, EE Dept.
University, MS 38677, USA

Ozlem Kilic
Catholic University of America
Washington, DC 20064, USA

Ahmed Kishk
Concordia University, ECS Dept.
Montreal, QC H3G 1M8, Canada

David E. Stein
USAF Scientific Advisory Board
Washington, DC 20330, USA

EMERITUS ASSOCIATE EDITORS-IN-CHIEF

Yasushi Kanai
Niigata Inst. of Technology
Kashiwazaki, Japan

Levent Gurel
Bilkent University
Ankara, Turkey

Erdem Topsakal
Mississippi State University, EE Dept.
Mississippi State, MS 39762, USA

Mohamed Abouzahra
MIT Lincoln Laboratory
Lexington, MA, USA

Sami Barmada
University of Pisa, ESE Dept.
56122 Pisa, Italy

Alexander Yakovlev
University of Mississippi, EE Dept.
University, MS 38677, USA

Ozlem Kilic
Catholic University of America
Washington, DC 20064, USA

Fan Yang
Tsinghua University, EE Dept.
Beijing 100084, China

EMERITUS EDITORIAL ASSISTANTS

Khaled ElMaghoub
Trimble Navigation/MIT
Boston, MA 02125, USA

Anne Graham
University of Mississippi, EE Dept.
University, MS 38677, USA

Christina Bonnington
University of Mississippi, EE Dept.
University, MS 38677, USA

Mohamed Al Sharkawy
Arab Academy for Science and Technology, ECE Dept.
Alexandria, Egypt

DECEMBER 2017 REVIEWERS: REGULAR PAPERS

Shakil Ahmed
Rajesh Elangovan
Grant Ellis
Long Li
Yasser Madany
Samir Mahmoud
Peyman Mahouti
Xiao-Min Pan
Xuewei Ping
Jean Piou
Azhagumurugan R.
Anand R.
Ashish Singh
Varun Singh
Wenhua Yu

DECEMBER 2017 REVIEWERS: EXPRESS PAPERS

Shahid Ahmed
Volkan Akan
David Chen
William Coburn
Alistar Duffy
Yunus Erdemli
Alessandro Fanti
Randy Haupt
Maokun Li
Lifford McLauchlan
Pejman Rezaei
Rashid Saleem
Katherine Siakavara
Ashish Singh
Steven Weiss
Yu Mao Wu
Bo Zhao

THE APPLIED COMPUTATIONAL ELECTROMAGNETICS SOCIETY JOURNAL

Vol. 32 No. 12 December 2017

TABLE OF CONTENTS – REGULAR PAPERS

TABLE OF CONTENTS – EXPRESS PAPERS

Advanced Statistical 3D Models of Composite Materials for Microwave Electromagnetic Compatibility Applications

Sébastien Lalléchère

Université Clermont Auvergne, CNRS, SIGMA Clermont, Institut Pascal, 4 av Blaise Pascal, F-63178 Aubière
sebastien.lallechere@uca.fr

Abstract **─** This article describes advanced tridimensional time domain tools for characterizing composite structures in EMC context. Because of current high interests from industrial areas (e.g., automotive, and/or aerospace), many domains are demanding for reliable and accurate numerical tools to characterize such materials. In this framework, a particular care is granted to mixing theories. This article will demonstrate the interest of trustworthy statistical tools to check at the same time the validity of electromagnetic mixing rules and to realistically calibrate these models.

Index Terms **─** Composite material, computational electromagnetics, electromagnetic compatibility, shielding effectiveness, time domain modeling.

I. INTRODUCTION

Composite materials are being extensively used for almost fifteen years in various areas such as transport (for instance automotive, aerospace, railway) [1, 2], communication [3], and energy [2]. Due to increasing environmental constraints (e.g., regarding sources of perturbations: crosstalk, grounding [1], lightning [2], wireless communication [3]), ElectroMagnetic Compatibility (EMC) requirements are more and more demanding for accurate and efficient characterization (with experimental and/or numerical tools) of these mixed materials. In this framework, many studies were proposed to model shielding performances of reinforced materials including enclosures with composite thin sheet: for instance based upon Finite Element Method (FEM) technique [4], Discontinuous Galerkin Method (DGM) [5], or experimental device with carbon-nanostructured composites in [6]. It is to be noted that relevant modeling processes are needed in that context, especially relying on time domain methods [7]. Indeed, on the one hand, since composites made of resin matrix and high strength fibers (e.g., carbon, graphite, glass) are widely spread in different industrial domains such as automotive [1], and aerospace and wind energy [2], they require particular care for electrical safety and functioning reasons. On the other hand, assuming the conductivity and sizes of inclusions leads to competitive numerical issues. Indeed, a priori weakly conducting particles are considered in comparison to purely metallic shields, and high scaling factors are observed since the sizes of inclusions are in between 10^5 and 10^7 times smaller than EMC systems. That is why mixing rules (part of Electromagnetic Mixing Theory, EMT) have been recently widely used for statistical developments [8] and numerical works [9-12] to characterize the effective permittivity of composite mixtures for different applications from scattering [8] to EMC [5-7, 9, 10] throughout metrology [11, 12]. They are mainly based upon classical unified mixing rule [8-10] with different variations as developed in Section II. The first aim of this contribution is to demonstrate the interest of a tridimensional (3D) time domain automated (with Matlab®) tool based upon Finite Integration Technique (FIT, CST®) for the assessment of the electromagnetic attenuation (by computing Shielding Effectiveness, SE) of biphasic mixed materials. It is to be noted at that stage, that SE data will be computed from T-solver (time domain FIT) simulations; although final data are depicted in frequency domain (from Fast Fourier Transformation, FFT). The second objective is to provide first-orders statistical moments (i.e., mean and standard deviation, std) of SE to face equivalent homogeneous approaches (e.g., from Maxwell-Garnett, MG [8] or Dynamic Homogenization Method, DHM [9]) with proposed numerical modeling. This proposal is divided into four sections following introductory part I: Section II details theoretical foundations from mixing rules, whereas Section III provides information regarding the automated numerical procedure relying on time domain FIT method. Finally, numerical results are given in Section IV, both validating our methodology and successfully comparing it with advanced EMTs (e.g., DHM). Some concluding remarks are provided in last Section V.

II. THEORETICAL BASIS

Mixing equations such as Maxwell-Garnet (MG), Bruggeman-Rule (BR), or coherent potential rule [8, 9] are wide spread and useful formalisms to avoid costly 3D

Submitted On: October 23, 2016
Accepted On: January 18, 2017

numerical models. In this article, we will focus on particular case of biphasic composite materials (two phases *i*=1 or 2, respectively for matrix and conducting inclusions; volumetric fractions are respectively given in the following by η=1-ν and ν). For spherical inclusions, the classical formulation involves a depolarization 3x3 tensor $\boldsymbol{N}$, such as N is a diagonal matrix holding the Cartesian terms $(N_u)^T$, where N_u=1/3 (u=x, y, or z) as discussed in [13]. Relying on terms in relation (1), the effective homogenized complex permittivity ϵ_u in Cartesian direction u (x, y, or z) is given in [9] by:

$$\varepsilon_u = \frac{\varepsilon_1 \frac{1-\nu}{\varepsilon_\infty + N_u(\varepsilon_1 - \varepsilon_\infty)} + \varepsilon_2 \frac{\nu}{\varepsilon_\infty + N_u(\varepsilon_2 - \varepsilon_\infty)}}{\frac{1-\nu}{\varepsilon_\infty + N_u(\varepsilon_1 - \varepsilon_\infty)} + \frac{\nu}{\varepsilon_\infty + N_u(\varepsilon_2 - \varepsilon_\infty)}}, \tag{1}$$

where ε_∞ represents the complex permittivity of the infinite medium. It is to be noted that according to numerical test case proposed in [9, 13], the material will be assumed to be low-loss (i.e., depending on real permittivity and conductivity of the material). Without any loss of generality, any kind of material may be taken into account through ε_∞ parameter (e.g., Debye frequency dispersive material as in [7]). The assumption $\varepsilon_\infty = \varepsilon_1$ in relation (2) leads to the classical MG formulation, whereas DHM [9] offers to take into account the effect of the size of inclusions by defining $\varepsilon_\infty = \varepsilon_1 + \varepsilon_2 (d/\lambda)^\alpha$, with λ standing for the wavelength in the effective medium, and d is the characteristic dimension of the inclusions (diameter here). Previous works in [9, 13] have demonstrated that for cylindrical fibers, $\alpha = 2$ offers very accurate performances to predict effective properties (2D Finite Element Method, FEM, was considered as reference tool). Previous results were confirmed in [10], where the authors used 3D frequency solver FEKO© to model semi-infinite structure. In this context, few studies were proposed to model 3D configurations involving micro- or nano-inclusions; an interesting piece of work was given in [11] including Monte Carlo (MC) generation of fibers and simulation with FEM (COMSOL®) for extracting the medium conductivity.

III. NUMERICAL METHODOLOGY

As aforementioned, few works may be found regarding use of 3D electromagnetic tools to simulate random heterogeneous media. Due to the large frequency bandwidth required in this study (from 0.1 to 60 GHz), it is proposed to use time (T-) solver from CST® Microwave Studio. Baer et al. have proposed this solution for metrological work in [11] from 18 to 26 GHz, with periodical inclusions and waveguide.

The characteristics of time simulations (CST®) are summarized in Fig. 1. The details are given as follows: transient FIT solver (total duration is 400 ps); plane wave source from 100 MHz to 60 GHz, size of the composite (including spherical conducting inclusions as given in Fig. 2 (a)) parallelepiped is 1x1x6 mm^3; minimum elementary meshes are 13 nm while the convergence of 3-D meshing was ensured (data not shown here); computing time for Intel Xeon 4 cores processor is less than 3 hours (including generation of random inclusions, launching simulations, and final extraction of SE results via FFT of E-field simulation, see Fig. 2 (b): 600 frequencies equally distributed from 0.1 to 60 GHz) per test case. From [8], SE is defined as the ratio between electric (E-) field at a given location *z* (see Fig. 1, E-field probe) and frequency *f* in absence (E^0) and presence (E^c) of composite structure. In this framework, the SE (i.e., attenuation here) of the modelled medium is defined as:

$$SE(z,f) = {E^0(z,f)}\Big/{E^c(z,f)}. \tag{2}$$

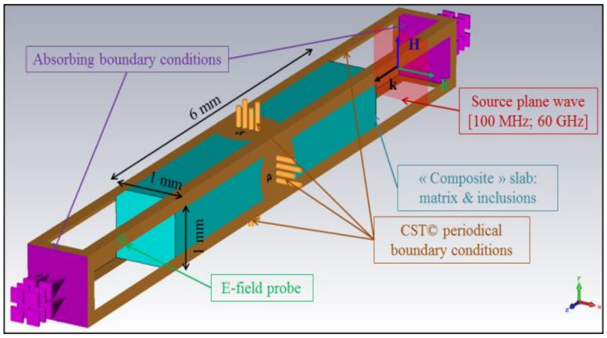

Fig. 1. Numerical setup of the 3D time domain model including source, boundary conditions, and composite sample (size, lossless epoxy resin, $\varepsilon_1 = 5\varepsilon_0$; hidden spherical inclusions inside with $\varepsilon_2 = \varepsilon_0$ and $\sigma_2 = 1000$ S/m).

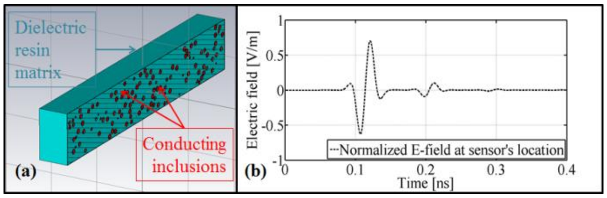

Fig. 2. (a) Sectional view (x_0=0.1 mm) of one random mixed structure; the volumetric fraction of inclusions is ν = 0.10 with constant radius of spheres (*r*=0.05 mm). (b) Normalized E-field at sensor's position (see Fig. 1) computed in time domain with CST®.

IV. STATISTICAL ASSESSMENT OF SHIELDING EFFECTIVENESS

This section is devoted to the presentation of numerical results obtained. In a first subsection, the relevance of the model will be checked in comparison to MG and DHM formalisms for various volumetric fractions of inclusions (here ν = 0.01, 0.05, 0.10). In a second step, SE statistics computed from the proposed technique will provide information about the impact of assuming random sizes of inclusions.

A. Relevance of the model from MG and DHM

Ten CST® models according to Figs. 1-2 were generated in this section, and SE mean and std were extracted for three volumetric fractions: ν_1=0.01, ν_2=0.05, and ν_3=0.10.

Figures 3-4 show the results obtained considering ν_2 and ν_3 (see Fig. 5 for volumetric rate ν_1 in Subsection IV.B). By assessing a limit of validity, the results validate MG formalism (bold crosses) in frequency. Thus, a good accordance is observed between SE statistics (plain curve and error bars) from numerical FIT modeling and MG mixing rule (transmitted E-field and SE are analytically computed from [14]). Results agree well respectively up to 25 and 15 GHz for cases ν_2 and ν_3 (case ν_1 provides good agreement with MG almost over the entire frequency bandwidth, data not shown here). Based upon DHM [9] principles, an optimized value γ=1.92 was extracted (close to γ=2 proposed in [9, 10] for cylindrical infinite straight fibers). As depicted in Figs. 3-4, an excellent agreement is observed between homogenized SE from DHM and 3D time domain FIT models.

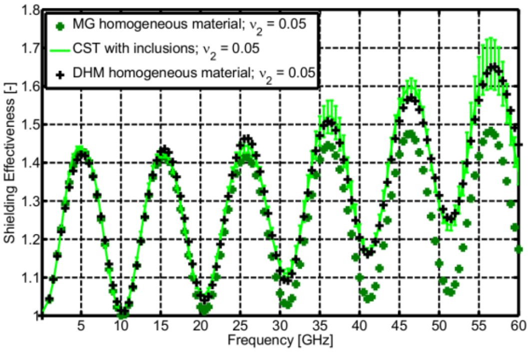

Fig. 3. SE of composite structure (ν_2=5%) respectively from MG (bold dark green crosses), DHM (thin black crosses), and statistical FIT modeling (plain green line).

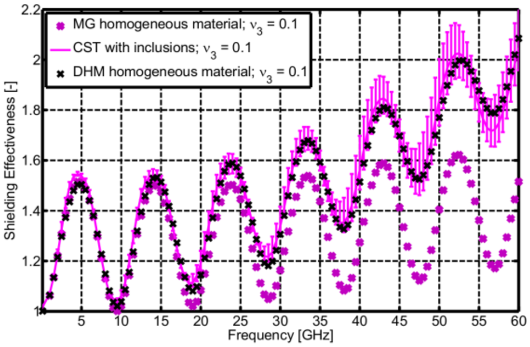

Fig. 4. SE of composite material (ν_3=10%) respectively from MG (bold dark pink crosses), DHM (thin black crosses), and statistical FIT modeling (plain pink line).

B. Influence of random sizes and locations of spherical inclusions

This subsection is devoted to the presentation of results obtained when assuming both random locations and sizes of inclusions inside resin matrix. To this end, the automated procedure between Matlab® interface (randomly generating both sizes and locations of spherical radii with MC) and CST® was enriched: the complete automation of the procedure avoided any trouble when defining 3D models, launching time domain simulations, post treatments of data). Without any loss of generality, radii of spheres were assumed to be uniformly distributed (r = 0.050 ± 0.010 mm, see caption in Fig. 5). Figure 5 shows the influence of randomizing sizes of inclusions (dashed blue line) in comparison to solely taking into account random location of inclusion inside resin matrix (plain red line). It is to be noted that the analytical results from DHM agree very well with time domain 3-D simulations.

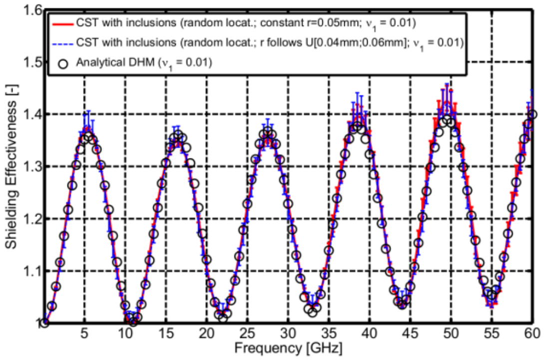

Fig. 5. Impact of assuming random law (uniform distribution between 0.040 and 0.060 mm) for the size of spherical inclusions (volume fraction ν_1=1%): constant radius r=0.050 mm (bold red line), random distribution of sizes (thin blue line), and analytical homogenized DHM data (black circles).

Figure 6 provides qualitative and quantitative results by assessing the effect of random generation of inclusions for volumetric rate ν_1=0.01. As it is the case in Fig. 5, SE std offers an overview of the statistical dispersion of results from 0.1 to 60 GHz. This is higher for test case including random dimensions of spherical inclusions (thin blue line) than where spheres' radii are assumed constant (r=0.050 mm). Despite all, the reproducibility (and the relatively low coupling effect of inclusion due to their vicinity) leads to weak levels of SE std. Indeed, the averages over the whole frequency band of SE std are respectively 0.0047 and 0.0081 (far weaker than mean levels of SE around 1.2, see Fig. 5). Finally, Fig. 6 confirms the very good agreement between SE statistics from FIT modeling (CST®) and DHM (taken from same optimization than in Section IV.A) mixing formalism.

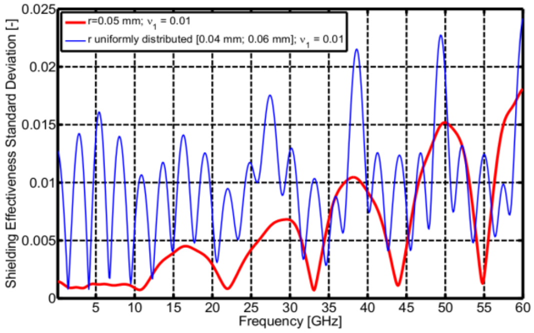

Fig. 6. SE standard deviation (10 CST® simulations, see Fig. 4) with random locations of inclusions and: (red) constant spherical radius (bold line); (blue) random radii of spheres (thin line).

V. CONCLUSION

This article proposes an automated procedure relying on time domain modeling of composite biphasic mixture. It has been validated with regard to classical mixing rules (here Maxwell-Garnett) and offers a statistical overview of the SE of micro-structured composites. The automation of the entire procedure provides useful information about the statistical dispersion of results, jointly with numerical trustworthy data to calibrate advanced homogenization model, such as DHM. Some additional works are nowadays in progress to extend current study to: alternative shapes of inclusions, different electrical characteristics (e.g., conductivity, complex permittivity modelling) of particles and multi-physics issues (thermal and mechanical ones for instance), and modeling of realistic EMC issues including frequency dispersive materials as it is the case in [7]. The proposed methodology could be useful in different domains including antennas and propagation, plasma, metrology, and remote sensing.

REFERENCES

[1] M. Vincent, M. Klingler, Z. Riah, and Y. Azzouz, *Influence of Car Body Materials on the Common-Mode Current Radiated Emissions Induced by Automotive Shielded Cables*, in Proc. Joint IEEE Int. Symp. on EMC and EMC Europe 2015, Dresden, Germany, August 2015.

[2] A. Smorgonskiy, F. Rachidi, M. Rubinstein, N. Korovkin, and A. P. Vassilopoulos, *On the Adequacy of Standardized Lightning Current Waveform for Composite Structures for Aircraft and Wind Turbine Blades*, in Proc. EMC Europe 2016, Wroclaw, Poland, September 2016.

[3] A. Meddipour, I. D. Rosca, A. Sebak, C. W. Trueman, S. V. Hoa, "Advanced Carbon-Fiber Composite Materials for RFID Tag Antenna Applications," *ACES Journal*, vol. 25, no. 3, pp. 218-229, 2010.

[4] W. Abdelli, X. Mininger, L. Pichon, and H. Trabelsi, "Impact of Composite Materials on the Shielding Effectiveness of Enclosures," *ACES Journal*, vol. 27, no. 4, pp. 369-375, 2012.

[5] M. Boubekeur, A. Kameni, A. Modave, L. Bernard, and L. Pichon, "Modeling of Weakly Conducting Thin Sheets in the Discontinuous Galerkin Method for Shielding Effectiveness Evaluation," *ACES Journal*, vol. 28, no. 10, pp. 931-937, 2013.

[6] D. Micheli, C. Apollo, R. Pastore, D. Barbera, R. Bueno Morales, M. Marchetti, G. Gradoni, V. Mariani Primiani, and F. Moglie, "Optimization of Multilayer Shields Made of Composite Nanostructured Materials," *IEEE Trans. on EMC*, vol. 54, pp. 60-69, 2012.

[7] M. Y. Koledintseva, J. Drewniak, R. DuBroff, K. Rozanov, and B. Archambeault, "Modeling of shielding composite materials and structures for microwave frequencies," *PIER B*, vol. 15, pp. 197-215, 2009.

[8] M. Y. Koledintseva, R. DuBroff, and R. Schwartz, "Maxwell-Garnett rule for dielectric mixtures with statistically distributed orientations of inclusions," *Progress in Electromagnetics Research (PIER)*, vol. 99, pp. 131-148, 2009.

[9] V. Préault, R. Corcolle, L. Daniel, and L. Pichon, "Effective permittivity of shielding composite materials for microwave frequencies," *IEEE Trans. on EMC*, vol. 55, pp. 1178-1186, 2013.

[10] Y. Liao, G. Shi, L. Yuan, and X. Ying, *Equivalent modeling of the microwave dielectric properties for fiber reinforced shielding composites*, in Proc. 7th Asia Pacific Int. Symp. on EMC, 2016.

[11] C. Baer, B. Hattenhorst, C. Shultz, B. Will, I. Rolfes, and T. Musch, *Analysis of composite materials with periodically aligned inclusions using 3D field simulations*, in Proc. GeMiC 2016, pp. 120-123, 2016.

[12] T. Zhang and Y. B. Yi, "Monte Carlo simulations of effective electrical conductivity in short-fiber composites," *Journal of Applied Physics*, 103, 014910, 2008.

[13] V. Préault, "Méthode d'homogénéisation pour la modélisation électromagnétique de matériaux composites," PhD Thesis (in French), 2013.

[14] L. Zheng, Q. Zhao, and X. J. Xing, "Effect of plasma on electromagnetic wave propagation and THz communications for reentry flight," *ACES Journal*, vol. 30, no. 11, November 2015.

Circularly Polarized Aperture-Coupled Microstrip-Line Fed Array Antenna for WiMAX/C Bands Applications

Vahid Rafiei [2], **Hasan Saygın** [1], **and Saeid Karamzadeh** [1,2]

[1] Application & Research Center for Advanced Studies, Istanbul Aydin University, Turkey
[2] Department of Electrical and Electronics Engineering, Istanbul Aydin University, Istanbul, Turkey
vahidrafiei@aydin.edu.tr, karamzadeh@itu.edu.tr, hasansaygin@aydin.edu.tr

Abstract — In this paper, a new configuration of broad band circularly polarized (CP) array antenna is presented by a modified feeding network The proposed feed network includes two hybrid 90-degree branch line coupler and a 180-degree rat-race coupler. The feed network of array provides sequential rotation condition for consisting of four L-shaped microstrip lines which coupling through four ring-shaped slots. Each element of array is printed on two layer of substrate which connected together with a ring aperture. Employing wideband CP elements and feeding network structure causes the creation of innovation at CP array. The 3dB axial-ratio bandwidth of the array extends to approximately 650 MHz with impedance bandwidths of 24.7% for C-band applications and a relative high gain of about 10.2 dBic. The performance of the antenna has been approved by comparing between measurement and simulation results.

Index Terms — Aperture-coupled microstrip-line fed, array antenna, circularly polarized.

I. INTRODUCTION

Recently, the use of circularly polarized (CP) antennas have advantages such as: very effective in combating multipath interferences or fading, able to reduce the “Faraday rotation” effect due to the ionosphere and no strict orientation between transmitting and receiving antennas are required [1–15]. Therefore, circularly polarized antennas play a key role in many wireless applications, such as RFID systems, satellite communication and navigation systems. These antennas have more popularity because of their better mobility and weather penetration [1-7]. Microstrip technology with light weight and easy fabrication as a choice is constructed. But, the inherent narrow axial-ratio (AR) bandwidth and low gain of the microstrip antenna leads to limit their applications. The printed CP slot antennas attract much attention due to their capabilities of providing wide impedance and AR bandwidths while maintaining the low profile [1-15].

Hitherto, many attempts to improve them have been reported [2-7]. A feeding mechanism for patch antenna with circular polarization is proposed that has a feeding geometry, which is an integration of a hook shape feed line and four Γ-slots, a 2×2 sequentially rotated CP slot patch antenna array using a microstrip-line-to-asymmetric-CPW feeding network has been presented in [2]. In [5], a design of a circularly polarized array using a two section cascaded coupler feeding system for creating broadband circular polarization performance has been presented, which feeding network of the array is composed of a 180° ring hybrid coupler connected to the two branch-line couplers generating circular polarization. Despite the reported works can improve 3-dB AR bandwidth, they often suffer from large size and low gain.

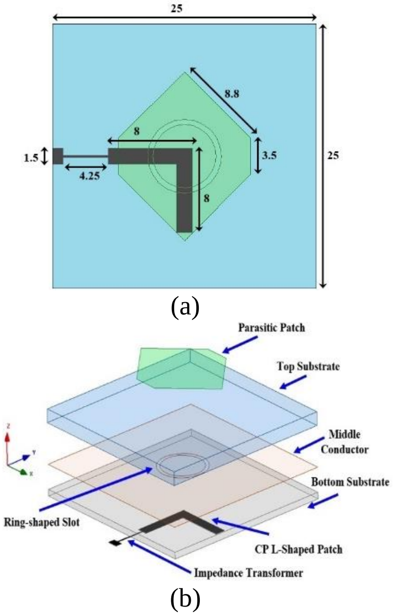

(a)

(b)

Fig. 1. Configuration of the proposed CP array antenna elements: (a) top view and (b) perspective view.

To addressed mentioned problems, in this paper a novel CP array antenna is presented. The proposed antenna consists of four single elements which each of

Submitted On: March 2, 2017
Accepted On: July 24, 2017

elements includes two layers of substrate which by a ring slot feed and radiation patch isolated from together. A cascade feed network includes two branch line and a rat-race coupler provide sequentially rotated conditions. Results and details of proposed antenna are discussed in following sections.

Table 1: Comparison of the proposed antenna size and measured characteristics with other references; the impedance bandwidth is for a frequency range where the VSWR ≤ 2, and ARBW is the 3-dB axial-ratio bandwidth

Ref.	Size (mm^3)	BW (GHz)	3dB ARBW (GHz)	Peak Gain (dBic)
[8]	70×70×1.60	0.85 (1.75-2.6)	0.4 (1.7-2.1)	3.7
[9]	70×70×1.60	0.20 (1.5-1.7)	0.3 (1.5-1.8)	3.5
[10]	70×70×1.60	0.80 (1.6-2.4)	0.2 (1.8-2.0)	3.5
[11]	60×60×0.76	0.80 (1.7-2.5)	0.7 (1.8-2.5)	3.5
[12]	60×60×0.74	1.40 (1.6-3.0)	0.7 (2.3-3.0)	4.0
[15]	30×30×0.80	1.2 (4.9-6.1)	0.5 (5.25-5.75)	3.7
This work	25×25×1.4	1.11(4.87-5.98)	0.63 (5.17-5.8)	5.8

II. ANTENNA ELEMENTS

Construction of CP array elements is displayed in Fig. 1. The proposed elements are consisted of two layers of FR4 substrate with relative permittivity of (ε_r=) 4.4 and loss tangent of (tanδ=) 0.02. In order to reduce radiation loss and improvement of radiation characteristics of the patch, the thicknesses of bottom and top substrates are chosen to be 0.8 mm and 1.6 mm, respectively (Figs. 1 (a), (b)). At the bottom side of the array elements, a thin microstrip line with a length of 4.25 mm and width of 0.2 mm acts as an impedance transformer between the CP L-shaped antenna and the 50 Ω microstrip line along the y-axis. Between the two substrates, a metallic layer including a ring-shaped slot which performs as an aperture slot is created. The bottom layer of single element consists of a L shape feed line which among a ring aperture slot between two substrates couples to upper patch. The size of ring aperture is regulated so that provides a 90-degree phase difference in two point of excitation by L-shape feed toward top patch. At top layer, in order to improve CP features two opposite corner of rectangular patch is chamfered. The results of single element are illustrated in Fig. 2. As it is shown, the impedance bandwidth is 4.87 to 5.98 GHz (Fig. 1 (a)) with 630 MHz 3-dB AR bandwidth (Fig. 1 (b)). The proposed antenna with an almost constant gain in all of IBW generates a broadside pattern (Fig. 1 (c)), as expected. The proposed single element has an area of 625 mm^2 (25 mm × 25 mm), which is significantly less than the previously published slot antennas as summarized in Table 1. Compared to other types of CP slot antennas fabricated on the same substrate the proposed antenna exhibits an impedance bandwidth which is significantly larger and with no reduction in the gain performance, as well as having a larger circular polarization bandwidth. The gain is comparable to previous designs.

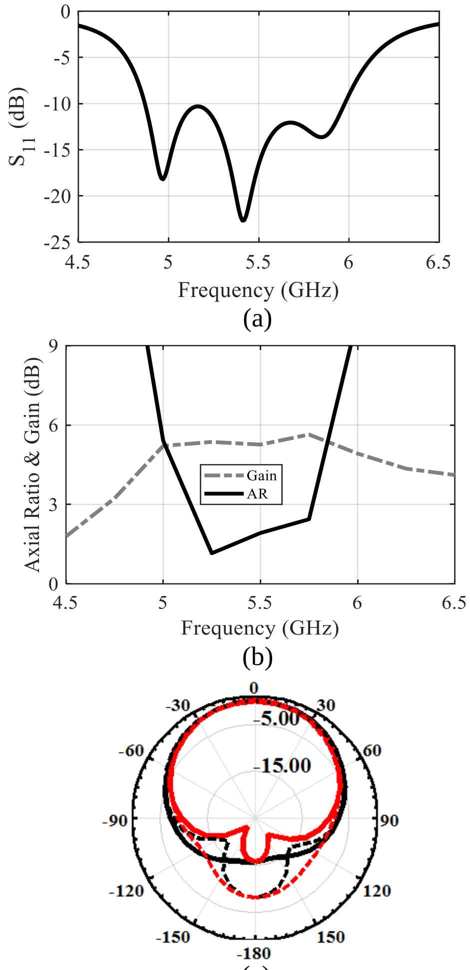

(a)

(b)

(c)

Fig. 2. Results of the proposed CP array antenna elements (solid lines are CP right hand, dash lines are CP left hand, blue lines are at φ=0° and red lines are at φ=90°). (a) The simulated S_{11}, (b) the simulated gain and axial ratio, and (c) a normalized simulated radiation pattern at 5.5 GHz.

III. ARRAY ANTENNA DISCUSSION

The feed network and array antenna designed and optimized by using Agilent Advanced Design system (ver.2012) and Ansys HFSS (ver. 13), respectively. In order to enhance the 3-dB axial ratio bandwidth and pattern balance, elements rotations must be changed as much as 90° between the adjacent elements and 180° between the opposite ones, and phase delay of the feed line has to be changed according to the elements rotations, respectively. The details of the configuration and feed network of the proposed CP array antenna are displayed in Fig. 3. As shown in Fig. 3 (a), the feed network uses a 180° ring hybrid coupler to realize a 3 dB power split, equal in magnitude, but 180° out of phase. Two branch-line hybrid couplers then divide the signal energy into two paths and give the signal to each of the output branches with the same amplitude, but phase-shifted by 90°, wherein the relative phases at four feed points are 0°, 90°, 180° and 270°.

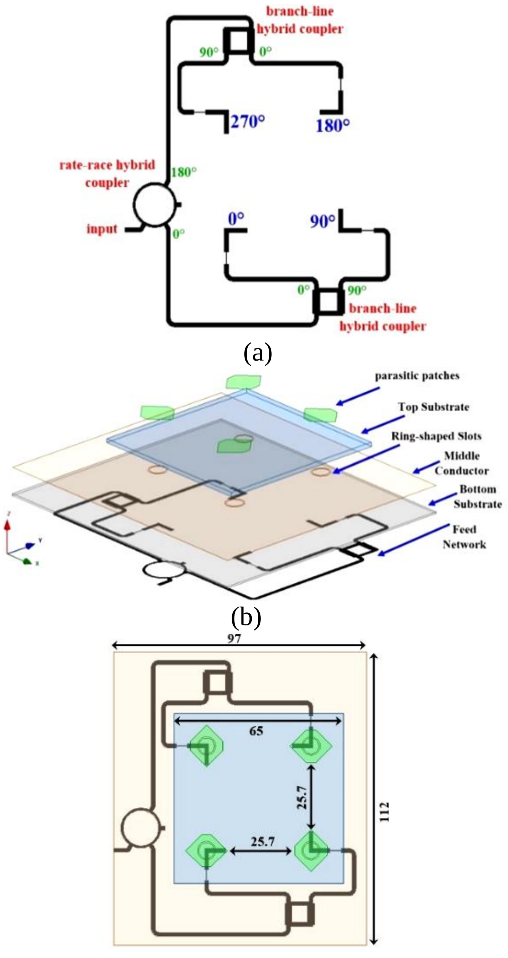

(a)

(b)

(c)

Fig. 3. A configuration and feed network of the proposed CP array antenna: (a) top view of feed network, (b) perspective view of the proposed CP array antenna, and (c) top view of the proposed CP array antenna.

A perspective and top view of the proposed CP array antenna are shown in Fig. 3 (b) and Fig. 3 (c) respectively. The scattering parameter of the proposed array antenna is measured by the Agilent™ 8722ES vector network analyzer. The CP array antenna achieves measured impedance bandwidths from 4470 to 6670 MHz for C-band applications with S_{11}<-10 dB, as demonstrated in Fig. 4 (a). The comparison between simulated and measured AR and gain of the proposed array antenna are shown in Fig. 4 (b). The measured AR bandwidth of the array is 650 MHz between 4870 MHz to 5520 MHz. Minimum point of the axial-ratio curve is at 5000 MHz with a magnitude of 1.67 dB. The proposed array has a peak gain of 9.85 dBic at 6.24 GHz. A standard linearly polarized waveguide BJ320 was used to measure the total gain characteristics. The measured results of the normalized radiation patterns of the array at 5 GHz are presented in Fig. 4 (c). The RHCP and LHCP radiation patterns of the array are obtained at φ=0° and φ=90°. The array antenna size is 97 mm × 112 mm. Also a photograph of the fabricated antenna is shown in Fig. 5.

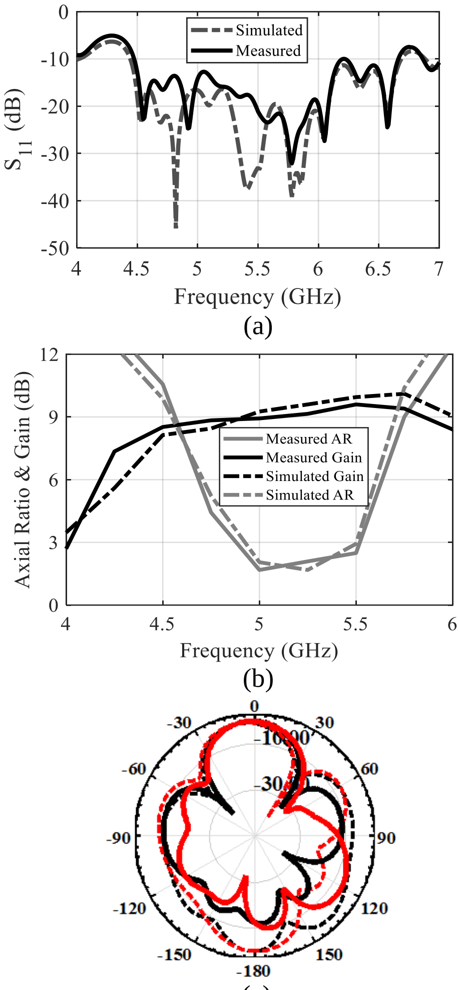

(a)

(b)

(c)

Fig. 4. Results of the proposed CP array antenna (solid lines are CP right hand, dash lines are CP left hand, blue lines are at φ=0° and red lines are at φ=90°). (a) Comparison between the simulated and measured S_{11}, (b) comparison between the simulated and measured gain and axial ratio, and (c) normalized measured radiation pattern at 5.5GHz.

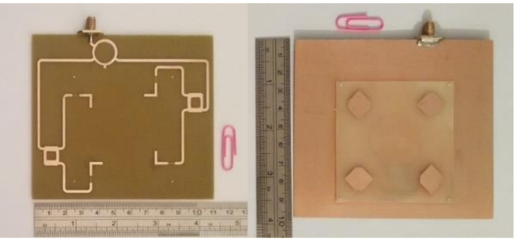

Fig. 5. Photograph of the fabricated antenna.

The design when compared with the previous CP array structures with sequential feed network and arc feed-line presented in Table 2 show significantly increased impedance bandwidth and axial-ratio bandwidth, i.e., the impedance and AR bandwidth are, respectively, more than three and two fold wider than the previous designs.

Table 2: Comparison of the proposed feed network structure and measured characteristics with other array antennas

Ref.	Feed Network	Impedance BW	ARBW	PG (dBic)	Substrate
[13]	Asymmetric CPW	0.80 (1.1-1.9)	0.80 (1.1-1.9)	~7.5	FR4
[14]	Aperture Coupled	0.80 (1.6-2.4)	0.60 (1.7-2.3)	~15	Rogers 5880
[15]	Symmetric Microstrip	1.7 (4.5-6.2)	1.47 (4.75-6.22)	7.2	FR4
This work	Cascade	2.2 (4.47-6.67)	0.65 (4.87-5.52)	10.2	FR4

IV. CONCLUSION

In this paper, a two layers CP array antenna using the cascade feed network for C-band application is presented. The feed network by special structure which consists of two 90-degree couplers and a 180 degree couplers can be realized a broadband sequentially rotated condition. The single elements of antenna have been designed on two layer which isolated feed network and radiating patch by a ring slot. The patch of antenna to provide better CP feature was chamfered in two opposite corner. Proposed antenna compared with other works and indicated that proposed antenna is better than they from most aspects.

REFERENCES

[1] H. W. Lai, K. M. Mak, and K. F. Chan, “Novel aperture-coupled microstrip-line feed for circularly polarized patch antenna,” *Progress In Electromagnetics Research*, vol. 144, pp. 1-9, 2014/

[2] S. Fu, S. Fang, Z. Wang, and X. Li, “Broadband circularly polarized slot antenna array fed by asymmetric CPW for L-band applications,” *IEEE AWPL. Lett.*, vol. 8, pp. 1014-1015, Sep. 2009.

[3] H. Ebrahimzadeh, Ch. Ghobadi, J. Nourinia, “Circular multi UWB monopole antenna,” *IEICE Electronic Express*, vol. 7, no. 10, pp. 717-721, 2010.

[4] S. Gao, Q. Yi, and A. Sambell, “Low-cost broadband circularly polarized printed antennas and array,” *IEEE Antennas and Propagation Magazine*, vol. 49, no. 4, pp. 57-64, Aug. 2007.

[5] S. Karamzadeh, V. Rafii, M. Kartal, O. N. Ucan, and B. S. Virdee, “Circularly polarised array antenna with cascade feed network for broadband application in C-band,” *Electronics Letters*, vol. 50, no. 17, pp. 1184-1186, Aug. 2014.

[6] G. Kumar and K. L. Ray, *Broad Band Microstrip Antennas*. Artech House, Boston, pp. 362-363, 2003.

[7] J. K. Mandal, S. C. Satapathy, M. Kumar Sanyal, P. P. Sarkar, and A. Mukhopadhyay, “Information systems design and intelligent applications,” *Proceedings of Second International Conference, INDIA*, vol. 1, pp. 82-83, 2015.

[8] J. Y. Sze, K. L. Wong, and C. C. Huang, “Coplanar waveguide-fed square slot antenna for broadband circularly polarised radiation,” *IEEE Trans. Antennas Propag.*, vol. 51, pp. 2141-2144, Aug. 2003.

[9] J.-Y. Sze and Y.-H. Ou, “Compact CPW-fed square aperture CP antenna for GPS and INMARSAT applications,” *Microw. Opt. Technol. Lett.*, vol. 49, no. 2, pp. 427-430, Feb. 2007.

[10] C. C. Chou, K. H. Lin, and H. L. Su, “Broadband circularly polarized cross-patch-loaded square slot antenna,” *Electron. Lett.*, vol. 43, no. 9,pp. 485-486, Apr. 2007.

[11] J.-Y. Sze, J.-C. Wang, and C.-C. Chang, “Axial-ratio bandwidth enhancement of asymmetric-CPW-fed circularly-polarised square slot antenna,” *Electron. Lett.*, vol. 44, no. 18, pp. 1048-1049, Aug. 28, 2008.

[12] J.-Y. Sze and C.-C. Chang, “Circularly polarized square slot antenna with a pair of Inverted-L grounded strips,” *IEEE Antennas Wireless Propag. Lett.*, vol. 7, pp. 149-151, 2008.

[13] S. Fu, S. Fang, Z. Wang, and X. Li, “Broadband circularly polarized slot antenna array fed by asymmetric CPW for L-band applications,” *IEEE AWPL. Lett.*, vol. 8, pp. 1014-1015, Sep. 2009.

[14] S. Gao, Q. Yi, and A. Sambell, “Low-cost broadband circularly polarized printed antennas and array, *IEEE Antennas and Propagation Magazine*, vol. 49, no. 4, pp. 57-64, Aug. 2007.

[15] S. Karamzadeh, B. S. Virdee, V. Rafii, and M. Kartal, “Circularly polarized slot antenna array with sequentially rotated feed network for broadband application,” *Int. J. RF and Microwave Comp. Aid. Eng.*, vol. 25, pp. 358-363, 2015. doi:10.1002/mmce.20869

A Broadband Dual-Polarized Antenna for TD-SCDMA System

Zhiwei Liu, Yichao Li, Jun Liu, Yueyuan Zhang, Xiliang Wu, and Yunhong Zhou

Department of Information Engineering
East China Jiaotong University, Nanchang, 330013, China
zwliu1982@hotmail.com, 516538157@qq.com, 328804642@qq.com, zyyaney1981@hotmail.com,
1244501724@qq.com, 843082091@qq.com

***Abstract* —** A broadband dual-polarized antenna is proposed for TD-SCDMA system. The dual-polarized antenna is combined with two perpendicularly crossed dipoles. Crossed dipoles can reduce the same frequency interference and improve the signal reception effect. The isolation of this dual-polarized antenna is greater than 25 dB for co-polarization and 28 dB for cross-polarization. The measured results demonstrate that voltage standing wave ratio (VSWR) is no more than 1.3 at the operating frequency and the antenna has an average gain of 8.3 dBi for slant polarizations. That is, our proposed antenna meets the requirements for stringent design. We use array antenna technology based on the requirements of gain and beam tilt. A 5-element dual polarized antenna array is realized by 5-way unequal power divider at 1880 - 2635 MHz. The antenna gain of the array is about 12.5 dBi for different polarization. In numerical and measured results, the specific design methods and ideas of antenna and power divider are presented. As we can see from the test results, the antenna presented in this paper is far better than the industry standard.

***Index Terms* —** Array, base-station antenna, dual-polarized antenna, TD-SCDMA system.

I. INTRODUCTION

In the past 30 years, it has been witnessed a tremendous success of wireless communication in the global market. Even after decades of fast growth, the number of cellular devices is still steadily increasing, surpassing the population in some countries due to consumers' need to stay connected wirelessly. For instance, since China Mobile commercially launched TD-SCDMA 3G in 2009, statistics data reveals that there have been more than 2.3 hundred million TD-SCDMA subscribers until April 2014 [1].

One of the key components in wireless mobile communication systems is the base station antenna, which plays a critical role in converting the electromagnetic waves that propagate in free space to electric current in the base station's circuitry [2- 4]. With the development of various generations of wireless mobile communication systems [5], researchers have achieved numerous milestones for different standards of base station antennas used in many wireless communication systems including advanced mobile phone service (AMPS) system, GSM, CDMA, TD-SCDMA, WCDMA, CDMA2000, and Wimax [6-10], as well as 4G (LTE / LTE Advanced) base station antenna [11, 12]. In addition, most of related work on base station antenna design focuses on the miniaturization, broadband, dual frequency band [13, 14, 15], and smart antenna characteristics. The smart antenna technology is used to replace the conventional antenna to improve the spectrum efficiency. It has spatial filtering to the beam from all directions, which improves the reliability of the system. According to the specifications of Table 1.

Table 1: TD-SCDMA antenna specifications

Frequency	1880 - 2635 MHz
VSWR	< 1.5
Ports isolation	> 28 dB (cross polarization); > 25 dB (co polarization)
Front-to-back ratio	> 25 dB
Cross polarization ratio	> 15 dB (0 deg)
Gain	> 12.5 dBi
Angle of inclination	6 deg

II. DUAL-POLARIZED ANTENNA DESIGN

A. Antenna element design

The configurations of the proposed antenna element operating at 1880 - 2635 MHz are illustrated in Fig. 1. For a better description of the antenna element, the x-y plane is defined as the horizontal plane (H-plane) and x-z plane as the vertical plane (V-plane). Radiator arm is a square ring type structure, which is not only expand the radiation unit band width, but also greatly reduce the weight, material and cost. The brace is a quarter-wavelength Balun structure placed to make the current on two dipoles balanced and to achieve the impedance matching. Radiation arm is ± 45° dual-polarization integration, using traditional half-wave dipole form. L_1 is calculated according to the half wavelength of the center frequency point 2.2 GHz. The length of the H_3 is

Submitted On: December 15, 2016
Accepted On: March 22, 2017

slightly smaller than a quarter wavelength of the center frequency. The rest of the size is optimized by HFSS software simulation. The specific size of the antenna can be seen in Table 2. Finally, the far-field of the antenna is measured by an outdoor test system. The system is able to measure the margin of the far field antenna pattern, phase center, gain, beam-width and so on. It also can automatically generate the test report. This system consists of a holder, an antenna rotating pedestal system, a vector network analyzer, a data-processing system, and some computers. The model of the vector network analyzer is Agilent E5017C, which is used to measure the radiation pattern of the antenna.

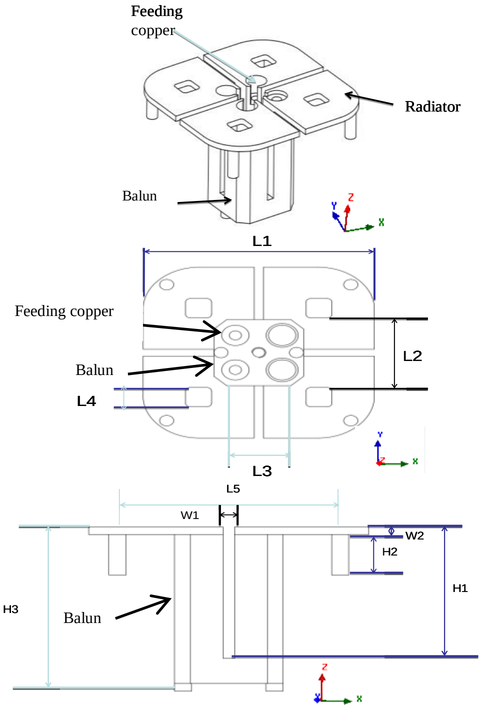

Fig. 1. Structure of the element: plan, top and side view.

Table 2: Key size of the proposed antenna (unit: *mm*)

L_1	L_2	L_3	L_4	L_5	H_1	H_2	H_3	W_1	W_2
49	20	13.5	5.5	39	26	8	31	2	1.5

The simulated VSWR and gain of one unit is given in Fig. 2. VSWR of two ports are less than 1.3 within the working frequency band and the peak gain of the antenna element is about 8.3 dBi.

B. 5-way power divider

5-element linear array is applied to enhancing the gain of the antenna to meet the requirements. Antenna has four rows of linear array since eight channels are required by TD-SCDMA. Thus, 5-way power divider is needed to meet the requirement. According to beam-forming theory, the power ratio of each element is 0.6: 0.8: 1: 0.8: 0.6. Figure 3 (a) describes the impedance calculation principle of 5-way power divider. The width of each micro-strip line can be evaluated from impedance. In the light of the required inclination angle, we can calculate the phase of each port. In Fig. 3 (b), it is shown that the specific phase calculation process.

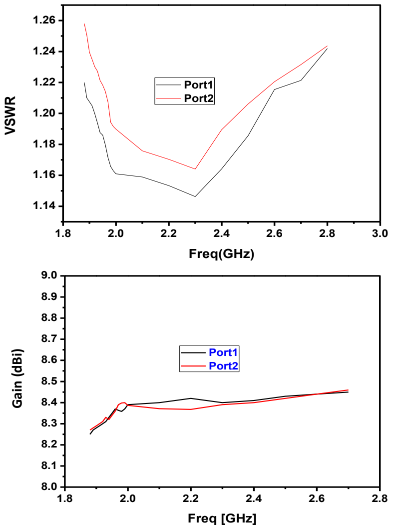

Fig. 2. Simulated results of VSWR and gain for proposed antenna element.

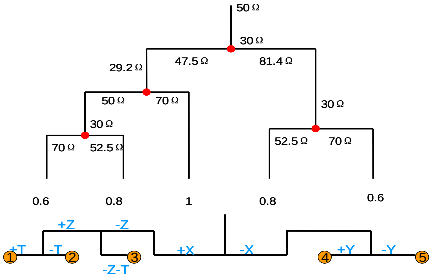

Fig. 3. Calculation principle of 5-way power divider: impedance (upper) and phase (lower).

Spacing between each unit is approximately 110 *mm* according to the 0.9 wavelength of center frequency. The ADS software is used to obtain the simulation results of the power divider. Figure 4 has shown the layout of ADS design 5-way power divider. In Fig. 5 (a), both simulation and measured data of VSWR are less than 1.12 and 1.25, respectively. The simulated and measured phase curves are shown in Fig. 5 (b), from which it can be seen that two results have good agreement. From Fig. 5 (c), we can see that the ratio of amplitude approximately as follows: 0.6: 0.8: 1: 0.8: 0.6 (S_{12}: S_{13}: S_{14}: S_{15}: S_{16}).

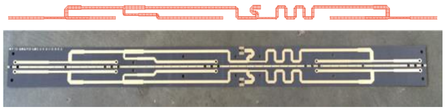

Fig. 4. Structure of power divider.

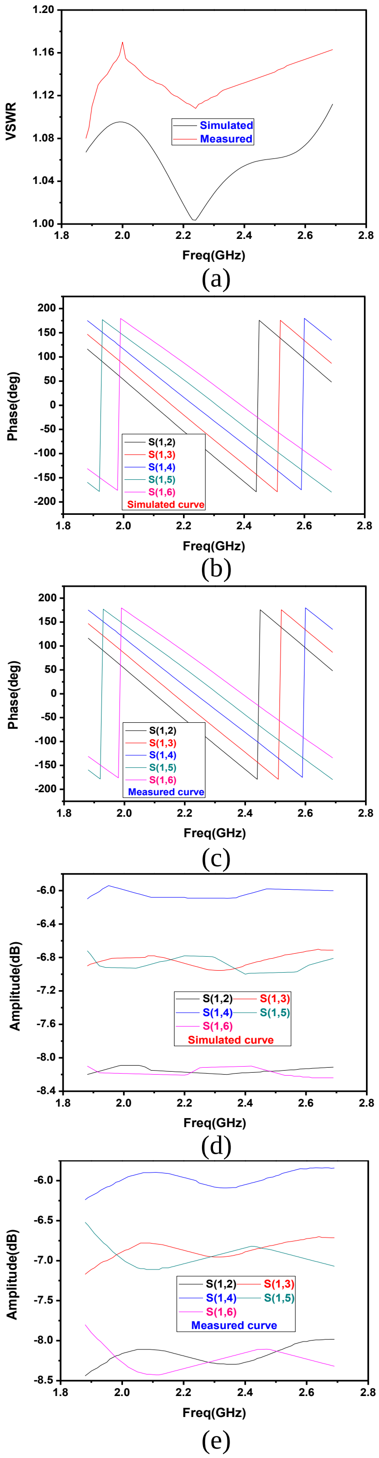

Fig. 5. Simulated and measured results of power divider: (a) VSWR; (b) simulated results of phase; (c) measured results of phase; (d) simulated results of amplitude; (e) measured results of amplitude.

C. Antenna array design

A dual-polarized antenna array with 4 × 5 elements is developed for TD-SCDMA applications which is depicted in Fig. 6. The element spacing was optimized for a maximum gain but without the appearance of grating lobes. A 5-way power divider is employed to feed the antenna array for each polarization. Flexible coaxial line is used to connect each element for each polarization to the power divider. The measured VSWR of the dual-polarized antenna array are shown in Fig. 7. The measured isolation is higher than 25 dB. The lowered isolation for the antenna array compared to the antenna element is mainly due to the coupling between two adjacent antenna elements for different polarizations. From the measurement in Fig. 8, the front-to-back ratio and axial cross polarization ratio are 28 dB and 17 dB at 1.88 GHz, 27 dB and 20 dB at 2.025 GHz, 30 dB and 22 dB at 2.635 GHz, respectively. The measured gain of antenna array are plotted in Fig. 9. The measured gain is about 13 dBi, slightly lower than the simulated result due to the losses from the power dividers and coaxial lines which were not taken into account in simulation.

Fig. 6. Prototype of array antenna.

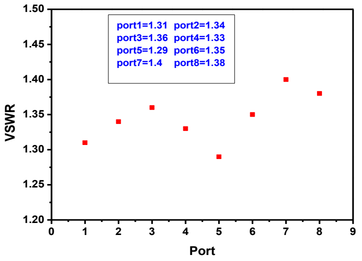

Fig. 7. Measurement of VSWR for different port.

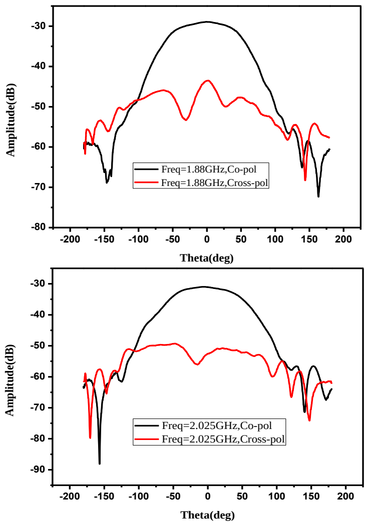

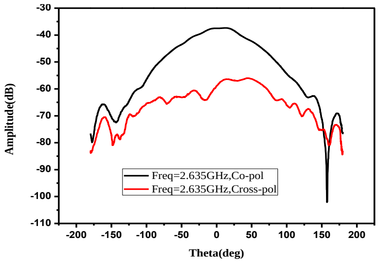

Fig. 8. Measurement for horizontal plane.

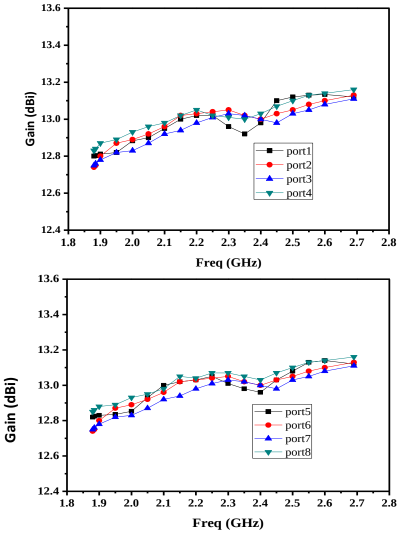

Fig. 9. Measurement of gain for different ports.

III. CONCLUSION

A broadband dual-polarized antenna is proposed for TD-SCDMA system. The dual-polarized antenna is composed of two perpendicularly crossed dipoles. The dual-polarized antenna has isolation of same polarization greater than 25 dB and isolation of different polarization greater than 28 dB. Measurements verify that this proposed antenna can meet the stringent design requirements including VSWR less than 1.3 at the operating frequency and average gain of 8.3 dBi for slant polarizations. A 5-element dual-polarized antenna array is realized by 5-way unequal power divider and the gain is about 12.5 dBi for each polarization.

ACKNOWLEDGEMENT

This work was supported by the National Natural Science Foundation of China (No. 61261005, 61601185), Graduate Innovation Fund Project (YC 2014-S270).

REFERENCES

[1] C. L. Lin, *Antenna Engineering Handbook*. Beijing, China: Pub. House of Electronics Industry, 2002.

[2] J. D. Kraus, *Antennas: For All Applications*. Beijing, China: Pub. House of Electronics Industry, 2005.

[3] C. A. Balanis, *Antenna Theory Analysis and Design*. Hoboken, NJ, USA: Wiley, 2005.

[4] J. A. Kong, *Electromagnetic Wave Theory*. Beijing, China: Publishing House of Electronics Industry, 2003.

[5] T.-W. Chiou and K.-L. Wong, “Broad-band dual-polarized single microstrip patch antenna with high isolation and low cross polarization,” *IEEE Trans. Antennas Propag.*, vol. 50, no. 3, pp. 399-401, Mar. 2002.

[6] K.-L. Wong and T.-W. Chiou, “Broad-band dual-polarized patch antennas fed by capacitively coupled feed and slot-coupled feed,” *IEEE Trans. Antennas Propag.*, vol. 50, no. 3, pp. 346-351, Mar. 2002.

[7] S. K. Padhi, N. C. Karmakar, Sr., C. L. Law, and S. Aditya, Sr., “A dual polarized aperture coupled circular patch antenna using a C-shaped coupling slot,” *IEEE Trans. Antennas Propag.*, vol. 51, no. 12, pp. 3295-3298, Dec. 2003.

[8] Y.-X. Guo, K.-M. Luk, and K.-F. Lee, “Broadband dual polarization patch element for cellular-phone base stations,” *IEEE Trans. Antennas Propag.*, vol. 50, no. 2, pp. 251-253, Feb. 2002.

[9] H. Wong, K.-L. Lau, and K.-M. Luk, “Design of dual-polarized L-probe patch antenna arrays with high isolation,” *IEEE Trans. Antennas Propag.*, vol. 52, no. 1, pp. 45-52, Jan. 2004.

[10] S. Finistauri, G. Marrocco, G. D’Orio, M. Motta, and S. De Polo, “Investigation on pattern distortion of landscape-compliant 3G base station antennas,” *in Proc. IEEE Antennas Propag. Soc. Int. Symp.*, vol. 1, pp. 1054-1057, 2004.

[11] K.-M. Luk and B. Wu, “The magnetoelectric dipole—A wideband antenna for base stations in mobile communications,” *Proc. IEEE*, vol. 100, no. 7, pp. 2297-2307, July 2012.

[12] M. A. Soliman, W. Swelam, A. Gomaa, and T. E. Taha, “Steerable dual band planar microstrip phased array antenna for 3G and 4G wireless communication systems,” *in Proc. IEEE-APS Topical Conf. Antennas Propag. Wireless Commun.* (*APWC*), pp. 905-908, 2001.

[13] W. An, H. Wong, K. L. Lau, S. Li, and Q. Xue, “Design of broadband dual-band dipole for base station antenna,” *IEEE Trans. Antennas Propag.*, vol. 60, no. 3, pp. 1592-1595, Mar. 2012.

[14] Y. Cui, R. Li, and P. Wang, “A novel broadband planar antenna for 2G/3G/LTE base stations,” *IEEE Trans. Antennas Propag.*, vol. 61, no. 5, pp. 2767-2774, May 2013.

[15] Y. Cui, R. Li, and P. Wang, “Novel dual-broadband planar antenna and its array for 2G/3G/LTE base stations,” *IEEE Trans. Antennas Propag.*, vol. 61, no. 3, pp. 1132-1139, Mar. 2013.

[16] H. W. Lai, K. K. So, H. Wong, C. H. Chan and K. M. Luk, “Magnetoelectric dipole antennas with dual open-ended slots excitation,” *IEEE Trans. Antennas Propag.*, vol. 64, no. 8, pp. 3338-3346, Aug. 2016.

Frequency and Time Domain Analysis of Planar UWB Antenna with Controllable WIMAX/WLAN Band-Notched Characteristics

Rajarshi Sanyal [1], Debashree Bhowmik [1], Partha P. Sarkar [2], and Santosh K. Chowdhury [3]

[1] Department of Electronics & Communication Engineering
MCKV Institute of Engineering, Howrah, W.B., India
rajarshi.sanyal1972@gmail.com, debashree.debu.bhowmik965@gmail.com

[2] Department of Engineering and Technological Studies (DETS)
University of Kalyani, Nadia, W.B., India
parthabe91@yahoo.co.in

[3] Kolkata W.B., India
santoshkumarchowdhury@gmail.com

Abstract – An ultra wideband (UWB) printed monopole antenna with dual band stop characteristics is proposed in this article. Distinctive feature of this antenna is the notched band control ability with improved operating bandwidth. By employing modified λ/2 vertically combined T and U-shaped conductor backed plane, a sharp band notch is achieved with notched band of 3.3–3.7 GHz. In order to obtain another notched frequency band of 5.1-6 GHz, a rectangular spiral shaped λ/4 open stub has been incorporated to the microstrip feed line. Frequency rejection performance can be controlled flexibly by varying various parameters and positions of the corresponding band notched elements. Furthermore, additional resonance at higher frequencies has been generated by introducing a metal loaded complimentary split ring resonator (MLCSRR) to the ground plane, so that it provides enhanced usable fractional bandwidth (2.6-13.9 GHz) more than 136%. The performance of the proposed antenna is analyzed both in frequency and time domain to assess its suitability in UWB communication.

Index Terms – Conductor backed plane, frequency band notch performance, Metal Loaded Complimentary Split Ring Resonator (MLCSRR), ultra wideband.

I. INTRODUCTION

Federal Communication Commission (FCC) has assigned the frequency range from 3.1 GHz to 10.6 GHz for ultra wideband (UWB) communication systems [1]. However, various band notched elements are applied to overcome the electromagnetic interference of WIMAX (3.3-3.7 GHz) and WLAN (5.15-5.825 GHz) in UWB system. Conductor backed plane (CBP) is one of the band notched elements. In previous literatures, different geometries of CBP have been discussed so far such as I-shaped [2], H-shaped [3], W-shaped [4] CBP structures. Introduction of split ring resonator (SRR) at the rear side of patch is the similar approach for band rejection [5]. Another common way of band notch technique is the application of open stub at the edge of the microstrip feed line; ground plane or patch has been discussed in recent investigation [6]. In this paper two different band notch elements are employed for dual band rejection purpose. First one is a vertically combined half wavelength T- and U-shaped conductor backed plane. The main advantage of the new modified CBP geometry is that it can efficiently control the rejection bandwidth of WIMAX frequency band (3.3-3.7 GHz) for deep and sharp rejection. Another stop band element for WLAN frequency band (5.1-6 GHz) is a quarter wave length rectangular spiral shaped open stub in the microstrip feed line. Bandwidth of the WLAN rejection band can be controlled by varying the open stub distance from patch. Moreover, a metal loaded CSRR is introduced to achieve much wider impedance bandwidth, especially at higher band. Metal loading technique with CSRR in ground plane generates additional resonant mode which ensures good impedance matching over the wide range of frequency 2.6-13.9 GHz (VSWR < 2).

II. ANTENNA DESIGN AND CONFIGURATION

The geometry of the proposed design with WIMAX band-notched ability is illustrated in Fig. 1. Antenna is printed on FR4 substrate with $\varepsilon_r = 4.4$ and thickness of 1.6 mm, which consists of a simple rectangular radiating patch, which is excited by a 50Ω microstrip feed line. To generate notch band around 3.5 GHz, a thin half wavelength on the rear side of the patch is electrically separated from the ground plane and patch. The conductor

Submitted On: September 16, 2016
Accepted On: January 16, 2017

backed plane geometry is a vertical combination of T- and U-shaped parasitic elements. The desired centered rejection frequency $f_{notch\text{-}wimax}$ at 3.5 GHz can be approximated as:

$$\mathbf{f_{notch\text{-}wimax}} = \frac{c}{2L_{CBP}\sqrt{\epsilon reff}}, \tag{1}$$

where $\epsilon_{reff} = (\epsilon_r+1)/2$, c = speed of light in free space, ϵ_r = relative permittivity of the substrate and $L_{CBP} = (L_1+L_3)/2+L_2+2L_4$. Similarly, to reduce the interference from the WLAN system, a rectangular spiral shaped quarter wavelength open thin stub is inserted to the microstrip feed line corresponding to the rejection frequency at 5.5 GHz. The total length of spiral stub (L_{STUB}) can be calculated by the empirically approximated formula as:

$$\mathbf{f_{notch\text{-}WLAN}} = \frac{c}{4L_{STUB}\sqrt{\epsilon reff}}, \tag{2}$$

where $L_{STUB} = X_1+X_2+X_3+X_4+X_5+X_6+X_7-7t$.

This work mainly focuses on the following two issues:

i) Proper control of filter bandwidth of rejection bands;
ii) Enhancement of impedance bandwidth using metal loaded CSRR type defective ground structure.

Sharpness of the rejection mechanism completely depends on the quality factor (Q-factor). Coupling gap (d_C) between horizontal arm of CBP and ground plane acts as resonator and introduces capacitive effect which offers series resonance band notch function around 3.5 GHz. Inductive reactance is offered by narrow metallic strip of CBP and the capacitive effect of coupling gap (d_c) is termed of equivalent series RLC resonance circuit. Strong coupling effect due to closer separation between the horizontal arm of CBP and the ground plane produces high capacitance value that conversely degrades that Q-factor and enhances the rejection bandwidth around 3.5 GHz. On the other hand, closer gap between the vertical arms of CBP significantly improves the capacitance value which leads to high Q-factor and sharp rejection around 3.5 GHz. At rejection frequency (5.5 GHz), the open circuited stub draws more current by presenting low impedance at its anchor. In case of increasing separation, both equivalent capacitance and Q-factor decrease which leads to the rejection bandwidth enhancement around 5.5 GHz. Regarding the defective ground structure (DGS), a rectangular complimentary split ring resonator has been loaded to the inner periphery of the ground plane with metal loading. In previous literature, several DGS geometries have been presented. In this work, an asymmetrical modified DGS is depicted by using a thin metal shorting strategy on single rectangular CSRR type DGS configuration. Additional current path in ground plane due to the metal loaded CSRR type DGS creates a resonance circuit. The combination of current path due to metal shorting effect and the presence of defect in the region of high electromagnetic fields lead to smaller equivalent inductance and capacitance; hence, higher resonance frequency can be obtained. This effect in turn leads to the enhancement of the impedance bandwidth.

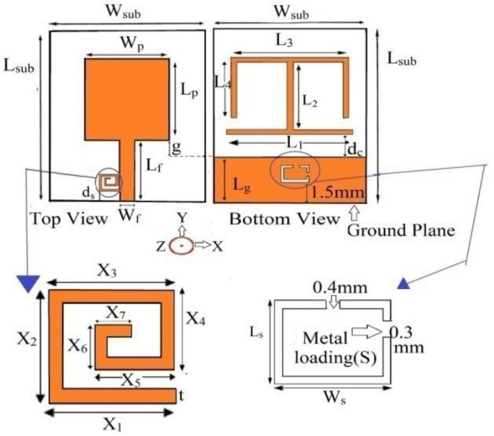

Fig. 1. Configuration of the proposed antenna.

III. FREQUENCY DOMAIN RESULTS

A parametric study of the frequency domain characteristics has been done by using Ansys HFSS simulator.

A. Effect of d_C & d_S in rejection band controlling

Figure 2 shows the effect of d_c and d_S in controlling of the bandwidth of individual rejection band around 3.5 GHz and 5.5 GHz.

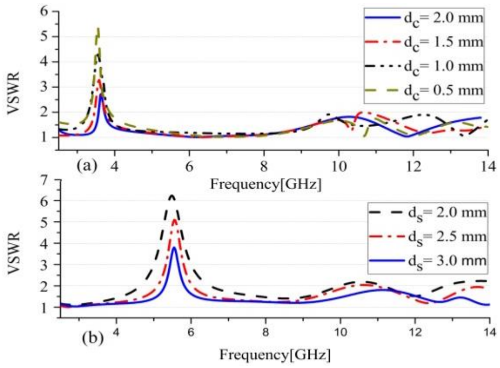

Fig. 2. Simulated VSWR for different value of: (a) d_c for controlling WIMAX rejection band, and (b) d_s for controlling of WLAN rejection band.

B. Enhancement of the impedance bandwidth

Figure 3 indicates the effect of CSRR with and without metal loading. It is observed that when a narrow metal strip is appropriately loaded with CSRR at optimum position, additional resonance at 11.7 GHz along with 10.6 GHz produces much enhanced bandwidth extended by approximately 3 GHz.

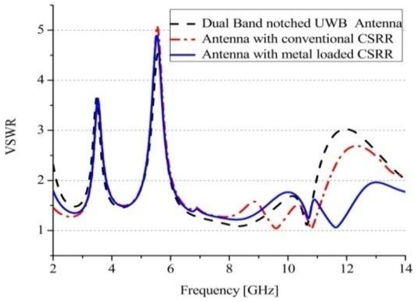

Fig. 3. Simulated VSWR characteristics for the antenna with and without metal loaded CSRR.

C. Variation of conductor backed plane parameter and stub length

The WIMAX band rejection can be tuned by changing the dimension of L_1, L_2, L_3 and L_4 independently as shown in Fig. 4. Similarly, WLAN rejection band can be controlled by varying the effective stub length L_{stub}, as shown in Fig. 5. It is worthwhile to mention that there is a low mutual coupling at two rejected frequencies indicating that each rejection frequency can be controlled independently.

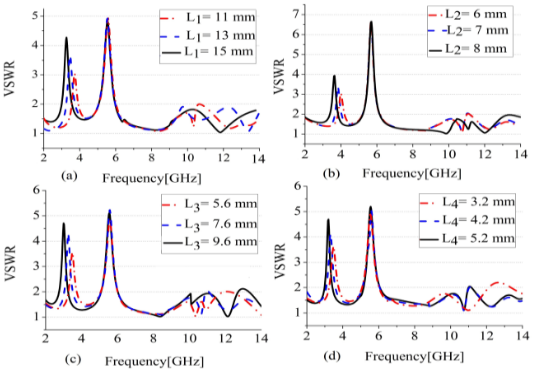

Fig. 4. Simulated VSWR with varying parameters: (a) L_1, (b) L_2, (c) L_3, and (d) L_4, (L_{stub}=10.4 mm).

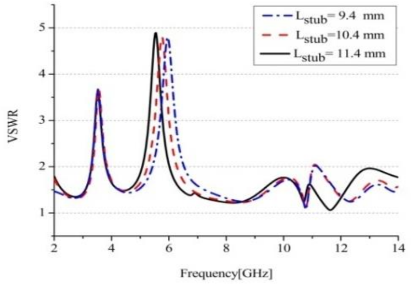

Fig. 5. Simulated VSWR for different value of L_{stub} (L_1=13 mm, L_2=7 mm, L_3=7.6 mm, L_4=4.2 mm).

D. Experimental result for VSWR

Figure 6 illustrates the prototype of proposed UWB band notched antenna with optimized dimension given in mm: L_{sub}=20, W_{sub}=20, L_f=7.5, W_f=2, L_P=12, W_P=10, Lg=4, L_1=13, L_2=7, L_3=7.6, L_4=4.2, g=3.5, d_c=0.5, d_g=2.5, X_1=2, X_2=2.5, X_3=1.7, X_4=1.7, X_5=1.2, X_6=1.2, X_7=6, t=3.

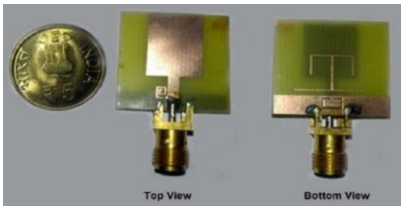

Fig. 6. Prototype of proposed antenna.

The measured and simulated VSWR of the proposed antenna with dual band notch characteristics are shown in Fig. 7. The measured frequency range covers the UWB range from 2.6 GHz-13.9 GHz with stop bands 3.3-3.7 GHz and 5.1-6 GHz, which cover the entire WIMAX and WLAN frequency band.

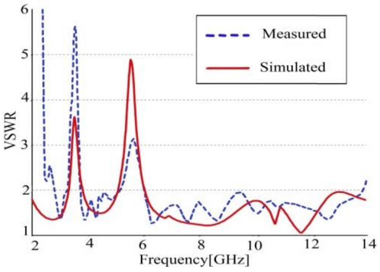

Fig. 7. Measured and simulated VSWR for the proposed antenna.

E. Measured radiation pattern and peak gain

The normalized measured far field radiation patterns are shown in Fig. 8. It is observed that H-plane patterns are fairly omni-directional over the entire frequency band and E-plane patterns are monopole like.

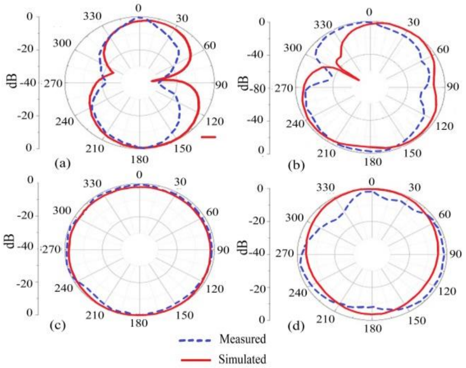

Fig. 8. Simulated and measured radiation pattern for the proposed antenna at: (a) E-plane 7 GHz, (b) E-plane 11 GHz, (c) H-plane at 7 GHz, and (d) H-plane at 11 GHz.

The measured peak gain of the proposed band notched antenna is shown in Fig. 9. It is noted that the proposed antenna exhibits gain variation from 0.2 dBi to 3.3 dBi, except two sharp dips at 3.5 GHz and 5.5 GHz.

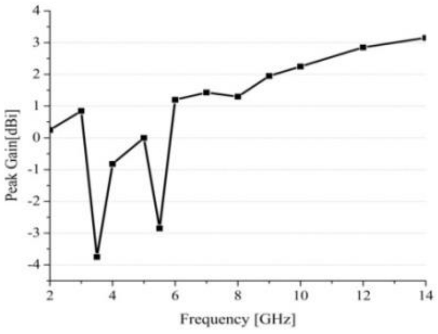

Fig. 9. Measured peak gain for the proposed antenna.

IV. TIME DOMAIN STUDY

Figure 10 illustrates the magnitude of transfer function and group delay characteristics between two identical antennas placed 30 cm apart in face to face and side by side orientation. In pass band, the group delay variation is less than 1 ns and the magnitude of transfer function is almost flat, which indicates the phase linearity between two antennas. However, large variation of group delay can be observed in stop bands with the sharp decrease in transfer function magnitude $|S_{21}|$, which is due to the band rejection characteristics.

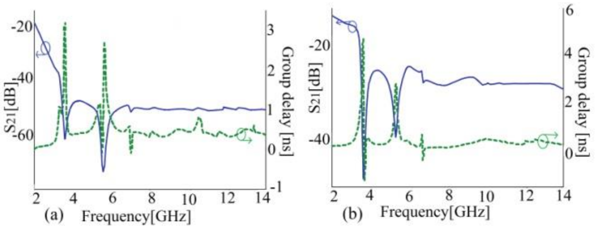

Fig. 10. Measured magnitude of the transfer function and group delay: (a) face-face and (b) side by side mode.

V. CONCLUSION

A monopole UWB antenna with enhanced impedance band width has been investigated and realized with controllable frequency rejection band centered at 3.5 GHz and 5.5 GHz. Metal loaded complimentary split ring resonator (MLCSRR) to the ground plane provides much wider impedance band width (2.6–13.9 GHz). The proposed antenna demonstrates superior performance in terms of frequency and time domain and therefore, it can be applicable in near future UWB wireless applications.

REFERENCES

[1] FCC, "Ultra-Wideband Operation FCC Report and Order," Tech. Rep. US 47 CFR Part 15, 2002.

[2] N. Choi, C. Jung, J. Byun, M. J. Park, Y. S. Chung, T. Kim, F. J. Harachiewicz, and B. Lee, "Compact UWB antenna with I-shaped band notch parasitic element for laptop application," *IEEE Antenna and Wireless Propagation Letter*, vol. 8 pp. 580-582, Aug. 2009.

[3] N. Ojaroudi and M. Ojaroudi, "Small square monopole antenna having variable frequency band-notch operation for UWB wireless communication," *Micowave and Optical Technology Letters*, vol. 54, no. 8, pp. 1994-1998, Aug. 2012.

[4] N. Ojaroudi, M. Ojaroudi, and N. Ghadimi, "Dual band-notched small monopole antenna with novel W-shaped conductor backed-plane and novel T-shaped slot for UWB application," *IET Microwaves, Antennas & Propagation*, vol. 7, no. 1, pp. 8-14, Jan. 2013.

[5] J. Y. Siddiqui and Y. M. M. Antar, "Compact SRR loaded UWB circular monopole antenna with frequency notch characteristics," *IEEE Transactions on Antennas and Propagation*, vol. 62, no. 8, pp. 4015-4020, Aug. 2014.

[6] M. Rahimi, R. A. Sadeghzadeh, F. B. Zarrabi, and Z. Mansouri, "Band-notched UWB monopole antenna design with novel feed for taper rectangular radiating patch," *Progress in Electromagnetics Research*, vol. 47, pp. 147-155, Feb. 2014.

ACES JOURNAL, Vol. 32, No. 12, December 2017

An Ultra-Wideband Absorber Backed Planar Slot Antenna

William O. Coburn

US Army Research Laboratory
Adelphi, MD 20783, USA
william.o.coburn.civ@mail.mil

Abstract **─** Planar antenna designs have many advantages such as low-profile, light-weight, and ease of fabrication and integration. Here, a planar slot antenna implemented on ceramic substrate with coplanar waveguide feed is considered. With absorber loading the design provides 50 Ω input impedance over the frequency range 0.3–3 GHz so it is considered ultra-wideband. This paper summarizes a numerical investigation using both frequency and time-domain solvers. The results serve to guide the future analysis of broadband antennas with lossy dielectric loading for ground penetrating radars. The evaluation of radar performance requires further simulation and model validation based on antenna measurements.

Index Terms **─** Ground Penetrating Radar, Method of Moments, microwave absorber, planar slot antenna, Time-Domain Finite-Difference.

I. INTRODUCTION

This paper investigates the numerical analysis of a planar slot antenna in the time- and frequency-domains using commercial solvers. FEKO (www.feko.info) is used for the frequency-domain solver while the GEMS Simulator (www.2comu.com) is used for the transient response. In free space the time-domain solver can be more efficient, but when calculating field penetration into the soil the problem space increases substantially. In addition, the time domain solver can have limitations or reduced accuracy when loading the antenna with high loss materials.

Planar slot antennas can have input impedance near 50 Ω over a broad bandwidth (BW) without additional impedance matching [1]. A metal reflector can also be used to increase directivity, but introduces gain variations as a function of frequency. For handheld ground penetrating radar (GPR) applications, the embodiment considered here is restricted in size to a 3-inch (76.2 mm) cube. A model was constructed using FEKO to modify the baseline shape resulting in an antenna size 75 mm (W) x 72 mm (L) with SMA edge connector.

II. ANTENNA DESIGN

The antenna is a coplanar waveguide (CPW) fed patch radiator exciting a rectangular slot. A broad frequency BW slot can be obtained by careful design of the structure exciting the slot and tapering the slot corners. A common implementation was presented in [2] shown in Fig. 1 (a), but the provided model parameters were not consistent with the fabricated antenna. Some parameters were modified resulting in the antenna model in Fig. 1 (b). The CPW line appears to be designed for a larger permittivity than described in [2]. The revised antenna size was increased by a factor of three and modified to improve the low frequency bandwidth as shown in Fig. 1 (c) with the prototype shown in Fig. 1 (d). The planar slot antenna with coaxial end-launch connector is modeled with a thin wire or an edge port. The CPW feed was adjusted to be on TMM10 having $\varepsilon_r = 9.2$ and $\tan\delta = 0.0022$ [3] with thickness 0.787 mm (31-mils). An edge port was used with FEKO as can be seen in Fig. 1, while GEMS used the same feed structure with a wire port to represent the SMA connector. Multiple CPUs were used with the required CPU times and RAM adjusted to be for a single processor and for symmetry when used. With this linear scaling GEMS required 1.53 CPU hours (0.22 GB RAM), while FEKO took 10.6 CPU hours (0.52 GB RAM) for 151 frequencies. The GEMS runtime was much shorter but only 27 far field patterns were calculated (requiring 7.7 min). In general, the time domain solver is more efficient for UWB antennas and the impedance transformed to the frequency domain can be done for an arbitrary number of frequencies.

This planar slot was simulated with FEKO and GEMS over the frequency range 0.3–3 GHz with the S_{11} comparison shown in Fig. 2 (a). The FEKO and GEMS results have similar frequency dependence and fair agreement in amplitude, but neither fully captures the measured impedance variations. GEMS obtains the measured low-frequency behavior but without absorber loading the antenna is not well matched. Adaptive or fine meshing was used in both codes and the GEMS residual signal converges to a level 54 dB below peak. Compared to the measured data, GEMS obtains an artificial result near 2.5 GHz, which is the largest error in return loss obtained with the time-domain solver (15 dB), while FEKO has a 3 dB discrepancy near 2.7 GHz.

Submitted On: February 9, 2015
Accepted On: January 16, 2016

Over the required BW the radiation pattern is stable becoming multi-lobed above about 3 GHz. However, the E-plane pattern tilts forward near 3 GHz as can be seen in Fig. 2 (b) where the realized gain at zenith is reduced at high frequency owing to a tilted main lobe. The measured boresight gain indicates a more tilted pattern shape. The oscillations observed in the measured gain are artifacts of the anechoic chamber being noise limited at certain frequencies.

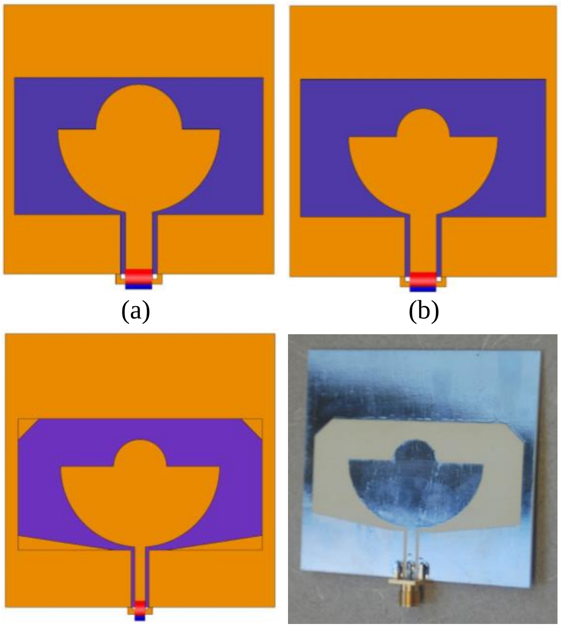
(a) (b)

(c) (d)

Fig. 1. Planar slot antennas: (a) original design [2], (b) modified version, (c) proposed design, and (d) fabricated antenna.

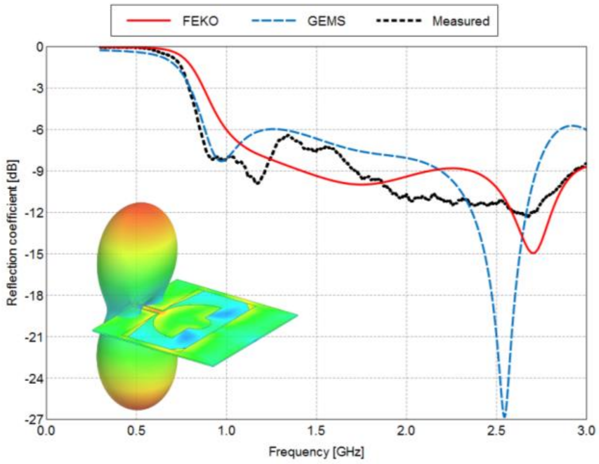

(a)

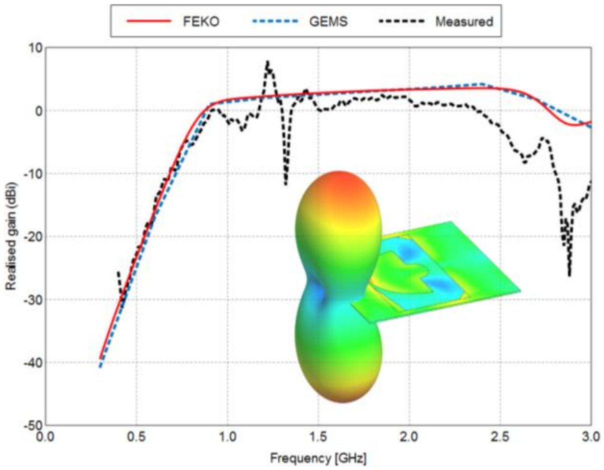

(b)

Fig. 2. Planar slot antenna on TMM10 substrate: (a) return loss and (b) realized gain vs. frequency.

III. ABSORBER LOADING

This structure has a larger impedance BW and higher gain compared to the radiator only as a planar monopole antenna. At low frequencies the antenna has the radiation pattern of a dipole with the electric (E-) field being parallel to the CPW feed. This antenna is loaded with a lossy dielectric 2.5-inch thick to extend the impedance BW to lower frequencies at the expense of antenna efficiency. A 3-layer graded microwave absorber, such as AN74 [4] is used with or without metal backing. The high loss layer ($\varepsilon_r = 3$ and $\tan\delta = 2$) is next to the antenna with the middle and last layers having less loss at $\varepsilon_r = 1.5$ and $\tan\delta = 0.5$ and $\varepsilon_r = 1.4$ and $\tan\delta = 0.45$, respectively. This 3-layer absorber is simulated in GEMS using $\varepsilon_r = 3$ with conductivity $\sigma = 0.24$ S/m with the same parameters used in FEKO for comparison. At low frequency both representations are similar and consistent with measured data. But as can be seen in Fig. 3, the graded absorber better represents the measured return loss above 1.5 GHz. The results indicate that for GPR applications the antenna is poorly matched at low frequency. The antenna transient excitation and radiated field indicate some late time ringing which can be mitigated by absorber loading. This loading requires a tradeoff between impedance matching at low frequencies and antenna efficiency and should be measured to determine adequate radar performance. Ground penetrating radars typically operate over a decade impedance BW with antennas in close proximity to the soil. Thus, the absorber loading and slightly tilted main beam may not hinder performance for this application.

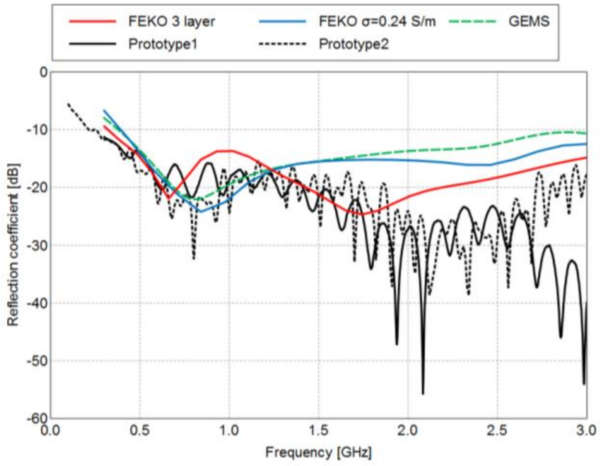

Fig. 3. Planar slot antenna on TMM10 substrate return loss with microwave absorber.

The gain at zenith vs. frequency is shown in Fig. 4 without metal backing for constant conductivity, σ = 0.24 S/m. The results indicate that the absorber parameters vs. frequency are not known exactly and should be measured. The simulation results are in good agreement but the measured gain is less than predicted indicating higher loss than assumed. The results with absorber and metal backing are shown in Fig. 5 where the metal backing introduces gain variations with frequency. The design requires a tradeoff between impedance matching at low frequencies and antenna efficiency. A customized absorber with known frequency dependence may be required to optimize performance with this antenna.

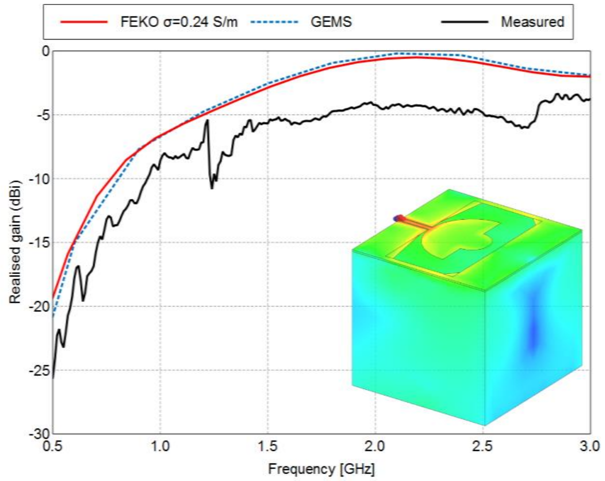

Fig. 4. Absorber loaded planar slot antenna realized gain on boresight vs. frequency.

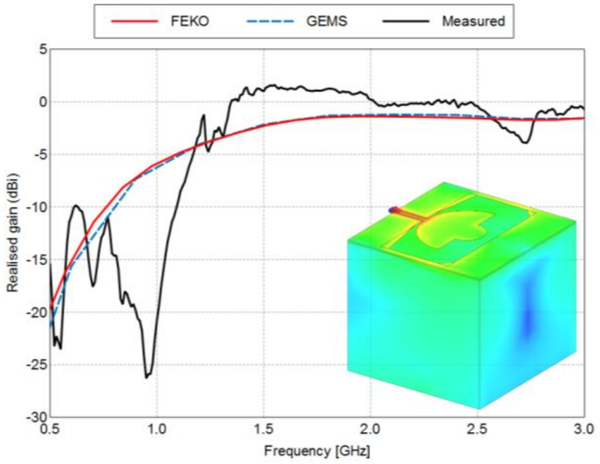

Fig. 5. Absorber loaded slot antenna with metal backing realized gain on boresight vs. frequency.

IV. CONCLUSION

The UWB antenna is a critical component for GPR systems and should radiate a sharp pulse with low reverberation (ring down) from multiple reflections over the antenna structure [5]. The design objective is complicated by physically (and electrically) small antenna requirements for hand-held systems. Both time and frequency domain codes produce similar results indicating that this antenna would require lossy dielectric loading to avoid ringing from the edges. This is common practice to sacrifice antenna efficiency for broad impedance BW and flat gain response over the required frequency band. Although some of the measured gain variations are artificial, a frequency dependent absorber will be used in future simulations to better capture the measured frequency dependence.

REFERENCES

[1] K. L. Wong, *Compact and Broadband Microstrip Antennas*, John Wiley & Sons, New York, 2002.

[2] M. Koohestani and M. Golpur, “Very ultra-wideband printed CPW-fed slot antenna,” *Electronics Letters*, vol. 45, no. 21, October 2009.

[3] Rogers Corp., *TMM Thermoset Microwave Materials Datasheet*, (www.rogerscorp.com).

[4] N. Rahman, A. Sharma, M. Afsar, S. Palreddy, and R. Cheung, “Dielectric characterization and optimization of wide-band, cavity-backed spiral antennas,” *ACES Journal*, vol. 26, no. 2, pp. 123-130, February 2011.

[5] L. Gurel and U. Oguz, “Simulation of ground-penetrating radars over lossy and heterogeneous grounds,” *IEEE Trans. Geosci. Remote Sensing*, vol. 39, no. 6, pp. 1190-1197, June 2001.

Simple Configuration Low-pass Filter with Very Wide Stop Band

Behrooz Fath Ganji [1], Mahya Samadbeik [2], Abbas Ramezani [1], and Abdolmajid Mousavi [1]

[1] Department of Electrical Engineering
University of Lorestan, Kamalvand, Khorramabad, Lorestan, Iran
Ganji.behrooz@yahoo.com, Ramezani.ab@lu.ac.ir, mousavi.m@lu.ac.ir

[2] Department of Electrical and Engineering
West Tehran Islamic Azad University, Tehran, Iran
Samadbeik.m@gmail.com

Abstract ─ In this paper, a compact microstrip low-pass filter with elliptic-function response is presented. A half-ring along with two half-elliptic patch resonators is cascaded to design a compact low-pass filter with very wide stop band and high selectivity in a small circuit area. This filter has the stop band from 3.3 up to 27.57 GHz with attenuation level better than -20 dB. The proposed filter has low insertion loss in the pass band and stop band, high return loss (RL), and very wide rejection in the stop band, along with compact size and simple configuration .The filter is designed, fabricated and measured. Simulation and measurement results are presented and compared to previous researches. The results of simulations and measurements are in agreement.

Index Terms ─ Low-pass filter, microstrip components, semi-elliptic resonator, semi-ring resonator, stop band range.

I. INTRODUCTION

In new days microwave communication systems, microstrip low-pass filter (LFP) has a vital importance improving the performance of such systems. Compact size low-pass filters with high rejection and low insertion loss are important in developing the modern microwave communication systems.

Recently, studies on low-pass filter have been reported with different configurations in microwave applications. To achieve sharp response, we use multiple cells; these increments enlarge the size of the circuit and insertion loss in the pass band region of the proposed filter in [1]. In [2], the traditional low-pass filters produce slow roll-off and narrow stop band. In [3], a microstrip low-pass filter with a small size and mostly wide stop band using cell resonator has been introduced. The main disadvantage of this filter is the low rejection and the existence of harmonic in the stop band. The presented low-pass filter in [4] which uses the half-elliptic patch resonator, in spite of having an appropriate sharp roll-off and mostly wide stop bandwidth has a large size of the circuit and an unsuitable return loss. The low-pass filter in [5] which has been designed by the means of the hairpin resonator contains a harmonic and improper level suppression in the stop band having a high insertion loss. Also, in this filter, the defected ground structure cannot be etched on the metal surfaces. Compact quasi-elliptic microstrip LPF in [6] does not have sharp response, and has inadequate attenuation level in the stop band. The presented LPF in [7] which has been designed by the aid of half-circular and half-elliptic patch resonator is proposed to achieve wide stop band and sharp response. Despite the above mentioned advantages, the return loss in the pass band and the size of the filter is not suitable. The presented filter by the use of tub in hairpin resonator with radial stubs in [8], despite its small size, contains a low return loss in the pass band, and stop bandwidth with -20 dB suppression level is unsatisfactory. In [9], there is not sharp response and low insertion loss. In [10], measured result show that the design filter has a better than -10 dB stop band rejection but the new filters design with -20 dB attenuation level. The results in [11] are acceptable but quantity of cut-off frequency is about 4.24 GHz that is high value for design filter.

In this work, we have attempted to improve the major filter parameters by decreasing the filter size, simple configuration, decreasing the insertion loss, increasing the return loss and rising the stop bandwidth with a high rejection. The mentioned filter has been designed and manufactured using a semi-ring resonator and two semi-elliptic resonators with different size. The stop bandwidth is from 3.3 GHz to 27.57 GHz with under -20 dB suppression level. This filter was manufactured after designing and the experimental results have been measured. Measured and simulated S-parameters are in agreement.

II. DESIGN OF PROPOSED FILTER

The designed filter is shown in Fig. 1 (a) and designed

Submitted On: March 1, 2015
Accepted On: December 13, 2015

filter's dimensions are as follows: $R_1 = 1.75$ mm, $R_2 = 4.25$ mm, $L_1 = 0.2$ mm, $W_0 = g = 0.1$ mm. Figures 1 (b) and 1 (c) illustrate the simulation results of S_{21} of the designed resonator against W_0 and R_1.

Figure 1 (b) shows that by changing the value of W_0, the location of cut-off frequency and transmission pole can be controlled, with increasing of W_0 from 0.1 to 0.3 mm with steps of 0.1 mm, transmission zero in 3.6 GHz will approach the upper frequency. The effect of R_1 on the frequency response of resonator is shown in Fig. 1 (c).

It can be observed that the cut-off frequency is affected by the R_1. In fact, the existence of R_1 is the basis of the designed resonator. The performance of the resonator is affected by the narrow line located along with the radius of the semi-ring patch. The narrow line is used to create equivalent inductance. Compared to the microstrip resonator in [4] & [7] the proposed resonator is more compact in size.

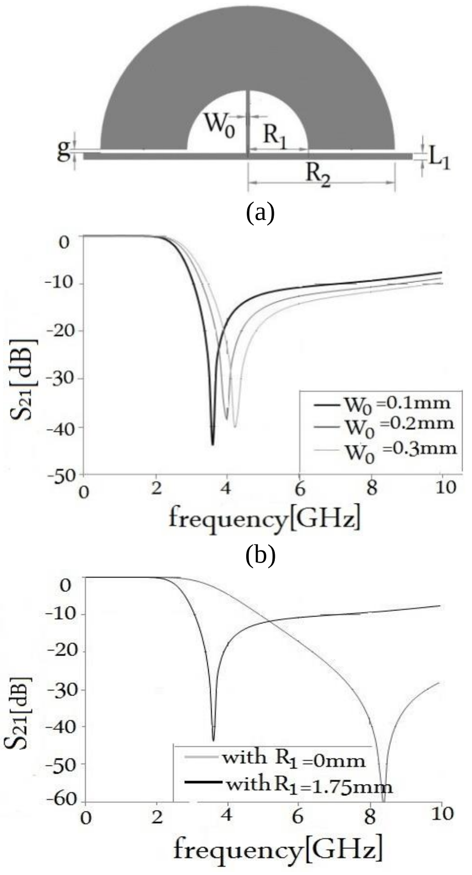

(a)

(b)

(c)

Fig. 1. (a) Schematic diagram of the designed filter, (b) simulation results for S_{21} with variation of W_0, and (c) simulation results for S_{21} with variation of R_1.

Compact size, simple configuration, high return loss and low insertion loss in the pass band are the advantages of the designed resonator. The designed semi-ring resonator has a low stop bandwidth which reaches to high rejection level and ultra wide stop band with the addition of two semi-elliptic resonators with different size in series.

III. SIMULATION AND MEASUREMENT

Figures 2 (a) and 2 (b) show the designed filter and fabricated filter respectively. Two other patches dimensions are as follows: $R_3 = 3.49$ mm, $R_4 = 3.73$ mm, $R_5 = 2.19$ mm, $R_6 = 2.03$ mm, $W_1 = 1$ mm, $W_2 = 0.45$ mm, $W_f = 1.65$ mm, $L_f = 0.7$ mm, $L_2 = 0.4$ mm, $L_3 = L_4 = 0.2$ mm, $L_5 = L_6 = 0.2$ mm. Simulated and measured results of designed filter are illustrated in Fig. 2 (c).

In order to impedance match, a pair of open microstrip stubs are fabricated at both sides of the LPF, so that the 50 Ω impedance at the input and output ports of the designed filter achieved, with the width $W_f = 1.65$ mm and length $L_f = 0.7$ mm.

For fabricating of the deigned filter, a substrate with a relative dielectric constant $\varepsilon_r = 2.2$, thickness $h = 0.508$ mm, and loss tangent $\tan\delta = 0.0009$ is used. ADS used to simulate the results of designed filter. Agilent network analyzer N5230A is used to measure the S-parameters. Figure 2 (c) illustrating the simulated and measured results of the designed filter. It can be seen from figures that the designed filter has -3 dB cut-off frequency equal to 2.71 GHz, insertion loss less than approximate 0.3 dB in the pass band from DC to 1.81 GHz, by return loss about 16.55 dB and suppression level more than -20 dB from 3.3 GHz to 27.57 GHz that shows we achieve a ultra wide stop band and a proper suppression harmonic in the designed filter. The transition band is 0.59 GHz, from 2.71 to 3.3 GHz with -3 dB and -20 dB, respectively, which shows that the designed filter reaches a proper performance. The designed filter has a transmission zero at 3.48 GHz with attenuation level of -57.66 dB. Compared to the LPF in [7], our designed low-pass filter has 56% size reduction (considering input and output ports), along with 58% increase in stop bandwidth with -20 dB suppression level, 43% improved in return loss and also the configuration of the proposed filter is simpler than those of in [7]. The designed filter size is 21.11×4.55 mm^2.

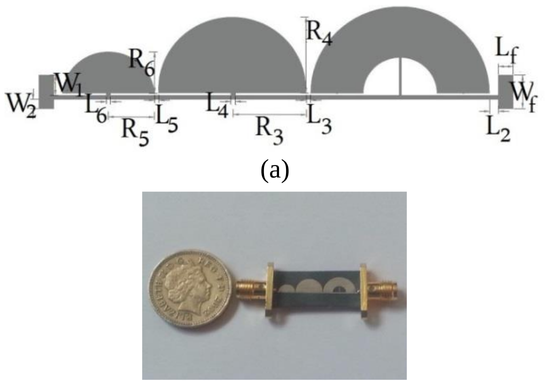

(a)

(b)

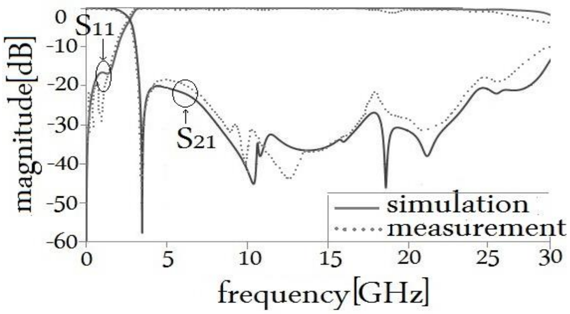

(c)

Fig. 2. (a) Schematic of the designed filter, (b) photograph of fabricated filter, and (c) simulation and measuring results.

Table 1 shows the performance comparison between the proposed filter and other reported LPFs. In Table 1, ζ RSB, NCS, SF, AF, FOM and RL correspond to the roll-off rate, stop band bandwidth, normalized circuit size, suppression factor, architecture factor, figure of merit and respectively [11]. The roll-off rate is given by:

$$\zeta = \frac{\alpha_{\max} - \alpha_{\min}}{f_s - f_c}, \tag{1}$$

where $\alpha_{\max}$ is the 20 dB and $\alpha_{\min}$ is the 3 dB. F_c and f_s are the -3 dB cut-off frequency and -20 dB stop band frequency. The relative stop band bandwidth (RSB) is defined as:

$$\mathrm{RSB} = \frac{\text{stop band bandwidth}}{\text{stop band centre frequency}}. \tag{2}$$

The suppression factor (SF) shows the stop band suppression level divided by 10:

$$\mathrm{SF} = \frac{\text{rejection level}}{10}. \tag{3}$$

The normalized circuit size (NCS) is defined as:

$$\mathrm{NCS} = \frac{\text{physical size (length} \times width)}{\lambda^2{}_g}, \tag{4}$$

where λ_g is the guided wavelength at -3 dB cut-off frequency. The architecture factor (AF) is the complexity factor of the circuit, which is defined as 1 when the design is 2D and as 2 when the design is 3D. Finally, the figure of merit (FOM) is the overall index of the proposed filter, which is defined as:

$$\mathrm{FOM} = \frac{\mathrm{RSB} \times \zeta \times SF}{\mathrm{AF} \times NCS}. \tag{5}$$

Table 1: Performance comparisons between published works and proposed filter

Ref.	Fc (GHz)	ζ	RSB	NCS	SF	FOM	RL (dB)
7	3.12	30.35	1.35	0.059	2	1388.9	11.5
8	1.67	21.21	1.42	0.010	1	3011.82	12
9	2	14	1.35	0.0093	1	2032.25	11
10	2	43.9	1.636	0.0151	1	4788	13
This Work	2.71	28.81	1.57	0.0174	2	5199	16

This filter can be used in applications in which a wide stop band is necessary. Experimental and simulated results are in agreement.

IV. CONCLUSION

In this new designed filter, we have used a half-ring resonator and two half-elliptic resonators in series. This LPF is designed and fabricated in a way that is in a good consistent with the simulation results and the experimental sample. In the designed filter, parameters such as size, stop bandwidth, configuration, return loss and insertion loss have been improved. Return loss in the pass band is about 16.55 and stop bandwidth with -20 dB suppression level is satisfactory. Experimental and simulated results are in agreement. The compact size and ultra wide stop band of the proposed filter make it a good choice for microwave communication systems.

REFERENCES

[1] D. M. Pozar, “Microwave filters,” *Microwave Engineering*, 4th ed., D. M. Pozar, pp. 550-582, New York, Wiley, 1998.

[2] J. S. Hong and M. J. Lancaster, *Microstrip Filters for RF/Microwave Applications*, New York: Wiley, 2001.

[3] K. Deng, Q. Xue, and W. Che, “Improved compact microstrip, resonance cell low-pass filter with wide stop band characteristics,” *Electron. Lett.*, vol. 43, no. 8, pp. 463-464, 2007.

[4] J.-L. Li, S.-W. Qu, and Q. Xue, “Compact microstrip low-pass filter with sharp roll-off and wide stopband,” *Electron. Lett.*, vol. 45, no. 2, pp. 110-111, 2009.

[5] F. Wei, L. Chen, X.-W. Shi, Q.-L. Huang, and X.-H. Wang, “Compact low-pass filter with wide stopband using coupled-line hairpin unit,” *Electron. Lett.*, vol. 46, no. 1, pp. 88-90, 2010.

[6] J. Wang, L. J. Xu, S. Zhao, Y. X. Guo, and W. Wu, “Compact quasi-elliptic microstrip low-pass filter with wide stop band,” *Electron. Lett.*, vol. 46, pp. 1384-1385, 2010.

[7] M. Hayati, A. Sheikh, and A. Lotfi, “Compact low-pass filter with wide stop band using modified semi-elliptic and semi-circular microstrip patch resonator,” *Electron. Lett.*, vol. 46, pp. 1507-1509, 2010.

[8] X. B. Wei, P. Wang, M. Q. Lin, and Y. Shi, “Compact wide-stop bandlow-pass filter using stepped impedance hairpin resonator with radial stubs,” *Electron. Lett.*, vol. 47, iss. 15, pp. 862-863, 2011.

[9] M. H. Yang, J. Xu, Q. Zhao, L. Peng, and G. P. Li, “Compact broad-stop bandlow-pass filters using sirs-loaded circular hairpin resonators,” *Pier 102*, pp. 95-106, 2010.

[10] F. Wei, L. Chen, and X.-W. Shi, “Compact low-pass filter based on coupled-line hairpin unit,”

Electron. Lett., vol. 48, 2012.

[11] M. Hayati, S. Naderi, and F. Jafari, "Compact microstrip low-pass filter with sharp roll-off using radial resonator," *Electron. Lett.*, vol. 50, no. 10, pp. 761-762, 2014.

GA Optimization of the Optical Directional Coupler

Pinar Ozkan-Bakbak

Department of Electronic and Communication Engineering
Yildiz Technical University, Istanbul, 34220, Turkey
pozkan@yildiz.edu.tr

Abstract **─** Optical couplers, which are passive devices, couple optic waves through optical waveguides and can be employed in many applications, including power splitters, optical switches, wavelength filters, polarization selectors, etc. In this work, a simple, fast and instant optimization design is presented for an optical directional coupler based on Genetic Algorithms (GA). This optimization design is preferred due to its favourable usage and fast convergence capability. Finally, the designed methodology has been analytically and experimentally evaluated and the results show that the GA is an advantageous method for designing an optical element where the measurable data is obtainable instead of complex formulas.

Index Terms **─** Genetic Algorithm, optical directional coupler.

I. INTRODUCTION

An optical directional coupler, which consists of two parallel optical fibers or two bent or one straight and one bent optical fibers, is a four-port circuit element and is fed by a laser or a light emitting diode at one of the ports. However the data transmission is provided through the other three ports. Due to interaction within the optical fibers, there is a periodic exchange of power between the two waveguides [1-6].

The IN 1 is the input port, OUT 1 is the output port, OUT 2 is the coupled port and IN 2 is the isolated port, as seen in Fig. 1.

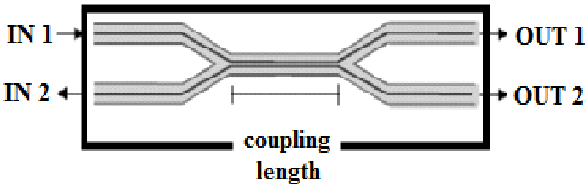

Fig. 1. The general model for directional couplers.

The concept of coupled modes at electromagnetic problems have emerged in the 1950's. The application of the coupled mode theory to optical waveguides had started by Vanclooster and Phariseau [4]. Marcuse, who worked on the interaction mechanism of parallel optical waveguides, contributed to the literature on coupled power equations [5]. The implementation of coupled mode theory to the optical waveguides can be found within Snyder and his working group studies. By increment the importance of directional couplers, especially after 1970, there are many studies in the literature on this subject [6].

A simple, fast and evolutionary structural optimization, which is based on Genetic Algorithms (GA), is described for optimization part. This optimization design is preferred due to its favourable usage and fast convergence capability [7]. The GA method can be applied by using a fitness function (FF). If the optimization is a minimization problem, the FF can be renamed as cost function (CF).

The remainder of this paper is organized as follows: In Section 2, the coupling mechanism between two optical directional coupler is analysed by using the coupled mode theory and perturbation theory. The interaction between the couplers, which consists of identical, slab, parallel, weakly guiding, lossless and uncladded optical waveguides, is analysed for a time dependent term of $\exp(jwt)$. TE even and odd, TM even and odd modes are determined in the slab and identical optic guides [1-6]. The propagation constant change is analysed to be used in the optimization as CF. In Section 3, the applicability of GA optimization in the optical directional coupler is investigated and concluded successfully. The comments on the results are explained in Section 4 and determined that the GA optimization results are compatible with the modal analysis results.

II. COUPLING ANALYSIS IN OPTICAL DIRECTIONAL COUPLER

In this study, the coupling is analyzed by using the coupled mode theory and perturbation theory. Perturbation theory is a mathematical method often used to obtain approximate solutions to equations for which no exact solution is possible, feasible or known. Detailed information about perturbation theory for solutions in optic can be found in [8]. Coupled mode theory is the

Submitted On: April 1, 2015
Accepted On: February 3, 2016

perturbational approached analyses for the coupling of the systems [1-6, 9].

The parameters for the proposed optical directional coupler are seen in Fig. 2. The weakly guiding optical waveguides are also thought to be weakly coupled to each other and the approximate field expressions in wave guides are adopted independent of polarization. In the weak coupling analysis, process is facilitated through ignoring the modes in the opposite direction. The coupling will be investigated in space domain.

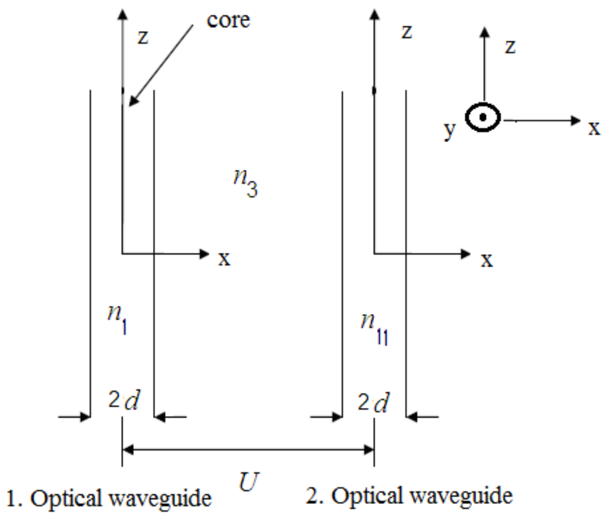

Fig. 2. The coupling between two parallel, identical, slab, weakly guiding, lossless and uncladded optical waveguides. The power reflection coefficient versus groove size.

The amplitude functions of the modes in the first and second optical waveguides are given with the propagation constants β for a time dependent term of $\exp(jwt)$ as follows:

$$a_i(z) = a_0 \exp(-j\beta_i z) \qquad i=1,2. \tag{1}$$

In lossless optic waveguides β values are real values [9] and the analyses are in space domain as follows:

$$da_i / z = -j\beta_i a_i, \tag{2}$$

where the coupling equations are:

$$da_1 / z = -j\beta_1 a_1 + c_{12} a_2, \tag{3}$$

$$da_2 / z = -j\beta_2 a_2 + c_{21} a_1. \tag{4}$$

Here c_{12} and c_{21} are the coupling coefficients. c_{12} is the effect of II optical waveguide to I optical waveguide per unit length, and c_{21} is the effect of I optical waveguide to II optical waveguide per unit length.

TE and TM modes are examined as a result of solving the Maxwell equations, Helmholtz equations and boundary conditions through optical waveguides [1-6].

TE even and odd guided field definitions in the waveguides in the core and the surrounding area respectively are as follows:

$$E_y = \begin{cases} A\begin{cases}\cos(\kappa x) \\ \sin(\kappa x)\end{cases} & 0 \le x \le d, \\ , & \\ B\exp\left(-\gamma(|x|-d)\right) & d \le x \le \infty, \end{cases} \tag{5}$$

where κ is the is the eigenvalue of core region and γ is the eigenvalue of the region surrounding the cores.

TM even and odd guided field definitions in the waveguides in the core and the surrounding area respectively are as follows:

$$H_y = \begin{cases} A\begin{cases}\cos(\kappa x) \\ \sin(\kappa x)\end{cases} & 0 \le x \le d, \\ , & \\ B\exp\left(-\gamma(|x|-d)\right) & d \le x \le \infty. \end{cases} \tag{6}$$

The propagation constant change of identical modes through identical waveguides in accordance with Maxwell's equations when the quadratic small terms are neglected:

$$\Delta\beta = \pm\frac{\omega\varepsilon_0}{4P}\int_{-\infty}^{+\infty}\int_{-\infty}^{+\infty}\left(n_{\mathrm{II}}^2 - n_3^2\right)E_2^* E_1 dxdy. \tag{7}$$

P is the modes' power, n_I is the refractive index of the first waveguide, n_{II} is the refractive index of the second waveguide, n_3 is the refractive index of the region surrounding the cores. n_I and n_{II} are the equal values for providing the identicalness. The propagation constant change for TE even and odd modes is given below:

$$\Delta\beta = \frac{k_0^2}{4\gamma}\left(n_{\mathrm{I}}^2 - n_3^2\right)\left[\frac{\gamma^2}{\beta^2(1+\gamma d)^2}\right]^{1/2}\begin{Bmatrix}\cos^2(\kappa d) \\ \sin^2(\kappa d)\end{Bmatrix} \tag{8}$$

$$\exp^2(\gamma d)\exp(-\gamma U),$$

and the propagation constant change for TM even and odd is given below:

$$\Delta\beta = \frac{\omega^2\varepsilon_0^2 n_{\mathrm{I}}^2\left(n_{\mathrm{I}}^2 - n_3^2\right)}{4\gamma}\frac{1}{\beta\left(d + \dfrac{n_{\mathrm{I}}^2 n_3^2}{\gamma}\dfrac{\kappa^2+\gamma^2}{n_3^4\kappa^2 + n_{\mathrm{I}}^4\gamma^2}\right)} \tag{9}$$

$$\begin{Bmatrix}\cos^2(\kappa d) \\ \sin^2(\kappa d)\end{Bmatrix}\exp^2(\gamma d)\exp(-\gamma U).$$

The modes corresponding to azimuthal mode number υ=1 are investigated for this study. V_c is the normalized frequency and the relation is given as follows:

$$(\kappa d)_c \cong V_c = \upsilon\frac{\pi}{2} \qquad \upsilon = 0,1,2,3.. \tag{10}$$

III. GA OPTIMIZATION OF THE OPTICAL DIRECTIONAL COUPLER

GA is an evolutionary algorithm that mimics the natural evolution such as inheritance, mutation, selection and crossover. The algorithm steps are simplified as:

- Randomly initialize the population and determine the fitness.
- Repeat the following steps until best individual is good enough:
    - Select the parents from the population,

- Perform the crossover on the parents creating the population,
- Perform the mutation of the population,
- Determine the fitness of the population.

GA has become a very popular optimization as it can be employed to various areas and provide global research in the solution spaces. The basic principles and applications in computer systems were presented by Holland [10] and de Jong [11] in 1975 and described in detail by Goldberg [12]. GA solver from Matlab toolbox is used in this study where we can also find multi objective GA which is concerned with the minimization of multiple objective functions.

GA solver finds the optimum results that gives the optimum propagation constant change with the relevant parameters. The CF is formulated by:

$$Cost\ Function = \min|\Delta\beta|. \tag{11}$$

Design parameter values in this coupling study are given as follows:

Operation frequency = 200 THz

$n_{I} = n_{II} = 1.5, \qquad n_3 = 1.49,$

$U_1 = 135\mu m, \quad U_2 = 135.3\mu m, \quad U_3 = 135.8\mu m.$

The rest parameters are equal in all simulations for good comparison.

TE and TM modes are analyzed and optimized via GA Matlab Solver in Figs. 3-6, where the compatible results of propagation constant change are figured due to the optical waveguide radius. Moreover Table 1 gives the accuracy percentage of GA results in comparison with the analytical results of each modes.

Table 1: Accuracy of GA

Accuracy of GA	Even (% Accuracy)	Odd (% Accuracy)
TE modes	99.56	99.65
TM modes	99.57	99.65
Average accuracy: % 99.60		

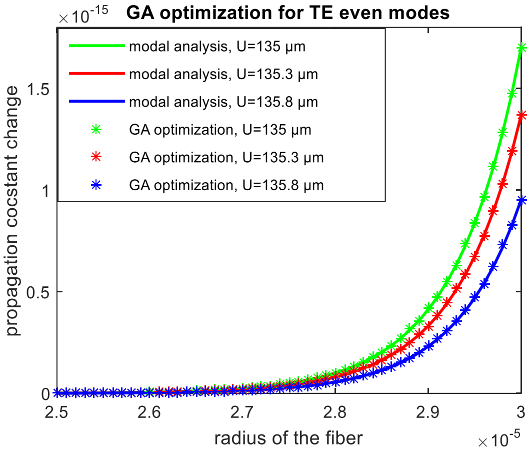

Fig. 3. GA optimization results catch the modal analysis results with high accuracy for TE even modes.

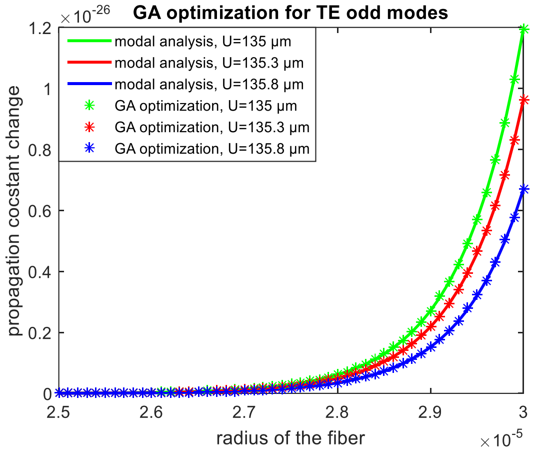

Fig. 4. GA optimization results catch the modal analysis results with high accuracy for TE odd modes.

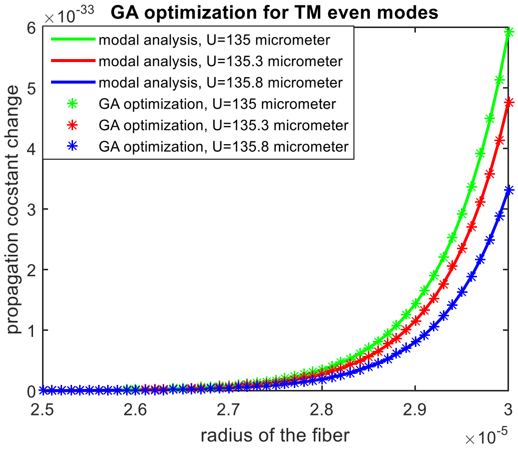

Fig. 5. GA optimization results catch the modal analysis results with high accuracy for TM even modes.

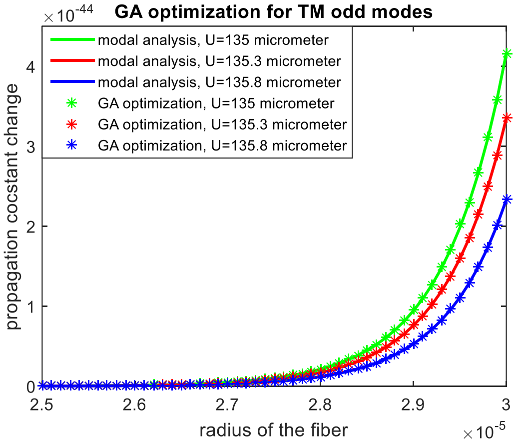

Fig. 6. GA optimization results catch the modal analysis results with high accuracy for TM odd modes.

IV. CONCLUSION

As a reminder, identical guides and equal parameters are employed to see comparative results. It is known via the modal analysis, the coupling between TE modes is more efficient than the coupling between TM modes. Moreover the coupling between even modes is more efficient than the coupling between odd modes. In addition, the propagation constant change increases with the radius of the fiber. As it is observed from the figures that GA results are in agreement with the analytical results. Thus, GA is a fast, simple, helpful and alternative method for designing a complex optical directional coupler. Consequently, GA can be enhanced in optical systems for the independent and automated processes.

REFERENCES

[1] A. W. Snyder and J. D. Love, *Optical Waveguide Theory*, J. W. Arrowsmith Ltd., Bristol, 1983.

[2] W. H. Louisell, *Coupled Mode and Parametric Electronics*, John Wiley & Sons, New York, 1960.

[3] Yariv, “Coupled mode theory for guided wave optics,” *IEEE J. Quantum Electron*., vol. QE9, no. 9, pp. 919-933, 1973.

[4] R. Vanclooster and P. Phariseau, “Coupling of two parallel dielectric fibres. I and II,” *Physica*, vol. 47, pp. 485-501, 1970.

[5] D. Marcuse, “Pulse propagation in multimode dielectric waveguides,” *Bell System Technical Journal*, vol. 51, no. 6, pp. 1199-1232, 1972.

[6] B. E. Little and W. P. Huang, “Coupled-mode theory for optical waveguides,” *Progress in Electromagnetic Research PIER 10*, pp. 217-270, 1995.

[7] J. M. Johnson and Y. Rahmat-Samii, “Genetic algorithms in engineering electromagnetics,” *IEEE Antennas and Propagation Magazine*, vol. 39, no. 4, pp. 7-21, 1997.

[8] D. A. B. Miller, *Quantum Mechanics for Scientists and Engineers*, Cambridge University Press, 2008.

[9] W. P. Yuen, “On the different formulations of the coupled mode theory for parallel dielectric waveguides,*” J. Lightwave Tech*., vol. 12, no. 1, pp. 82-85, 1994.

[10] J. H. Holland, *Adaptation in Natural and Artificial Systems*, MIT Press, 1975.

[11] K. A. De Jong*, An Analysis of the Behavior of a Class of Genetic Adaptive Systems*, Ph.D. thesis, University of Michigan, Ann Arbor, MI, USA, 1975.

[12] D. E. Goldberg, *Genetic Algorithms in Search*, Optimization and Machine Learning, Addison-Wesley, USA, 1989.

Phased Array Beam Steering Through Serial Control of the Phase Shifters

Randy L. Haupt

Department of Electrical Engineering and Computer Science
Colorado School of Mines, Golden, CO 80303, USA
rhaupt@mines.edu

Abstract **─** The commands to control the phases shifters in a phased array can be sent through a parallel or serial channel. Parallel commands simultaneously change the phase shifters, allowing the beam to nearly instantaneously hop from one direction to another. If a serial channel is used, then the commands are sequentially sent to the phase shifters. The sequential approach causes the beam to gradually move from one position to another, rather than the quick hop encountered with a parallel channel. This paper shows simulated results of the behavior of the array factor due to serial phase shifting and effects the element sequence has on that behavior and a method to optimize the command sequence.

Index Terms **─** Antennas, beamforming, genetic algorithm, linear array, phase steering, phased array, planar array.

I. INTRODUCTION

Phased arrays steer the main beam of the antenna by placing a linear phase shift across the elements. When the signals from all the elements add in phase, then this coherent addition results in a main beam peak. Phase steering began in the early 1930's when, the nulls of a two element array were steered by using a calibrated variable phase changer in order to determine the direction of arrival of a signal [1]. Today's digitally controlled phased arrays use state-of-the-art MIMC technology with phase shifters, amplifiers, and attenuators in the same module [2].

Commanding the phase shifters, especially for a large array, is a very complex engineering design. The commands may be sent to the element phase shifters over a parallel or serial control channel [3]. If the commands are sent in parallel, then all the phase shifters change at once. Serial phase shifting switches one phase shifter at a time in the array. Parallel phase shifter control is generally much faster than serial control, because a serial link transmits less data in one clock cycle than a parallel link. Unlike parallel control, serial control requires less hardware, is cheaper, occupies less space, has less crosstalk, and being asynchronous, clock skew is not an issue. Implementing serial phase shifting in place of parallel phase shifting may save cost and complexity for an array.

This paper explains the implications of serial phase shifting upon the array pattern during beam steering by a phased array. Mutual coupling, element patterns, phase shifter quantization, and bandwidth are ignored in order to isolate the effects on the array factor due to strobing one phase shifter at a time. The next section describes the effects on the array pattern of serial phase shifting in linear and planar arrays. Section III has an example that demonstrates how to reduce the main beam wandering due to serial phase shifting by sending nonsequential commands to the phase shifters. The order of the commands can be further optimized to reduce main beam wandering.

II. SERIAL PHASE SHIFTER CONTROL IN LINEAR ARRAYS

The effects of serial and parallel phase shifting can be demonstrated using the array factor formulation. An *N* element uniform linear array factor is given by:

$$AF=\sum_{n=1}^{N}e^{j(n-1)kd\sin\theta}e^{-j(n-1)kd\sin\theta_s}\ , \tag{1}$$

where $d=$ element spacing, $\theta_s=$ steering angle, $k=2\pi/$ wavelength, and $\theta=$ angle off boresight.

If all phase shifters receive their steering phase simultaneously, then the beam jumps from one steering angle, θ_s^A, to another, θ_s^B. If the phase shifters receive commands from a serial data connection, then the antenna elements receive their phase shifts one at a time. Consequently, the main beam does not jump from one direction to another, but morphs from a main beam pointing at θ_s^A to a main beam pointing at θ_s^B.

Serial phase shift commands go first to element 1, then element 2, then …, finally to element *N*. Serial commands split the array factor into two contiguous parts with the left *n* elements receiving a linear phase shift that steers the beam to θ_s^A, and the right part of *N*-*n* elements having a main beam that points to θ_s^B. The array factor for a uniform array becomes a

Submitted On: April 23, 2015
Accepted On: May 26, 2015

superposition of the two parts of the linear array:

$$AF = \overbrace{1+\cdots e^{j(n-1)(\psi+\psi_A)}}^{A} + \underbrace{e^{jn(\psi+\psi_B)}+\cdots e^{j(N-1)(\psi+\psi_B)}}_{B} . \quad (2)$$

When all the phase shifters receive commands to point at θ_s^A, then only term *A* in (2) exists. Steering the beam to θ_s^B causes term *B* to emerge in (2). If the phase shifts are delivered to the elements starting with element 1 and going in sequence to element *N*, then the array factor is a superposition of an *n* element uniform array factor pointing at θ_s^A, and an $N-n$ uniform array factor pointing at θ_s^B the new steering direction. The examples that follow demonstrate the beam transition from θ_s^A to θ_s^B.

Assume a linear array has 20 isotropic point sources spaced $\lambda/2$ apart, and the elements receive phase shift commands sequentially from element 1 to element 20. The commands are separated by a time Δt_s. Figure 1 shows a plot of the array factor starting at broadside ($\theta_s^A = 0^o$ and $t = 0$) and ending when the beam reaches the desired steering angle at $\theta_s^B = 0.5^o$, ($t = 20\Delta t_s$). The main beam at broadside slowly steers to $\theta_s^B = 0.5^o$, so serial beam steering seems to work well for small beam steering increments (about a quarter of a 3 dB beamwidth or less).

Figure 2 shows a plot of the array factor starting at broadside ($\theta_s^A = 0^o$ and $t = 0$) and ending when the beam reaches the desired steering angle at $\theta_s^B = 45^o$, ($t = 20\Delta t_s$). The main beam at broadside gradually degrades, while the main beam at $\theta_s^B = 45^o$ gradually emerges. Beam steering with parallel commands skips the distorted array factors for $\Delta t_s \le t \le 19\Delta t_s$.

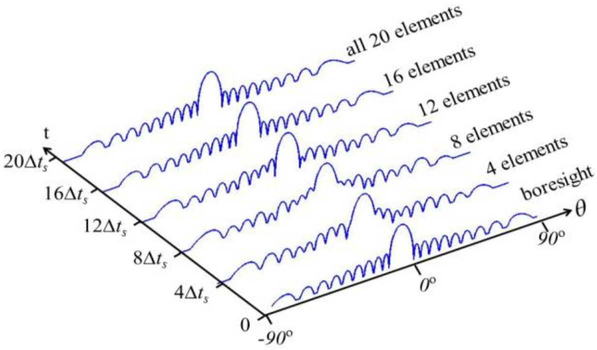

Fig. 1. Array factors as a function of time when steering a 20 element uniform linear array from boresight to 0.5^o.

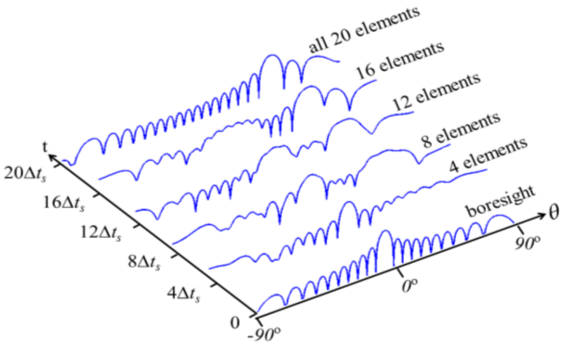

Fig. 2. Array factors as a function of time when steering a 20 element uniform linear array from boresight to 45^o.

The effects of serial steering on the array factor depend upon how far the beam is steered. The 20 element uniform array has a 3 dB beamwidth of 5.1^o and a null-to-null beamwidth of 11.4^o. Steering from $\theta_s^A = 0$ to $\theta_s^B = 3^o$ keeps the peak of the main beam near the 3 dB beamwidth of the broadside beam. Figure 3 (a) is a plot of the array factor after each phase shifter receives its steering command. At first, the broadside beam starts moving in the negative θ direction, while the new main beam begins to emerge at about $t = 8\Delta t_s$. The broadside main beam and the emerging main beam steered at $\theta_s^B = 3^o$ eventually merge into one beam at $t = 20\Delta t_s$. Figure 3 (b) is a plot of the maximum directivity, and its location in θ as the beam steers from broadside to $\theta_s^B = 3^o$. This plot confirms that the main beam starts moving in the negative θ direction before moving to $\theta_s^B = 3^o$. Along the way, the peak directivity decreases by 3 dB.

Increasing the beam steering to $\theta_s^B = 5.7^o$ puts the steered beam at the peak of the first sidelobe of the broadside pattern. Figure 4 (a) is a plot of the array factor after each phase shifter receives its steering command. The directivity of the broadside main beam decreases until it becomes the first sidelobe of the main beam steered at $\theta_s^B = 5.7^o$, while the first sidelobe of the broadside beam becomes the main beam at $\theta_s^B = 5.7^o$. Figure 4 (b) is a plot of the maximum directivity and its location in θ as the beam steers from broadside to $\theta_s^B = 5.7^o$. The maximum directivity shifts from $\theta = 0^o$ to $\theta = -1.2^o$ at the same time the directivity decreases over 3 dB. At the half way point, the peak gain dramatically shifts from $\theta = -1.2^o$ to $\theta = 7.3^o$. It then slowly gains directivity as it moves to the desired steering angle at $\theta_s^B = 5.7^o$.

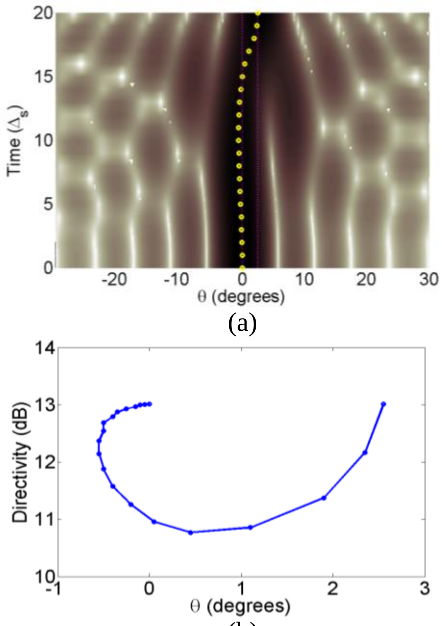

(a)

(b)

Fig. 3. Array factor as a function of time for a 20 element uniform linear array when serially steering from $\theta_s^A = 0^o$ to $\theta_s^B = 2.5^o$. (a) Circles indicate the main beam peak. (b) Location of maximum directivity.

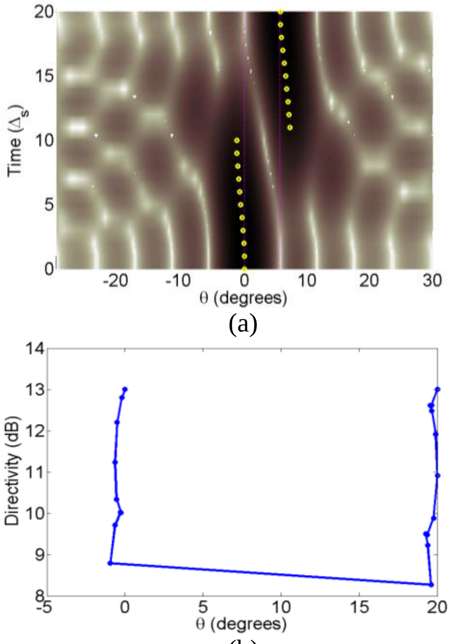

(a)

(b)

Fig. 4. Array factor as a function of time for a 20 element uniform linear array when serially steering from $\theta_s^A = 0^o$ to $\theta_s^B = 5.7^o$. (a) Circles indicate the main beam peak. (b) Location of maximum directivity.

As with the linear array, the main beam directivity of a 16×16 uniform planar array decreases while the main beam peak wanders in space when steering from one location to another. Figure 5 (a) shows the location of the main beam peak as it is serially scanned from $(\theta_s^A,\phi_s^A)=(0^o,0^o)$ to $(\theta_s^B,\phi_s^B)=(5^o,45^o)$. As with the linear array, the peak does not travel in a straight line from the initial angle to the desired steering angle. Instead, it wiggles about $\phi = 45^o$ as it goes from $(\theta_s^A,\phi_s^A)=(0^o,0^o)$ to $(\theta_s^B,\phi_s^B)=(5^o,45^o)$. The corresponding change in the peak directivity is shown in Fig. 5 (b). The main beam loses over 1 dB along its steering path.

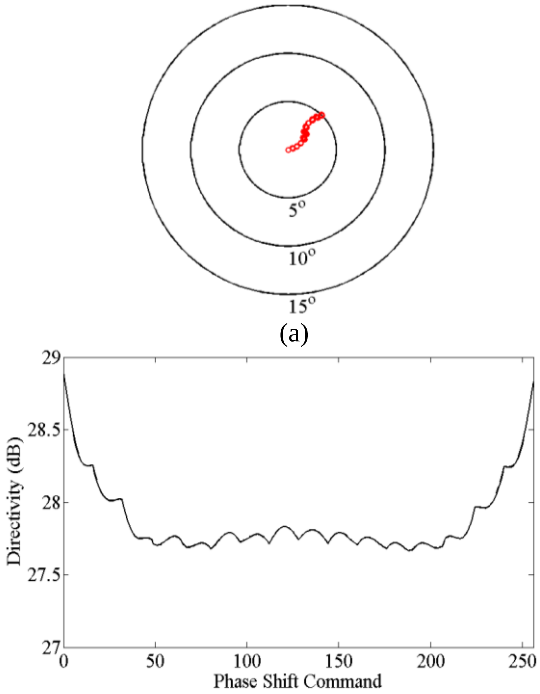

(a)

(b)

Fig. 5. Array factor as a function of time for a 16×16 element uniform planar array when serially steering from $(\theta_s^A,\phi_s^A)=(0^o,0^o)$ to $(\theta_s^A,\phi_s^A)=(5^o,45^o)$. (a) Circles indicate the main beam peak. (b) Location of maximum directivity.

III. NONSEQUENTIAL SERIAL PHASE SHIFTING

Sending the commands one phase shifter at a time in sequence from element 1 to element *N* has some undesirable consequences, such as the main beam peak moving to angles other than the starting and ending pointing directions. This section explores sending the phase shift commands to elements nonsequentially in order to prevent main beam wandering.

It is possible to reduce the main beam wandering due to serial phase shifting by not sending the phase shift commands to the elements in a random order. A random order for sending the phase shift commands was found by minimizing the maximum main beam deviation using a genetic algorithm from either θ_s^A or θ_s^B over 5^o increments of the scan range: 16, 19, 4, 14, 8, 11, 5, 17, 9, 3, 12, 6, 18, 15, 1, 2, 13, 10, 7, 20. Figure 6 compares sequential and nonsequential beam steering for $\theta_s^A = 0^o$ to $\theta_s^B = 2.5^o$. The nonsequential path for the main beam does not go below 0^o or above 2.5^o at any time. Sequential steering, on the other hand, steers the peak of the main beam below -0.5^o. The tradeoff with nonsequential steering is that the maximum decrease in the directivity is an additional 1 dB.

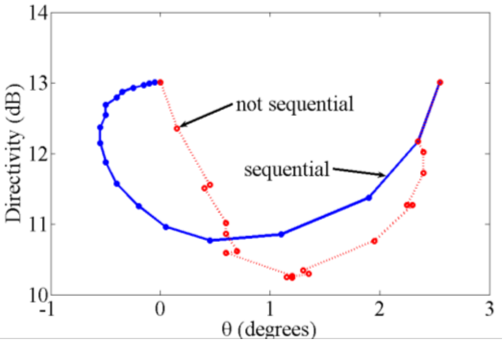

Fig. 6. Location of main beam peak vs. angle as a function of time as the main beam scans from $\theta_s^A = 0^o$ to $\theta_s^B = 2.5^o$.

IV. CONCLUSIONS

The main beam of a phased array can be scanned by sending the phase shifts to all the phase shifters, then changing their phase simultaneously, or by sending the phase shifts one at a time and changing the phase whenever the phase shifter receives the command. The simultaneous phase shift quickly moves a beam from one location to another. A serial phase shift, however, results in the main beam traveling a path from its present position to its desired new position with accompanying sidelobe level distortions. Serial commands can be sent to phase shifters and buffered (if there is available memory) until a strobe signals causes all the phase shifters to change at once, much like parallel phase shifting but slower. The beam wandering resulting from sequential serial phase shifting for beam steering greater than a fraction of a beamwidth can be limited by sending the phase steering commands in a random or optimal nonsequential order. There is a greater loss in directivity, though.

REFERENCES

[1] H. T. Friis, C. B. Feldman, and W. M. Sharpless, “The determination of the direction of arrival of short radio waves,” *Proceedings of the Institute of Radio Engineers*, vol. 22, pp. 47-78, 1934.

[2] R. L. Haupt, *Antenna Arrays: A Computational Approach*, Hoboken, NJ: Wiley-IEEE Press, 2010.

[3] R. Haupt, B. Thrall, A. Lyons, M. B. Davis, and R. Fitzgerald, “Phased array scanning with sequential commands,” *IEEE AP-S Symposium*, Chicago, IL, 1-2, 2012.

Merging VSim's Model Building and Visualization Tools with Custom FDTD Engines

R. Smith [1], A. Weiss [1], R. Bollimuntha [1], S. DMello [1], M. Piket-May [1], M. Hadi [1,2,3], and A. Elsherbeni [3]

[1] Department of Electrical, Computer, and
Energy Engineering
University of Colorado, Boulder, CO 80309, USA
ryan.smith-1@colorado.edu, alec.weiss@colorado.edu,
ravi.bollimuntha@colorado.edu,
sanjay.DMello@colorado.edu,
melinda.piket-may@colorado.edu

[2] Department of Electrical Engineering
Kuwait University, Safat 13060, Kuwait
mohammed.hadi@ku.edu.kw

[3] Department of Electrical Engineering & Computer Science
Colorado School of Mines, Golden, CO 80401, USA
aelsherb@mines.edu

Abstract **─** This work demonstrates how the graphical user interface of VSim (electromagnetic simulation software package) is modified and utilized to run a custom finite difference time domain algorithm. Commercial programs typically offer conventional FDTD functionality. More often than not, researchers may want to use their own code versions with proprietary modelling tools and extensions; for example, high-order differencing or specialized absorbing boundary conditions. VSim offers the flexibility of integrating an independent FDTD solver-engine that is tailored for the end user's needs. A detailed example is presented here of the replacement of VSim's own FDTD engine with a high-order FDTD code written with CUDA Fortran. Other custom FDTD codes could be integrated using the presented procedure.

Index Terms **─** CUDA Fortran, FDTD, High Order FDTD methods, VSim.

I. INTRODUCTION

The objective of this paper is to serve as a tutorial for using the graphical user interface (GUI) of VSim [1,2] as input/output interface, initially to define problem parameters and later to visualize the simulation results, while utilizing a custom-made FDTD algorithm. The custom FDTD algorithm used here is the high order FV24 algorithm [3,4], which has an extended unit cell reach that requires modifying some of the standard FDTD simulation parameters. The main constituents of VSim are the *VSimComposer* and *VSim Engine (Vorpal)*. *VSimComposer* is the GUI that allows users, via its Setup page, to define inputs and parameters such as problem space size, material properties and sources.

The *VSimComposer* or *VorpalComposer* also provides Run, Analyze and Visualize functionality. The available options on *VSimComposer* are shown in Fig. 1. Once the structure and behaviour of a simulation model is set using the Setup page, we start the simulation using the Run page. This starts the VSim's own EM computation engine, *Vorpal*, which is based on conventional FDTD. After the simulation is complete, the results, designated electric and magnetic fields, are placed in HDF5 (*.h5*) file format [5] that can be readily visualized using the Visualize page [6]. The main objectives of this work are to show how the same available interface of *VSimComposer* is used to initially set the problem space, import a CAD *.stl* file [6,7], then simulate the problem space by hooking a custom FDTD code to *Vorpal*, so that this custom scheme is run instead of VSim's FDTD engine, and finally to convert the output files to the appropriate (HDF5) format to enable VSim to understand the data to enable visualization. VSim offers the flexibility of integrating an independent FDTD solver-engine that is tailored for the end user's needs by using Python [1,2,8] scripts.

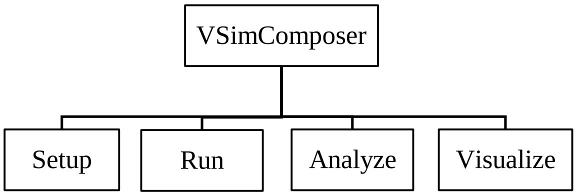

Fig. 1. Available page options on *VSimComposer*.

II. THE SIMLATION INPUT FILE

The input file to any VSim simulation is created with the *.pre* extension [6,9]. An already existing *pre* file can be customized according to the problem. We modify the simulation input parameters such as problem size,

Submitted On: June 3, 2015
Accepted On: January 24, 2016

material properties, scatterers, source location and frequency, etc. These appear in the form of table on Setup page and are collectively called *exposed variables*. We can also view the entire *pre* file and edit from the Setup page as text (using the View Input File button) or it can be modified in any text editor. Scatterers in the form of primitive shapes (rectangular prism, sphere, box, …etc.) or additional wave sources can be included in the problem space by defining their location, sizes, material and frequency (for sources). Scatterers of complex shapes are either formed by combining the primitive shapes or can be imported from a CAD file in binary *.stl* (STL: Stereo Lithography) format [6,9]. Some key variables that are defined in the *pre* file are described in Table 1.

Table 1: Description of key variables defined in *pre* file

Variable Name	Description
Primary_Frequency	The frequency of the source. Any harmonics are defined with respect to this frequency.
X_cells, Y_cells, Z_cells	No. of cells in each direction define the size of the problem.
Cells_ Per_ Wavelength	This gives the resolution of the grid: no. of cells that fit in one wavelength that is calculated from primary frequency.
Timesteps	How long the simulation will run, which also determines how far the wave will propagate.
Dump_Period	How often intermediate results of the simulation will be saved for visualization.
CAD_FILE_NAME	Name of the CAD file example.*stl*)
CAD_MATERIAL	Permittivity of material of scatterers in CAD file (0 for metal, ≥1 for dielectrics)
STRUCTURE_X,Y,Z	Location in the grid where the scatterer in CAD file needs to be placed.

A. Calculations of simulation parameters

Once the *pre* file is constructed as desired, it is validated (button in the upper right hand corner on Setup page) to check the *pre* file for errors. The output window at the bottom gives information about any syntax errors the verifier finds. While the *pre* file is being validated and saved, VSim performs some calculations so that the *.h5* files, placeholders for simulation data, are properly set up to hold all the required EM data.

A few key calculations are given below. The length of a cell is given by:

$$h = \Delta x = \Delta y = \Delta z \ = \lambda/R, \tag{1}$$

where R is cells per wavelength and,

$$\lambda = c/f, \tag{2}$$

where f is the frequency of the source and c is the speed of light in free space. The extent in a direction is thus,

$$L_{x,y,z} \ = hN_{x,y,z}, \tag{3}$$

where $N_{x,y,z}$ is the no. of cells in the x, y or z direction. And the time step is given by:

$$dt \ = (TIMESTEP\_FACTOR)\ h/(\,c\,\sqrt{3}), \tag{4}$$

where *TIMESTEP_FACTOR* is the Courant number.

Various steps involved in the implementation and the *VSimComposer* page they are started from and are given in the form of a flow diagram in Fig. 2.

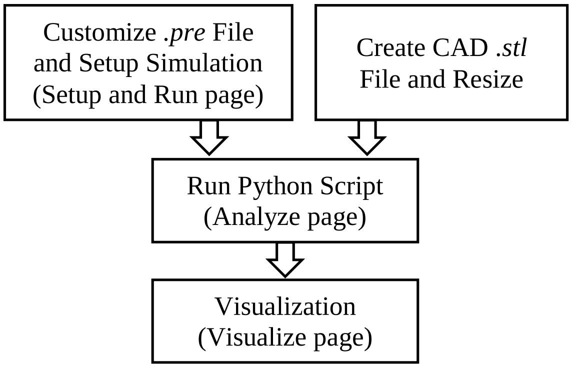

Fig. 2. Various steps involved in the implementation.

III. IMPORTING A CAD FILE

A CAD file is imported by initializing a variable in *pre* file with its name. As of *VorpalComposer 6.0* version, the only types of CAD files available to be imported are *.stl* files [7]. These files are a common format that many CAD programs can export to. If the file is not in this format, currently they are being converted by importing them into a CAD program and then exporting them as a binary *.stl* file. Generally, the *.stl* file has no representation of unit of measure, so the exporting units are arbitrary and need not be changed.

Since *.stl* file does not specify what units its distances are in, it needs to be resized according to the size of the problem space defined in the *pre* file, so that it fits inside the problem space. This task is accomplished by a separate C program (will be posted on ACES website). Currently this program simply scales the files to make each dimension less than a desired size and places the resized file in the working directory.

It is then possible to use the following macro in *pre* file to import shapes from a resized *.stl* file directly:

fillGeoCad(objectName, example_resized.stl,SHAPE_COMPLEMENT,SHAPE_SCALE,SHAPE_TRANSLATION)

By setting *SHAPE_COMPLEMENT* to zero the complement of the shape will not be taken. The *SHAPE_SCALE* is used to scale the resized CAD file shape into meters, the default units for length in *VorpalComposer* [6] for visualization purposes. The *SHAPE_TRANSLATION* can then be used to translate the *.stl* file relative to the location of the origin.

IV. SETTING UP THE SIMULATION

Once the *pre* file is customized as desired, the vorpal engine can be run using Run page on VSimComposer. This accomplishes two tasks: First, it creates empty *.h5* files. The *pre* file is modified such that no actual computations occur here; rather the empty *.h5* files are created to serve as placeholders for EM data (to be computed by the custom FV24 engine in the next step). This implies that the EM value for each cell at each dump time is temporarily 0. This is accomplished by using *dummyUpdater* in the *FieldUpdater* block in the *pre* file [9].

Second, it converts the resized *.stl* file to *.h5* file. The *pre* file is also modified to capture any resized *.stl* file placed in the working directory. It gets converted to *.h5* file that contains tables of information about the scatterer used for VSim's visualization. One of the tables contains the coordinates of the locations the scatterer occupies in the grid. This table is later picked and converted to .txt file to be used by the custom FDTD engine.

V. RUNNING THE SIMULATION

Now that the simulation has been set up, the custom FDTD engine, is called next. This is done using the Analyze page and selecting the Python script copied earlier to the working directory. This script can also be run from the command prompt after navigating to the working directory. The following subsections give a description of what this script does.

A. Parse the *pre* file

This is a string search that finds the names of variables and grabs their values. They are saved as python variables.

B. Convert scatterer *.h5* file into text file

Converts one of the tables in the scatterer *.h5* file generated earlier into a *.txt* file. This text file contains the coordinates of the scatterer elements in the grid. Material properties of the scatterer specified in the *pre* file are also added to the text file in the conversion process. This text file is later used by the custom FDTD engine.

C. Construct object arrays

An array of integers is constructed for each primitive object and additional source defined in *pre* file. This array identifies whether the object is sphere, box, etc. or a source and contains information on location and size.

D. Make a call to the custom FDTD engine

The compiled and ready-to-run custom FDTD engine is called and also, the parameters grabbed from the *pre* file and object arrays are passed to the custom FDTD engine. This engine should also pick the text file containing scatterer and material data. For our example, the results of the execution are saved in *.csv* (comma separated values) files as *Dump_1E.csv* (for electric field), *Dump_2E.csv*, etc. based on the dump period specified in *pre* file. There will be one electric field file and one magnetic field file for each data dump.

E. Conversion from *.csv* to *.h5* data format

Another python script is called that takes the data in the *.csv* files generated by custom code, and populates the *.h5* placeholders that were created by Vorpal engine earlier in the working directory.

VI. DATA VISUALIZATION

The EM data calculated by the custom FDTD engine are now present in the *.h5* files in the working directory, and can be viewed using the Visualize page of *VSimComposer*. VSim automatically detects the *.h5* files. Here is a list of important features in the 3D visualizer: "Display Contours" box in the lower left corner needs to be checked to see the wave nature of fields. On the left side, there are drop-down menus for Scalar and Vector data, as well as geometric objects. In the Scalar tab, the x, y, z component or the magnitude of either the electric or magnetic field can be selected. In the vector field tab, the electric or magnetic vector field can be selected. In the Geometries section, the user can check the primitive objects and imported CAD model to view them.

Once the data loads, the 3D visualizer can be used to pan and zoom around the waves. The time step bar at the bottom of the window is used to move in time. The number of contours shown can be changed between 2 and 20; this can be used to display every variation in the field, or only the major ones. Using the Colors button, the color scale of the visualizer can be changed. By default, the scale will update for each time step. If one wishes to keep the scale set for all time steps, the minimum and maximum values in the color options dialog may be fixed. This is useful for observing how the field strength decreases over time. A 3D view of electric field magnitude and the scatterer is shown in Fig. 3. In addition to 3D visualization, 2D cuts can be made to observe waves in 2D space using the Data View menu. A 2D view of electric field and the scatterer is shown in Fig. 4.

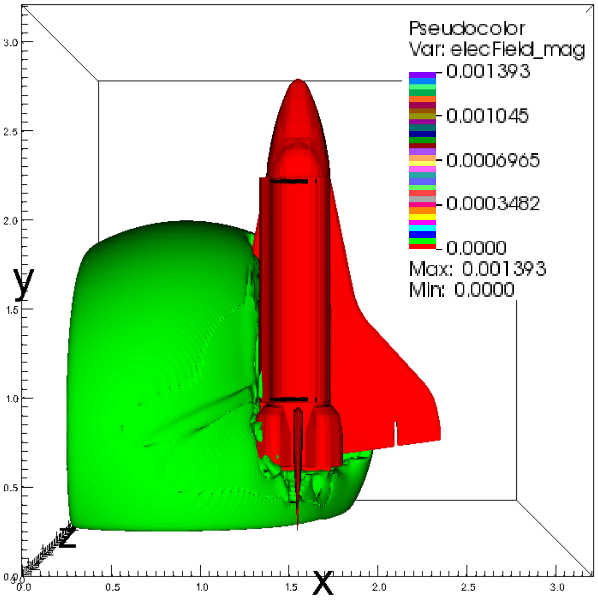

Fig. 3. A 3D view of electric field magnitude and shuttle scatterer at t = 180 time steps.

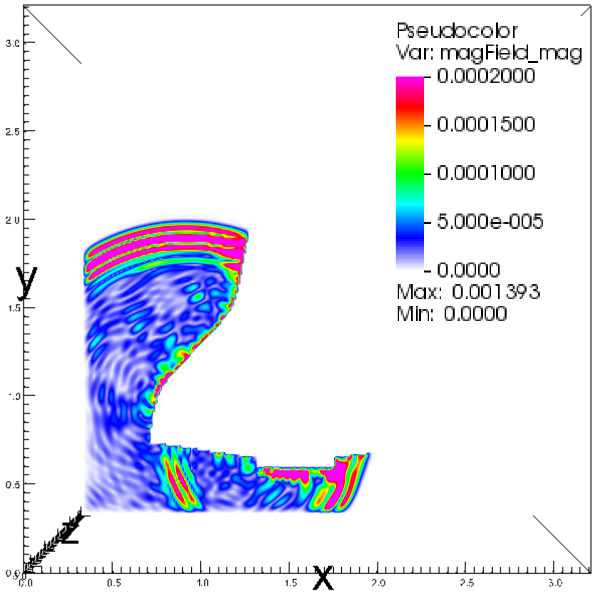

Fig. 4. A 2D slice in XY plane showing magnetic field magnitude at t = 180 time steps.

VII. SUMMARY AND CONCLUSION

A step-by-step implementation of a custom FDTD engine using the GUI data input and data visualization modules of a commercial EM simulation package is presented. Problem space defining parameters are set using the data input tool. Embedded scatterer definitions, if simple enough, could be defined by the same tool, or imported as a CAD file. The CAD file is then reshaped and combined with the user provided custom FDTD engine using a Python script. The visualization tool of the software package is finally used to observe and analyze collected simulation data. Although a custom high order FDTD engine was used as an example here, readers are at liberty to use their own FDTD engines written in their programming language of choice. A key data reshaping software tool will be posted to ACES website to facilitate this process.

ACKNOWLEDGEMENT

The authors would like to thank Tech-X Corp. for providing the license and support for the commercial software used for this work: VSim-7.0.0.

REFERENCES

[1] *VSim and VSim for Electromagnetics*, [Online]. Available: http://www.txcorp.com

[2] M. Piket-May, S. DMello, R. Smith and M. Hadi, “Using the VSim GUI to visualize high-order FV24 simulations of electrically large systems,” *IEEE Antennas Propagat. Society Int. Symp. (APSURSI)*, Memphis, TN, pp. 1632-1633, July 2014.

[3] M. F. Hadi, “A finite volumes-based 3-D low dispersion FDTD algorithm,” *IEEE Trans. Antennas Propagat.*, vol. 55, no. 8, pp. 2287-2293, Aug. 2007.

[4] M. F. Hadi, “CUDA Fortran acceleration for the finite-difference time-domain method,” *CPC*, vol. 184, no. 5, pp. 1395-1400, Jan. 2013.

[5] *What is HDF5?*, [Online]. Available: https://www.hdfgroup. org/HDF5

[6] *VSim in Depth*, Release 7.0.0, Tech-X Corporation, Boulder, CO, July 2014.

[7] *The STL Library*, [Online]. Available: http://www.eng.nus.edu.sg/LCEL/RP/u21/wwwroot/stl_library.htm

[8] *Beginner’s Guide to Python*, [Online]. Available: https://wiki.python.org/moin/BeginnersGuide

[9] *VSim Reference Manual*, Release 7.0.0, Tech-X Corporation, Boulder, CO, July 2014.

Novel Microstrip Ultra-Wideband Bandpass Filter Using Radial-Stub-Loaded Structure

Xida Deng [1], **Kai Da Xu** [2*], **Zhigang Wang** [1], **and Bo Yan** [1]

[1] EHF Key Laboratory of Science
University of Electronic Science and Technology of China (UESTC), Chengdu, 611731, China

[2] Institute of Electromagnetics and Acoustics & Department of Electronic Science
Xiamen University, Xiamen 361005, China
[*]kaidaxu@xmu.edu.cn

Abstract **─** A novel planar ultra-wideband (UWB) bandpass filter (BPF) using radial-stub-loaded resonator is proposed, where the resonator consists of three radial stubs, one located in the middle and two symmetrically at both sides. This radial-stub-loaded structure situates the first four resonant modes in the UWB passband (3.1~10.6 GHz) and makes the fifth resonant mode far away from this passband. To enhance the coupling degree, two interdigital coupled feed lines are utilized in this UWB filter. Finally, a UWB BPF with wide upper-stopband and sharp upper rejection skirt has been realized and its design steps have been also presented. The measured and full-wave simulated results of the proposed filter are in good agreement.

Index Terms **─** Bandpass filter, microstrip, radial-stub-loaded, ultra-wideband.

I. INTRODUCTION

UWB devices and systems have received great attention from both the academic and industrial fields since the U.S. Federal Communications Committee (FCC) fixed the UWB frequency spectrum range of 3.1 to 10.6 GHz for commercial use in 2002 [1]. As one of the key devices in a UWB system, UWB BPFs with low loss, compact size, and good selectivity attract the interest of the scholars and the industry. Many efforts have been carried out to make UWB BPFs better performance, e.g., the multiple-mode resonator (MMR) filters. A MMR with step-impedance structure was first presented to construct a UWB filter in [2]. However, this filter has a large size and its selectivity is also not very good. Then, three open-circuited stubs and three pairs of ones were employed to design MMR BPFs in [3] and [4], respectively, which produce four resonant modes in the passband. To improve the response and the rejection skirt of high frequency stopband, a novel UWB filter with three pairs of the rectangle stubs was introduced in [5]. Moreover, two types of quint-mode UWB filters were proposed to improve the in-band performance in [6] and [7]. The former one is using short-circuited shunt stub-embedded multiple-mode resonators, while the latter is based on dual stepped-impedance stub-loaded resonators without metalized via holes in the ground plane. In [8], the proposed multiple mode filter with a novel modified trisection stepped impedance resonator (SIR) is constructed to improve both in-band and out-band performance.

In this paper, a new UWB bandpass filter using triple-radial-stub loaded structure with interdigital coupling lines has been proposed. These triple radial stubs can not only situate the first four resonant modes in the passband but also move the fifth resonant mode up to the high frequency. To control the resonant modes of this structure within the FCC-regulated UWB passband, only a few variables need to be adjusted. Moreover, the proposed filter possesses an improved rejection skirt with a wider upper stopband compared with the References [2-8].

II. UWB BPF DESIGN

The structure of the proposed radial-stub-loaded UWB BPF on the printed circuit board (PCB) is shown in Fig. 1 (a). Figure 1 (b) is the equivalent network diagram of Fig. 1 (a). Three radial stubs are loaded in the middle of the resonator and the characteristic impedances of the filter input and output ports are both taken as 50 Ohm. The interdigital coupling lines can be seen as J-inverters, and their lengths are all around $\lambda g/4$, where λg is the guided wavelength at the center frequency of the UWB filter.

The parameters l_2, w_1 and s_1 in Fig. 1 (a) can affect the coupling strength between the resonator and feed lines, while the variation of the resonant modes can be observed and analyzed easily in the case of weak coupling. The simulated S_{21}-Magnitude results of the proposed radial-stub-loaded UWB filter under weak (l_2 = 0.5 mm, w_1 = 0.1 mm, s_1 = 0.1 mm) and strong

Submitted On: June 11, 2015
Accepted On: December 13, 2015

(l_2 = 7 mm, w_1 = 0.1 mm, s_1 = 0.1 mm) coupling are illustrated in Fig. 2 (a) and Fig. 2 (b), respectively, where Taconic RF-35 is used as the substrate of this filter with the relative dielectric constant of ε_r = 3.5 and thickness of 0.508 mm. As depicted in Fig. 2 (a), the in-band resonant modes of UWB (3.1-10.6 GHz) filter increase from two to four modes as the number of the radial stubs goes up; meanwhile, the harmonic responses are moved to higher frequency to make upper stopband wider. Furthermore, the rejection skirt of the filter is sharpened as the number of radial-stubs rises as shown in Fig. 2 (b). We can also see that the S_{21}-Magnitude curve in the UWB passband gradually rises towards the 0 dB line as the coupling strength increases. In the strong coupling case with l_2 = 7 mm, a desired UWB passband is realized. Compared with the filter using three rectangle stubs in [3], this structure using triple radial stubs achieves better performance.

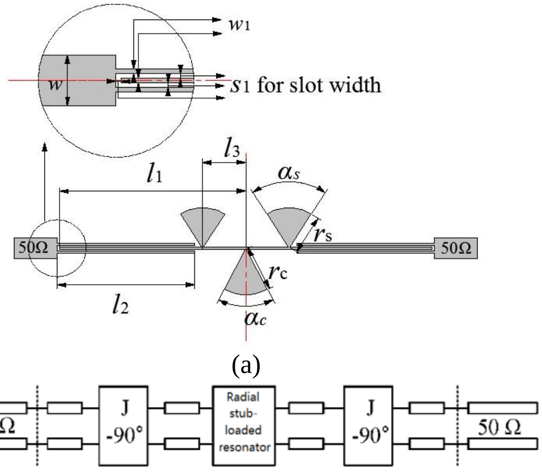

(a)

(b)

Fig. 1. (a) Schematic diagram of the proposed radial-stub-loaded UWB BPF (the structure is symmetrical with the red dash lines), and (b) its equivalent network diagram.

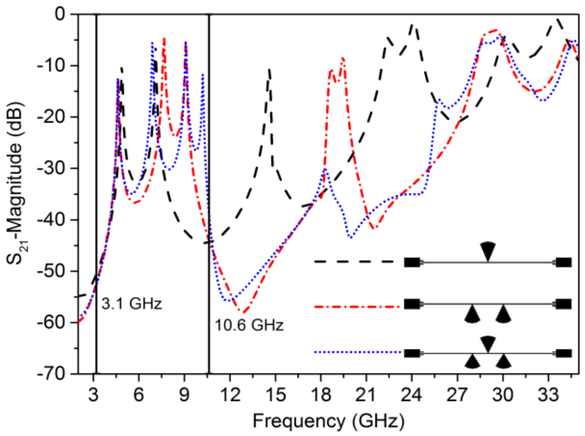

(a)

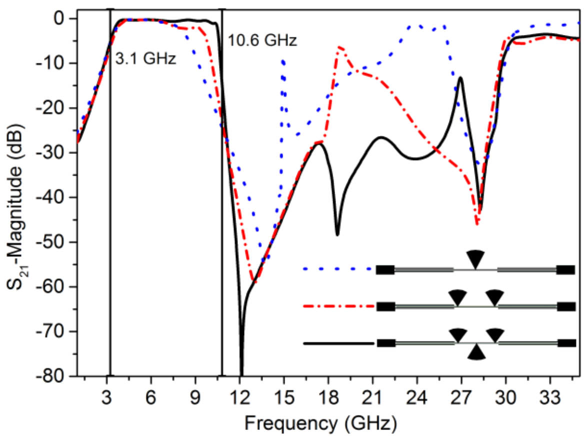

(b)

Fig. 2. Simulated S_{21}-magnitude comparisons of the filter: (a) when using single, dual and triple radial-stubs under weak coupling with l_2 = 0.5 mm, w_1 = 0.1 mm, s_1 = 0.1 mm, and (b) when using single, dual and triple radial-stubs under strong coupling with l_2 = 7 mm, w_1 = 0.1 mm, s_1 = 0.1 mm, where the other dimensions are fixed as l_1 = 9.5 mm, l_3 = 2.2 mm, w = 1.1 mm, r_c = 2.4 mm, r_s = 2.1 mm, $\alpha_c = 55^\circ$ and $\alpha_s = 65^\circ$.

Figure 3 illuminates the simulated frequency characteristics of the radial-stub-loaded resonator under weak coupling case of Fig. 1 (a) with varied r_s, α_s, and r_c, α_c respectively. We can see that the first four resonant frequencies, namely, f_{m1}, f_{m2}, f_{m3} and f_{m4} are located in the passband from 3.1 to 10.6 GHz, which can determine the passband frequency. Figure 3 (a) shows the relationship between parameters of two side radial stubs and the resonant frequencies. As r_s varied from 1.9 to 3.2 mm, f_{m3} and f_{m4} shift downwards but f_{m1} and f_{m2} almost remain unchanged although the angle of α_s changes from 50 to 80 degree, while f_{m5} stays around 18 GHz all the time. In Fig. 3 (b), f_{m1} and f_{m3} almost remain the same when r_c and α_c vary but f_{m4} decreases with the increase of r_c, while f_{m2} and f_{m4} increase with the decrease of α_c.

The aforementioned relationships assist us easily control the dimensions of the radial stub-loaded resonator to achieve the expected S_{21}-magnitude responses. Based on the above analysis, the design steps of the proposed filter are listed as follows. Firstly, we let l_2 equal to $\lambda g/4$. Secondly, l_3 will be chosen to meet the requirement of the lower cut-off frequency, and then make l_1 equal to around l_2+l_3. Thirdly, r_c, α_s, r_s, and α_c need to be adjusted to fit in the right side of the passband or the upper cut-off frequency. Finally, adjust w_1 and s_1 slightly to achieve the required coupling coefficient and meet the desired frequency selectivity.

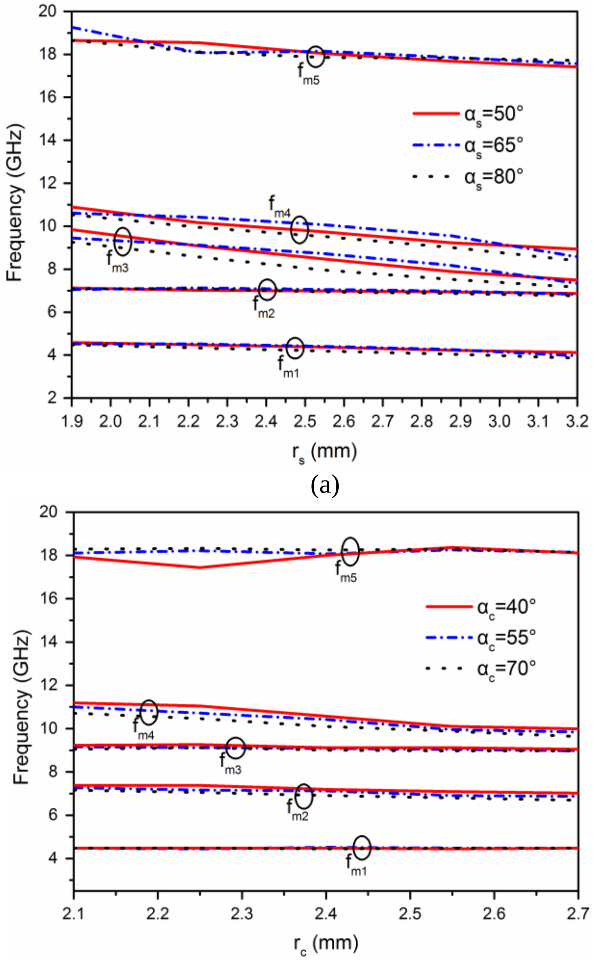

(a)

(b)

Fig. 3. Simulated characteristics of the proposed radial-stub loaded structure under weak coupling case with varied: (a) α_s and r_s, (b) α_c and r_c, where the other dimensions are fixed as l_1 = 9.5 mm, l_2 = 0.5 mm, l_3 = 2.2 mm, s_1 = 0.1 mm, $w = w_1$ = 1.1 mm.

III. FABRICATION AND MEASUREMENTS

Based on the above analysis, a novel adjustable UWB BPF using radial-stub-loaded structure is designed and fabricated on a Taconic RF-35 substrate with a relative permittivity of 3.5 and a thickness of 0.508 mm. The variables shown in Fig. 1 are chosen as follows: l_1 = 9.5 mm, l_2 = 7 mm, l_3 = 2.2 mm, s_1 = 0.1 mm, w_1 = 0.1 mm, w = 1.1 mm, r_c = 2.4 mm, $\alpha_c = 55^\circ$, r_s = 2.1 mm, $\alpha_s = 65^\circ$. The overall size of the filter still only amounts to 19.2 mm × 4.5 mm, though a low dielectric constant of this substrate has been used. The photograph of the fabricated microstrip radial-stub-loaded UWB BPF is shown in Fig. 4.

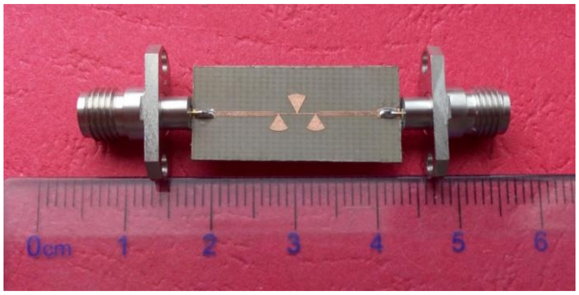

Fig. 4. Photograph of the fabricated microstrip UWB BPF.

The simulated and measured results are accomplished by using software HFSS [9] and vector network analyzer, respectively. As the SMA connectors in Fig. 4 is rated to 26.5 GHz, the frequency range of measurement is set from 1 to 26.5 GHz. Figure 5 show S-parameter and group delay results of the proposed filter, where the simulations and measurements are in good agreement. Slight deviation is observed between simulated and measured results, which could be attributed to unexpected tolerances in fabrication, material parameters and soldering. In the measurement, the 3-dB bandwidth is from 3.4 to 10.5 GHz. As shown in Figs. 5 (a) and (b), the insertion loss, including the losses from two SMA connectors, is less than 1.8 dB while the return loss is greater than 11.5 dB from 3.4 GHz to 10.5 GHz, which achieves a fractional bandwidth of 102%. The upper out-of-band rejection is greater than 23 dB from 11 to 26.5 GHz, which realizes a significant improvement compared with the References [2-8]. Moreover, the measured group delay is less than 0.8 ns in the UWB passband as depicted in Fig. 5 (c).

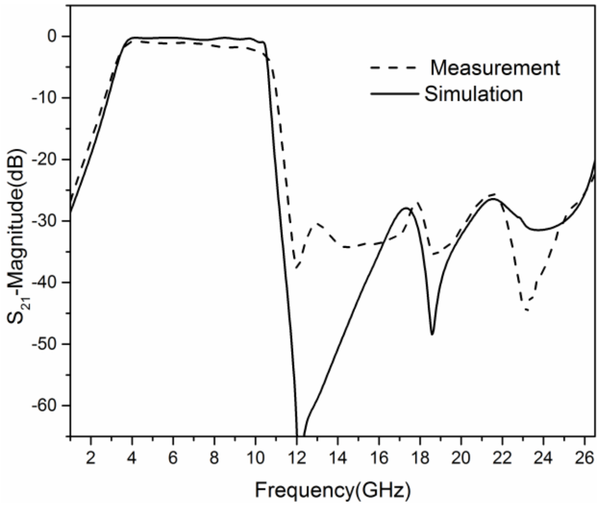

(a)

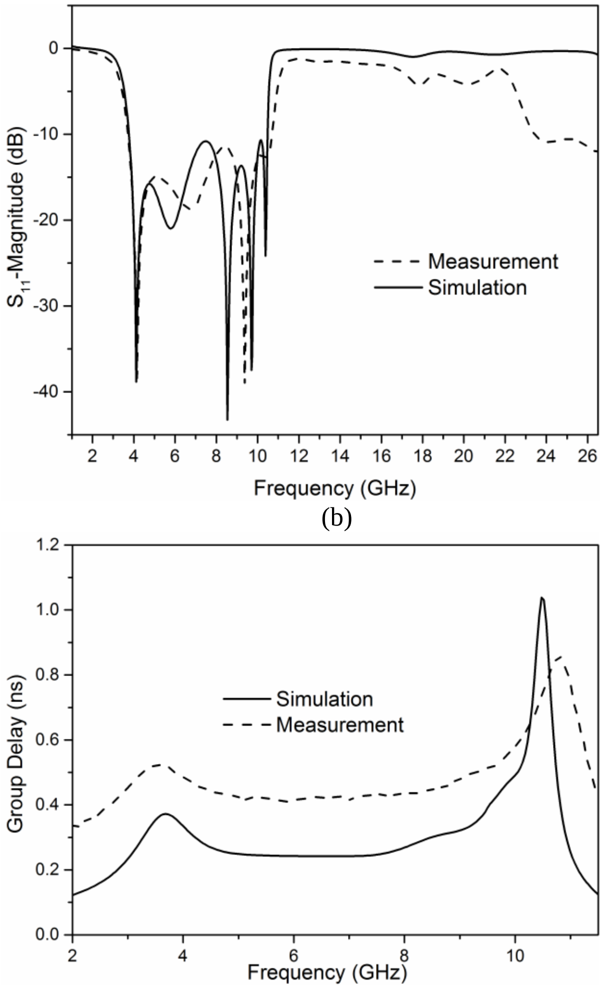

(b)

(c)

Fig. 5. Simulated and measured results of: (a) S_{21}, (b) S_{11}, and (c) group delay of the proposed UWB BPF.

IV. CONCLUSION

In this paper, a UWB BPF based on radial-stub-loaded resonator has been presented. Following the design procedure, we successfully allocate the first four resonant modes of the proposed BPF within the FCC-regulated UWB passband. Compared with UWB BPFs in [2-8], the proposed structure has better skirt selectivity and out-of-band rejection demonstrated both in simulation and measurement. The measured results validate the proposed design.

REFERENCES

[1] U. F. C. Commission, “FCC revision of part 15 of the commission's rules regarding ultra-wideband transmission systems: first report and order,” Technical Report, Feb. 2002.

[2] L. Zhu, S. Sun, and W. Menzel, “Ultra-wideband (UWB) bandpass filters using multiple-mode resonator,” *IEEE Microwave and Wireless Components Letters*, vol. 15, pp. 796-798, 2005.

[3] R. Li and L. Zhu, “Compact UWB bandpass filter using stub-loaded multiple-mode resonator,” *IEEE Microwave and Wireless Components Letters*, vol. 17, pp. 40-42, 2007.

[4] S. W. Wong and L. Zhu, “EBG-embedded multiple-mode resonator for UWB bandpass filter with improved upper-stopband performance,” *IEEE Microwave and Wireless Components Letters*, vol. 17, pp. 421-423, 2007.

[5] S. W. Wong and L. Zhu, “Implementation of compact UWB bandpass filter with a notch-band,” *IEEE Microwave and Wireless Components Letters*, vol. 18, pp. 10-12, 2008.

[6] S. W. Wong and L. Zhu, “UWB bandpass filters using short-circuited shunt stub-embedded multiple-mode resonators,” *Microwave and Optical Technology Letters*, vol. 51, pp. 2556-2559, 2009.

[7] S. Oh, B. Shin, J. Jeong, Y. S. Kim, and J. Lee, “UWB bandpass filter using dual stepped impedance stub loaded resonators,” *Microwave and Optical Technology Letters*, vol. 56, pp. 448-450, 2014.

[8] L. Y. Chen, C. H. Lee, and C. I. G. Hsu, “Novel UWB BPF design using modified trisection MMR,” *Microwave and Optical Technology Letters*, vol. 50, pp. 2904-2907, 2008.

[9] Ansoft High Frequency Structural Simulator (HFSS), 12th ed., Framingham, MA, USA, Ansoft Corp., 2006.

Slotted Triangular Monopole Antenna for UHF RFID Readers

Khaled ElMahgoub [1,2]

[1] Autoliv ASP, Inc.
1001 Pawtucket Blvd, Lowell, MA 01854, USA
[2] Auto-ID Labs, Massachusetts Institute of Technology
77 Massachusetts Avenue, Cambridge, MA 02139, USA
kelmahgoub@ieee.org

Abstract **─** A new compact slotted triangular monopole antenna for ultra-high frequency (UHF) radio frequency identification (RFID) applications is presented. The antenna exhibits an omnidirectional radiation pattern and has a bandwidth (BW) of more than 13%. It covers the global UHF RFID band and has a maximum gain of around 2.6 dBi. An overview of the antenna design along with the full wave simulation is provided. A prototype of the antenna is fabricated and tested. Good agreement is obtained between simulated and measured results. Moreover, the antenna is used with a UHF RFID reader in real use cases where read range and read rate with different commercial tags are used to evaluate the antenna performance.

Index Terms **─** Monopole antenna, Radio Frequency Identification (RFID), read range, read rate.

I. INTRODUCTION

These days' radio frequency identification (RFID) use cases have increased considerably. RFID is a technology which uses RF signals for automatic identification of objects. It is utilized for several applications as a part of different territories, for example, electronic toll gathering, retail administration, access frameworks and numerous others [1]. In spite of the fact that these applications are important around the world, diverse districts have distinctive administrative standards for ultra-high frequency (UHF) RFID frameworks. In China the UHF RFID bands are 840-845 MHz and 920-925 MHz, while for North America, Europe 902-928 MHz band, 865-868 MHz band are used respectively, while for Japan up till 2018 two bands can be used 916-924 MHz and 950-956 MHz. So for an UHF RFID item to work all inclusive it should be reconfigurable or has enough band to cover the whole UHF RFID band (840-960 MHz). This adds a challenge in designing a global UHF RFID antenna. Many broadband UHF RFID reader antennas have been proposed in literature [2]-[5].

In this paper, a new compact omnidirectional broadband antenna for UHF RFID is proposed. The antenna is based on a triangular monopole antenna structure with triangular slot [6]. It has an impedance matching (<10 dB) BW over 13% and covers the global UHF RFID band (840-860 MHz). The antenna has a maximum gain of 2.6 dBi, and a gain around 2.5 dBi over the entire band. The antenna is small (dimensions $< \lambda/3 \times \lambda/3$ at the center frequency of the band $f = 900$ MHz) and is suitable for small or handheld UHF RFID readers. The antenna was fabricated and different properties were measured, simulation and measured results showed good agreement. Moreover, the antenna was used with a commercial reader and real uses cases were tested.

The paper is organized as follows: In Section II, the antenna design is described, a parametric study is conducted to examine the effect of the slot dimensions and the final dimensions of the antenna are stated. In Section III, the antenna simulation and measurements results are provided. Conclusions are provided in Section IV.

II. ANTENNA DESIGN AND PARAMETRIC STUDY

In this section, the design process of the antenna is described. The final design is shown in Fig. 1 and the final dimensions are stated. First step of the design process is using an equilateral triangular monopole antenna for wide band operation [7]; the antenna perimeter is chosen to be equal $\lambda/2$ where λ is the wavelength at 900 MHz. A microstrip line is used for feeding, and the antenna is mounted over a Roger RT/droid 6006 substrate with $\varepsilon_r = 6.15$, $\tan\delta = 0.0019$, and thickness of 1.9 mm. Second step is adding a triangular slot to enhance the matching, and to study the effect of such slot a parametric study was conducted on the dimensions of the slot using high frequency structural simulator (HFSS) [8]. Two parameters are studied, first the slot gap size g, which is changed while other dimensions are kept fixed. As shown in Fig. 2 (a), it is clear that the gap size can be used to shift the

Submitted On: August 23, 2015
Accepted On: December 13, 2015

matching BW toward the required center frequency. Based on the parametric study g = 4.215 mm was chosen for this design. The second parameter is the slot width S_3, the slot width is changed while other dimensions are kept fixed. It could be noticed from Fig. 2 (b) that the slot width also causes a shift in the center frequency, S_3 = 60.415 mm was chosen. Moreover, genetic algorithm optimization was used to finalize the rest of the dimensions. The default parameters of HFSS genetic algorithm were used as follows: maximum number of generations is 1000, and number of individuals for parents, mating pool, children, next generation is set to 30, the number of survivors is set to 10, the goal was set that $|S_{11}|$(dB) at 900 MHz is ≤ -25 dB.

III. SIMULATION AND MEASUREMENTS RESULTS

In this section, the full wave simulations are carried out using HFSS. Moreover, measurement results are provided for the fabricated antenna shown in Fig. 1 (b). There is good agreement between the simulation and the measurement results.

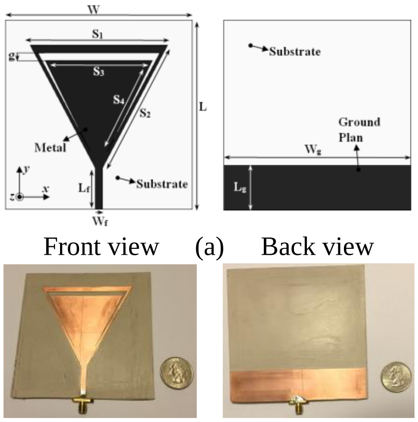

Front view (a) Back view

(b)

Fig. 1. (a) Antenna design, and (b) fabricated antenna (all dimensions in mm) [L = W = W_g = 105, S_1 = 77.275, S_2 = 77.553, S_3 = 60.415, S_4 = 56.55, L_f = 22.914, W_f = g = 4.215].

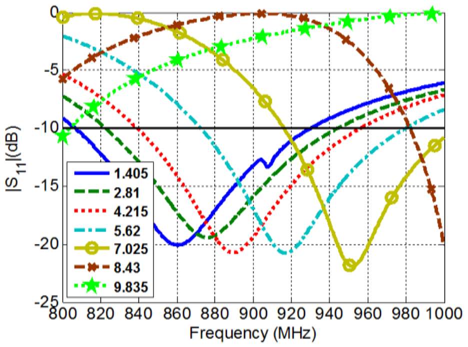

(a)

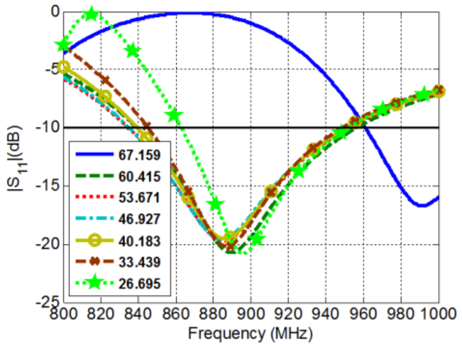

(b)

Fig. 2. Parametric study (units in mm): (a) g and (b) S_3.

A. Return loss

First the return loss is simulated and measured, and the results are shown in Fig. 3. As shown in the figure, the antenna is matched ($|S_{11}|$ < -10 dB) for the entire UHF RFID band (840 MHz to 960 MHz) with BW of more than 13%. Good agreement between simulated and measured results can be noticed.

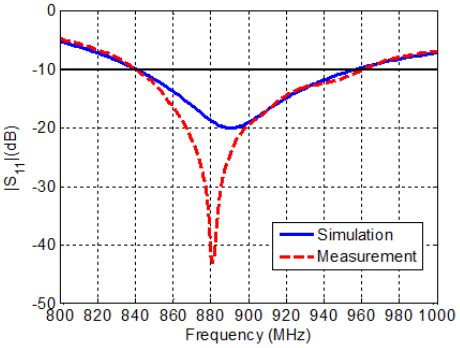

Fig. 3. Simulated and measured $|S_{11}|$ in dB.

B. Maximum gain

The maximum gain (at $\varphi = \theta = 0$) of the antenna is simulated and measured for different frequencies, the measurement setup is shown in Fig. 4 (a). The antenna has a gain around 2.5 dBi for the entire RFID UHF global band as shown in Fig. 5.

C. Radiation pattern

The radiation patterns of the antenna are simulated and measured at 915 MHz (center frequency for North America band). Measurement setup is shown in Fig. 4 (b), the radiation pattern are measured using what is defined in this paper as active measurement technique (measurement is done while reading a real tag). In this measurement technique the antenna is connected to M6e-M reader [9] (commercial UHF RFID) and the reader is set to the required frequency, the reader software is used to read a real tag (Alien Higgs 3 ALN-9640-Squiggle [10]) and report the tag received power.

The antenna is set at a fixed distance from the tag (1 meter) and the antenna is rotated using the 2 stepper motors as shown in the Fig. 4 (b). The received power at different angles is used to plot the measured radiation pattern (normalized to maximum received power). Figure 6 shows the different plane cuts for the radiation pattern, as shown the antenna exhibits an omnidirectional radiation pattern. Moreover, there is good agreement between the simulated and measurement results.

D. Read range

The Friis equation is used to calculate the theoretical maximum read range of an Alien Higgs 3 ALN-9640-Squiggle tag as follows:

$$r = \frac{\lambda}{4\pi}\sqrt{\frac{P_t G_t(\theta,\varphi) G_r(\theta,\varphi)\, p \left|T_{antenna}\right|^2 \left|T_{tag}\right|^2}{P_{th}}}\,, \qquad (1)$$

where, r is the read range in meters, λ is the wavelength in meters, P_t is the transmitted power by the reader in watts, G_t the gain of the transmitting antenna, G_r the gain of the receiving tag antenna, p the polarization efficiency, $T_{antenna}$ is the power transmission coefficient of the antenna (account for mismatch), T_{tag} is the power transmission coefficient of the tag and P_{th} is the minimum received power necessary to turn on the chip in watts. For maximum theoretical read range the following parameters are used: P_t is used as 1 W, which is the maximum allowed transmitted power in USA, p is used as 1 for polarization matching, P_{th} is used as -14 dBm (39.8107 µW) as provided by the chip vendor [11] for the measured equivalent circuit, λ is set for each frequency from 800 MHz to 1 GHz. As for the return loss and the transmitting maximum gain they are calculated from the HFSS simulation, the maximum gain (at $\varphi = \theta = 0$) is used for maximum read range. While the receiving gain is used as 2 dBi for small dipole and T_{tag} is assumed as 1 for matching case. The read range is around 7.5 meter on average, and it has a maximum value of 8 meter in the 840 MHz China band. Moreover, the read range was measured using the M6e-M reader and two commercial tags Alien Higgs 3 ALN-9640-Squiggle, and Monza 4 Frog 3D tag [12]. The measurement setup is shown in Fig. 4 (c), the reader is set to 5 different frequencies (866.3, 915.25, 918.5, 919.2 and 922.625 MHz) to cover most of the UHF RFID global band, and the reader power was set to 30 dBm. The theoretical result is compared with the measurement results in Fig. 7. As shown in Fig. 7, the measured read range for the ALN-9640-Squiggle tag is 6 meter for EU band and around 6.5 meter for USA band, which is less than the maximum theoretical read range, and this is due many factors such as the return loss of the tag in real case can't be neglected, also polarization mismatch factor should be added due to misalignment, in addition the tag antenna gain might be less the 2 dBi used in the theoretical read range calculation. Moreover, the read range of the Frog 3D tag is less than the ALN-9640-Squiggle due to polarization mismatch, the Frog 3D tag is dual polarized while the other tag is linear polarized which is in alignment with the proposed antenna polarization.

E. Read rate

The read rate is measured using two fabricated prototypes of the proposed antenna connected to the M6e-M reader as shown in Figs. 4 (d) and 4 (e). The universal reader assistant (URA) software [13] is used to read a large tag population of 230 GEN2 Tags with several chips and antennas. The default profile is used with the following configuration: region is set to USA with band 902 to 928 MHz with 50 hopping frequency, transmitted power of 30 dBm, two antenna ports 1 and 2, Miller 4 encoding, backscattered Link Frequency (BLF) of 250 kHz. As shown in Fig. 8, the reader reads 221 unique tags per second (tags/sec), while the reader reads 220 tags/sec when using two 6 dBi commercial antennas set underneath the table as shown in Fig. 4 (e). The result proves that the proposed antenna can be used in real life use cases.

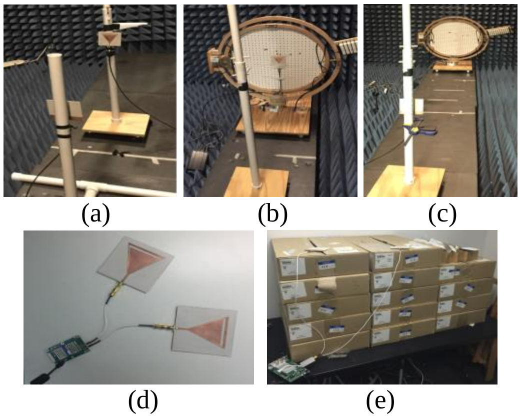
(a) (b) (c)
(d) (e)

Fig. 4. Measurement setup: (a) antenna gain, (b) radiation pattern, (c) read range, (d) commercial reader, and (e) read rate.

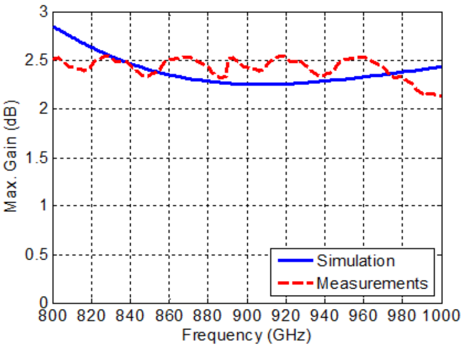

Fig. 5. Simulated and measured maximum gain versus frequency.

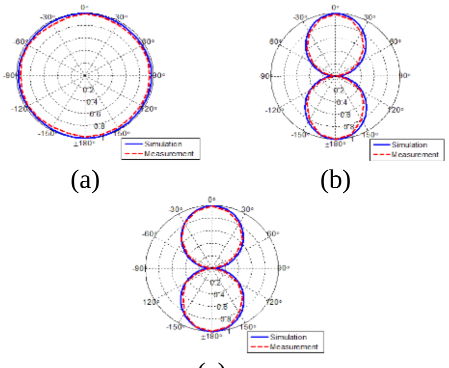

(a) (b)

(c)

Fig. 6. Simulated and measured radiation patterns normalized E_{total} at 915 MHz: (a) *x-z*, (b) *y-z*, and (c) *x-y* planes.

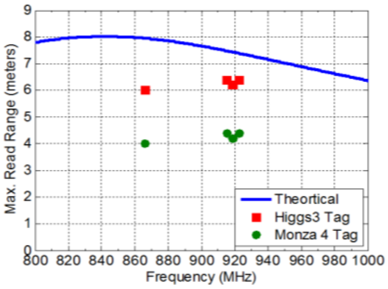

Fig. 7. Transmission coefficient for sandwiched composite-FSS structure under oblique incident TE^z plane wave (θ = 30º, φ = 60º).

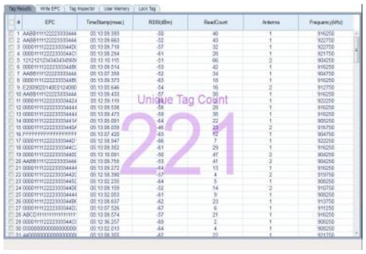

Fig. 8. Read rate measurements.

IV. CONCLUSION

A compact slotted triangular monopole antenna for universal UHF RFID applications is presented. The antenna exhibits an omnidirectional radiation pattern and has a bandwidth (BW) of more than 13%, and a maximum gain of around 2.6 dBi. The antenna design process was introduced and a prototype of the antenna was fabricated and measured. Good agreement is observed between the full wave simulation and measured results. Moreover, the antenna performance was evaluated with a UHF RFID reader in real use cases where read range and read rate with different commercial tags were measured. The antenna is suitable for small or handheld global UHF RFID readers.

REFERENCES

[1] K. ElMahgoub, T. Elsherbeni, F. Yang, A. Elsherbeni, L. Sydänheimo, and L. Ukkonen, "Logo–antenna based RFID tags for advertising applications," *ACES Journal, Special Issue on Computational and Experimental Techniques for RFID Systems and Applications*, part I, vol. 25, no. 3, pp. 174-181, Mar. 2010.

[2] J. Lu and S. Wang, "Planar broadband circularly polarized antenna with square slot for UHF RFID reader," *IEEE Transaction on Antennas and Propagation*, vol. 60, no. 1, pp. 45-53, Jan. 2013.

[3] Z. Wang, S. Fang, S. Fu, and S. Jia, "Single-fed broadband circularly polarized stacked patch antenna with horizontally meandered strip for universal UHF RFID applications," *IEEE Transaction on Microwave Theory and Techniques*, vol. 59, pp. 1066-1073, Apr. 2011.

[4] X. Liu, Y. Liu, and M. M. Tentzeris, "A novel circularly polarized antenna with coin-shaped patches and a ring-shaped strip for worldwide UHF RFID applications," *IEEE Antennas and Wireless Propagation Letters*, vol. 14, pp. 707-710, Dec. 2014.

[5] C.-C. Lin, L.-C. Kuo, H.-R. Chuang, and Y.-C. Kan, "A universal UHF RFID reader antenna," *IEEE Transaction on Microwave Theory and Techniques*, vol. 57, pp. 1275-1282, May 2009.

[6] K. ElMahgoub, "Omnidirectional triangular antenna for UHF RFID readers," *IEEE Antennas and Propagation Society International Symposium (APSURSI)*, pp. 1296-1297, Jul. 2014.

[7] C.-C. Lin, Y.-C. Kan, L.-C. Kuo, and H.-R. Chuang, "A planar triangular monopole antenna for UWB communication," *IEEE Microwave and Wireless Components Letters*, vol. 15, no. 10, pp. 624-626, Oct. 2005.

[8] HFSS: http://www.ansys.com/Products/Simulation+Technology/Electromagnetics/Signal+Integrity/ANSYS+HFSS

[9] ThingMagic M6e-Micro reader, http://www.thingmagic.com/embedded-rfid-readers/m6emicro/1-embedded-rfid-readers/394-m6emicro

[10] ALN-9640-Squiggle: http://www.alientechnology.com/wp-content/uploads/Alien-Technology-Higgs-3-ALN-9640-Squiggle.pdf.

[11] Higgs3 IC: http://www.alientechnology.com/wp-content/uploads/Alien-Technology-Higgs-3-ALC-360.pdf.

[12] https://www.smartrac-group.com/files/content/Products_Services/PDF/Frog3D_M4.pdf

[13] ThingMagic Universal Reader Assistant (URA), http://www.thingmagic.com/images/Downloads/software/URABonjourSetup64.zip

A Broadband Microstrip-to-Microstrip Vertical Via Interconnection for Low Temperature Co-Fired Ceramic Applications

Yupeng Liu, Lei Xia*, and Ruimin Xu

Fundamental Science on EHF Laboratory
University of Electronic Science and Technology of China, Chengdu, 611731, China
lypscottabcd@gmail.com, xialei@uestc.edu.cn*, rmxu@uestc.edu.cn

Abstract ─ This letter presents a microstrip-to-microstrip vertical via interconnect in microwave low temperature co-fired ceramic (LTCC) technology. According to the simulation results, the insertion loss is less than 0.33 dB and the return loss is greater than 29.9 dB from 0.3 GHz to 18 GHz. An equivalent lumped model is developed for analyzing the microstrip-to-microstrip vertical interconnection. The structure has been manufactured and measured.

Index Terms ─ Equivalent model, low temperature co-fired ceramic, microstrip-to-microstrip and vertical via interconnect, microwave.

I. INTRODUCTION

Low temperature co-fired ceramic (LTCC) is in the core place of multi-chip module (MCM) technology. With the excellent RF performance, the recent research shows that LTCC technology is more for use in microwave and millimeter-wave applications, the high-speed high-density, three-dimensional integration technology and so on, by its advantages, such as low thermal conductivity, high packaging flexibility, high integration density, high stability, and low cost [1-3]. It is widely applied in wireless communication systems [4]. Microwave components like stripline, cavity, substrate integrated waveguide (SIW) can be easily implemented on account of its three dimensional (3D) multi-layer structure [5]. LTCC multilayer circuit strctures require the interconnection of signals between different layers which will restrict the overall performance of the circuit systems. This is of key importance in the design of LTCC circuit systems. The high quality LTCC vertical interconnection plays an important role in system-in-package (SiP) module packaging applications. Since the geometry of vertical interconnections have significant effect in the electromagnetic behaviors of the LTCC multi-layer system [6], it becomes necessary to investigate the characteristics of these vertical interconnections.

The detailed design and implementation of the microstrip-to-microstrip vertical interconnection with better performance at microwave frequencies are considered in LTCC technology.

II. DESIGN DESCRIPTION

The configuration of microstrip-to-microstrip single vertical via interconnect is shown in Fig. 1 (a). The bottom microstrip line is vertically connected by coaxial-like signal via hole to microstrip line on top of the substrates. The inner ground planes on three different substrate layers are connected by the staggered via holes.

The proposed structure consists of eight layers of Ferro-A6M substrates with via holes formed by Ferro CN33-407 silver paste, internal conductors formed by Ferro CN33-398 silver paste, and external conductors formed by Ferro CN33-391 silver paste. Each substrate has a thickness of 94 μm with a relative permittivity of 5.9. So the total thickness of the design structure is 752 μm, and the thickness of the external conductors is 10 μm. According to the LTCC process specifications, two ceramic substrate layers are chosen for each microstrip line, which provides reasonable size for 50 Ω transmission lines. Both of the top and bottom microstrip lines are 310 μm conductor in width. The circular pad, connecting the microstrip line and transmission via hole, has a diameter of 320 μm. The height of signal via hole corresponds to the 8-layer LTCC substrate thickness. All via holes in the design are of 130 μm diameter.

In addition, the dominant mode of the microstrip line is quasi-TEM mode. This mode, relative to symmetry plane of the central microstrip line, is an even mode. Besides, the dominant mode of the coaxial-like line, formed by the vertical signal via and the surrounding shielded holes, is TEM mode. And this mode is also an even mode relative to symmetry plane of the central microstrip line. Therefore, it can realize a transition from the quasi-TEM wave of the microstrip line to TEM wave of the coaxial-like line among the interconnection structure. Figure 1 (b) illustrates 3D view of the coaxial-like via structure. As is known to all, the discontinuity effect of the vertical via hole can result in non-negligible signal reflection, which may seriously degrade the performance. Therefore, the effect of characteristic

Submitted On: October 12, 2015
Accepted On: January 24, 2016

impedance on transmission performance is mainly discussed below.

The original characteristic impedance of microstrip line is:

$$Z_0 = \sqrt{\frac{L_0}{C_0}}. \quad (1)$$

In order to improve the signal transmission performance, several ground-shielded via holes are employed around to enhance impedance matching. Meanwhile, the signal via hole produces the parasitic inductance ΔL. The characteristic impedance of vertical signal via hole becomes:

$$Z = \sqrt{\frac{L_0 + \Delta L}{C_0}}. \quad (2)$$

Therefore, in order to achieve impedance matching, we connect microstrip line to signal via hole through a pad, which introduces the compensation capacitor ΔC.

The characteristic impedance then becomes:

$$Z = \sqrt{\frac{L_0 + \Delta L}{C_0 + \Delta C}} = \sqrt{\frac{L_0}{C_0}} = Z_0. \quad (3)$$

The compensation capacitor ΔC can be directly derivable from the Equation (3):

$$\Delta C = \frac{L_0 + \Delta L - Z_0{}^2 C_0}{Z_0{}^2}. \quad (4)$$

Figure 1 (c) gives the cross sectional view. The parameters of this structure are shown in Table 1. The proposed structures (single and back-to-back) are simulated and carefully tuned in HFSS from 0.3 GHz to 18 GHz. The simulated results of S_{21} and S_{11} are shown in Fig. 2. It can be noticed from Fig. 2 (a) that the insertion loss ($|S_{21}|$) of single vertical interconnection is less than 0.202 dB up to 18 GHz, and the return loss ($|S_{11}|$) is better than 33.79 dB up to 18 GHz. From Fig. 2 (b), it can be observed that $|S_{21}|$ of back-to-back structure is less than 0.33 dB up to 18 GHz, and $|S_{11}|$ is better than 29.9 dB up to 18 GHz.

The improved structure in this letter can achieve better impedance matching and better signal integrity of TEM by the added middle ground plane with the aperture of the anti-pad. In practical manufacturing of LTCC, multi-layer vertical vias are easy to cause dislocation, which can affect signal connectivity. In particular, a disconnected signal via leads to microwave performance deterioration. Therefore, in order to prevent the impact of vertical via dislocation on performance, the surrounding shielded holes and the added middle ground plane with the aperture of the anti-pad are added to ensure better signal integrity of TEM in the event of slight dislocation. Therefore, it is observed that the proposed interconnect structure has better transmission performance. From the result of this work, it can be suggested that this interconnect structure is more suitable for vertical interconnection applications of microwave LTCC integrated circuit and SiP module packages.

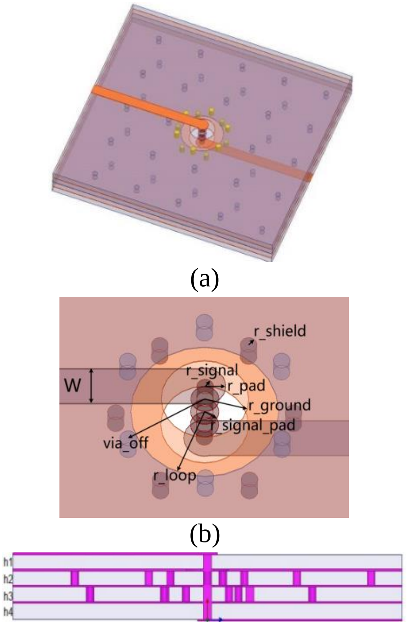

(a)

(b)

(c)

Fig. 1. The overall structure of microstrip-to-microstrip vertical via interconnects: (a) 3D view (single vertical interconnection), (b) coaxial-like via structure, and (c) cross sectional view for via interconnect.

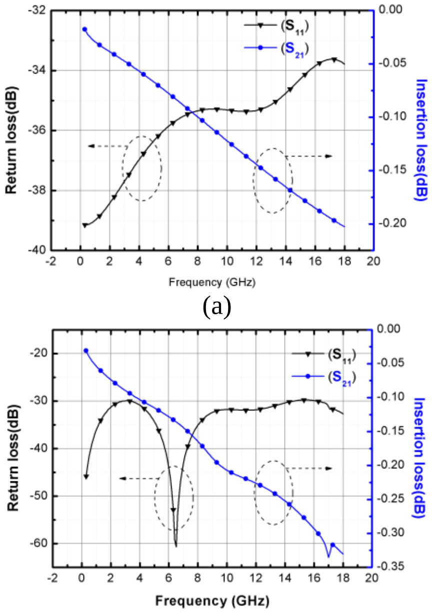

(a)

(b)

Fig. 2. Simulated S_{21} and S_{11} responses of microstrip-to-microstrip vertical interconnect: (a) single vertical transition, and (b) back-to-back structure.

Table 1: The parameters of this structure

Structure Parameters	Quantity	Data (mm)
W	Microstrip width	0.31
r_pad	Radius of pad connecting microstrip line to signal via	0.16
r_signal_pad	Radius of pad for signal via	0.11
r_signal	Radius of signal via	0.065
r_shield	Radius of shield via	0.065
r_ground	Radius of opening in microstrip ground plane	0.34
r_loop	Radius of opening in middle ground plane	0.575
via_off	Distance between shield via and signal via	0.69
h_i	Substrate thickness (h_1, h_2, h_3, h_4)	0.188

III. EQUIVALENT TRANSITION MODEL

An improved equivalent circuit, which is deduced theoretically from reference [7], is used for analyzing vertical via in Fig. 3. The impedance, inductance and capacitance effects of vertical via holes are considered. Hence, it consists of a seven lumped elements pi-equivalent circuit model for the single vertical via interconnect. L_1, C_1 and R_1 denote parasitic inductance, capacitance and resistance of vertical via respectively. R_2 and C_2 represent the parasitic resistance and capacitance between pads of vertical via holes and adjacent ground planes [8-10].

The equivalent model has been optimized and tuned in Agilent ADS on the parameters of the simulation result. The model parameters are extracted and listed in Table 2. The EM-simulated and circuit modeled S-parameter results of the single via interconnection are shown in Fig. 4. As vertical interconnecting via is not an ideal coaxial line, the dispersion increase with the frequency increasing, which leads to non-linear distortion of transmission structure. Therefore, this non-linear distortion increases with frequency and length. From the corresponding results, it can be suggested that the developed circuit model and EM-simulation match almost well.

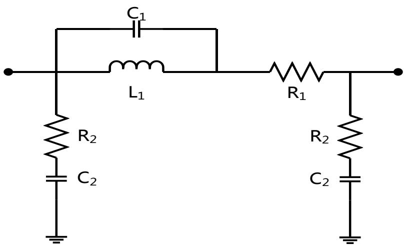

Fig. 3. Equivalent circuit for the proposed single vertical interconnection.

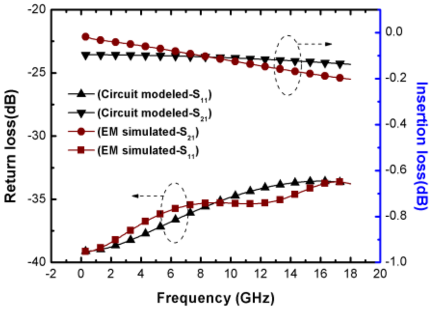

Fig. 4. EM-simulated and equivalent circuit modeled results of the proposed single vertical interconnection.

Table 2: Extracted model parameters

Lumped Parameters	Quantity	Data
C_1(fF)	Parasitic capacitance	85.86
C_2(fF)	Parasitic capacitance	22.38
L_1(pH)	Parasitic inductance	84.36
R_1(Ω)	Resistance	1.12
R_2(Ω)	Resistance	13.63

IV. MEASUREMENT

A back-to-back structure is manufactured for experimental validation as shown in Fig. 5. In Fig. 6, the measurement environment is displayed with a test fixture from Anritsu Model 3680V Universal. After firing, the average thickness of the LTCC substrate and the external conductor are 729 µm and 7 µm separately. The comparison of simulated and measured results has been shown in Fig. 7. For measurement results, the return loss is better than 10 dB, while the insertion loss is less than 1.59 dB in the frequency range of 0.3 GHz to 11.95 GHz. The simulation and measured results shows a discrepancy above 10 GHz. In practical manufacturing, due to fabrication tolerances, such as layer-to-layer alignment tolerance and dignment error of vertical via holes, the measured return loss (S11) of the fabricated model is less than the simulated result. In addition, due to mismachining tolerance of multi-metallized strips and the accuracy error of the shrinkage during the firing process, the measured insertion loss (S21) is larger than the simulated result. However, these factors are difficult to be considered in the simulation.

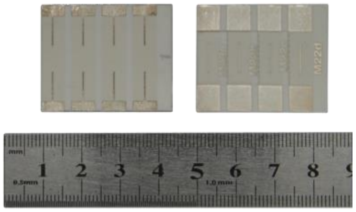

Fig. 5. Photographs of fabricated back-to-back interconnection modules (×4).

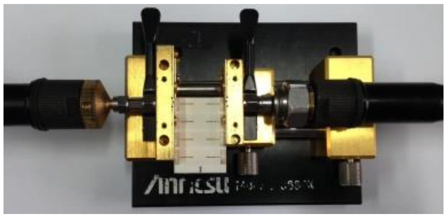

Fig. 6. Photograph of the testing environment.

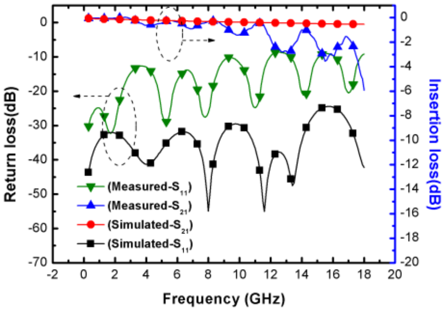

Fig. 7. Comparison of proposed study by simulated and measured results.

V. CONCLUSION

In this letter, a microwave microstrip-to-microstrip vertical via interconnect has been proposed and experimentally validated in LTCC technology. By using the coaxial-like signal via hole and the pad between microstrip and signal via hole, a better impedance matching and less discontinuity are achieved. Also, an improved equivalent circuit is developed for analyzing scattering characteristic of vertical via interconnects. The fabricated back-to-back structure shows an insertion loss of less than 1.59 dB and a return loss of better than 10 dB over 0.3 GHz to 11.95 GHz. This transition structure can be widely used in LTCC SiP module packaging applications.

ACKNOWLEDGMENT

This work was supported by Fundamental Science on EHF Laboratory of University of Electronic Science and Technology of China.

REFERENCES

[1] R. Kulke, et al., "LTCC-multilayer ceramic for wireless and sensor applications," 2001. [Online]. Available: http://www.ltcc.de/downloads/rd/pub/10-doc-plus-engl-2001.pdf.

[2] Q. Y. Guo, X. Y. Zhang, L. Gao, Y. C. Li, and J. X. Chen, "Microwave and millimeter-wave LTCC filters using discriminating coupling for mode suppression," *IEEE Transactions on Components, Packag. and Manufacturing Technol.*, no. 99, pp. 1-10, 2016.

[3] H. Chu, J.-X. Chen, and Y.-X. Guo, "A compact artificial transmission line structure using LTCC technology and its applications," *IEEE MTT-S Int. Microw. Workshop Series on Advanced Materials and Processes for RF and THz Applications*, pp. 1-3, 2015.

[4] Y. Zhou, A. Sun, J. Zhou, and Y. Shen, "A compact multi-channel receiver front-end using SiP integration technology on LTCC substrate for wireless communications," *Int. Conf. on Wireless Communications & Signal Processing*, pp. 1-5, 2015.

[5] I. Wolff, "From antennas to microwave systems-LTCC as an integration technology for space applications," *3rd Eur. Antennas Propag. Conf.*, pp. 3-8, Mar. 2009.

[6] A. Pham, et al., "Development of millimeter wave multi-layer organic based MCM technology," *IEEE MTT-S Int. Microw. Symp. Dig.*, pp. 1091-1094, June 1998.

[7] Y.-S. Bang, J.-M. Kim, J.-M. Kim, Y.-K. Kim, and Y.-H. Jang, "LTCC-based vertical via interconnects for RF MEMS packaging," *Microw. Opt. Technol. Lett.*, vol. 52, no. 2, Feb. 2010.

[8] H.-H. Jhuang and T.-W. Huang, "Design for electrical performance of wideband multilayer LTCC microstrip-to-stripline transition," *Electron. Packag. Tech. Conf.*, pp. 506-509, 2004.

[9] C. L. N. Pavan and K. C. J. Raju, "Vertical interconnect modeling between GCPWs in LTCC technology," *Asia Pacific Conf. on Postgraduate Research in Microelectronics and Electron.*, pp. 211-213, 2012.

[10] E. Pillai, F. Rostan, and W. Wiesbeck, "Derivation of equivalent circuits for via holes from full wave models," *Electron. Lett.*, vol. 29, no. 11, pp. 1026-1028, 1993.

Metamaterial Inspired Square Ring Monopole Antenna for WLAN Applications

S. Imaculate Rosaline and S. Raghavan

Department of Electronics and Communication Engineering
National Institute of Technology, Tiruchirappalli, India
imaculaterosaline@gmail.com, raghavan@nitt.edu

Abstract **─** This paper describes the design of a compact dual band monopole antenna using a metamaterial inspired split ring structure for WLAN (2.4/5.2/5.5 GHz) applications. The antenna is printed on a 20x20x0.8 mm^3 FR-4 substrate. It consists of two concentric square rings with a partial ground plane and is fed by a microstrip line. A split in the outer ring is introduced to induce magnetic resonance which in turn yields a narrow lower band resonance at 2.4 GHz. The position of the split in the ring plays a vital role in inducing the magnetic resonance. The extraction of negative permeability of the ring structure with and without the split is discussed to verify the metamaterial property existence. A prototype of the proposed structure is fabricated and the measured results comply greatly with the simulated results. The antenna has consistent radiation pattern over all the working region.

Index Terms **─** Metamaterial, monopole, negative permeability, split ring, WLAN.

I. INTRODUCTION

Wireless Local Area Network (WLAN), based on IEEE 802.11 standard operates in the 2.45 (2.4-2.48) GHz, 5.2 (5.15 -5.35) GHz and 5.8 (5.75 - 5.825) GHz frequencies. Several design of antennas capable of covering both these frequency bands are discussed in the recent past. Among the variety of antennas proposed, printed monopoles serve as a good choice because of their compactness, efficiency and easy integration with other microwave integrated circuits. Multi branched radiators [1, 2], slotted monopoles [3 - 5], meander monopoles [6], fractal shapes [7] are few among them to obtain dual band operation in the WLAN 2.5/5.2/5.8 GHz range. Recently, electromagnetic metamaterial inspired structures like split ring resonators and complementary split ring resonators are used in the design of antennas. Split ring monopole antenna proposed in [8] has impedance matching problem in the lower WLAN band, whereas the dual band antennas with CSRRs [9] and triangular split ring resonators (SRRs) [10] has larger dimensions. Recently, in [11], multiband metamaterial loaded monopole antenna is reported for WLAN/ WiMAX applications. But, yet the overall dimension of these antennas are large compared with the proposed one as shown in Table 1 below. Also, unlike these antenna analysis, this paper emphasizes on the role of metamaterial property (negative permeability) in antenna design.

Table 1: Dimensions of multiband antennas

Ref.	Dimensions, L x W (mm^2)
[8]	20 x 32
[9]	34 x 30
[10]	40 x 35
[11]	45 x 40
Proposed antenna	20 x 20

In this paper, a compact dual band monopole utilizing metamaterial inspired split ring structure is discussed. The magnetic resonance of the split ring structure offers a narrow lower band resonance at 2.4 GHz. The proposed geometry is very simple with good resonant and radiation characteristics, making it a good choice for commercial use.

II. PROPOSED ANTENNA DESIGN

The evolution of the proposed split ring radiating antenna is shown in Fig. 1. Here, configuration A shows a square ring monopole of side length 10 mm. It is fed by a 5x0.8 mm^2, microstrip line. In configuration B, a concentric inner ring is introduced to achieve resonance at the higher frequency band (5.5 GHz).

Finally, as shown in configuration C, a split is introduced along the horizontal arm of the outer ring to induce magnetic resonance and in turn yield a second lower band resonance. The antenna is printed on a 20x20x0.8 mm^3 FR-4 substrate with a relative dielectric constant of 4.4 and loss tangent of 0.002. A detailed layout of the proposed antenna is shown in Fig. 2 along with its side view and its dimensions are listed in Table 2. Photograph of the proposed structure is shown in Fig. 3.

Submitted On: November 11, 2015
Accepted On: February 20, 2016

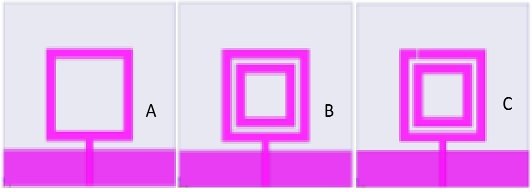

Fig. 1. Evolution of the proposed antenna.

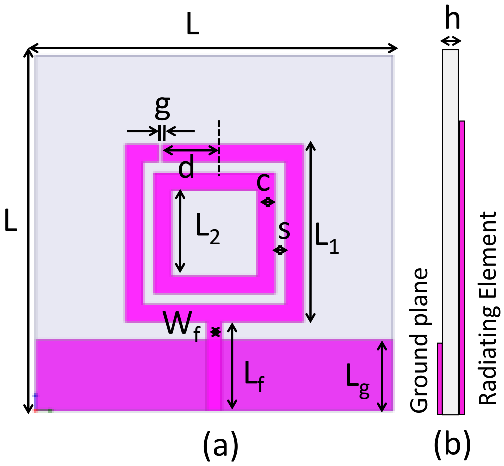

Fig. 2. Geometry of the proposed antenna: (a) top view and (b) side view.

Table 2: Dimensions of the proposed antenna

Parameter	Dimension (mm)	Parameter	Dimension (mm)
L	20	L_1	10
L_2	4.8	L_f	5
W_f	0.8	L_g	4
g	0.2	c	1
d	3	s	0.6
h	0.8		

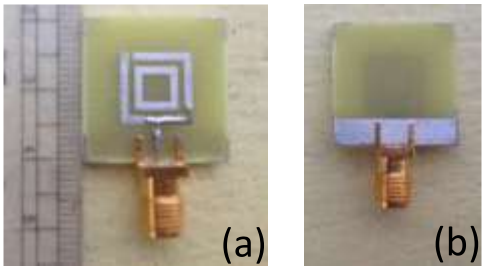

Fig. 3. Photograph of the proposed dual band antenna: (a) top view and (b) bottom view.

III. SIMULATION RESULTS

Simulations are performed using the Ansoft High Frequency Structure Simulator (HFSS) V.15.0 commercial software package. Figure 4 shows the simulated reflection coefficient characteristics of the three configurations shown in Fig. 1. Configuration A shows resonance around 6 GHz for $W_f = 0.8$ mm. When the inner concentric ring is introduced as shown in configuration B, the impedance matching at 6 GHz is improved, since the inner ring by itself exhibits a quarter wavelength resonance for the radii of 6.8 mm. Now, when the split is introduced along the outer ring (configuration C), the current along this path gets perturbed, and leads to a lower band resonance around 2.4 GHz. Figure 5 shows the parametric study on W_f for configuration B. It is inferred that when W_f is 1.6 mm, resonance around 4 GHz is observed and when W_f is 0.8 mm, resonance around 6 GHz is observed. Hence, for fabrication, $W_f = 0.8$ mm is chosen. The proposed structure shows a dual band resonance centred at 2.4 GHz, and 5.5 GHz, with -10 dB impedance bandwidth of 150 MHz (2.35 – 2.5 GHz) and 1230 MHz (4.9 – 6.13 GHz). Here, the position of the split from its centre (d) plays an important role in determining the lower resonant band. This is validated by performing a parametric study. Figure 6 shows the parametric study on the position 'd' of the split ring from the centre. It is noted that, when the split is present at the centre, there is no lower band resonance and when the split is moved on either side at a distance of 1 mm, 2 mm, etc. from the centre, a narrow lower band resonance around 2.4 GHz is inferred. This is due to the induced charge concentration around the split gap. Simulated surface current distribution of the proposed antenna at 2.4 GHz and 5.5 GHz are shown in Figs. 7 (a) and (b). It is inferred that, for 2.4 GHz band, the current is dense along the longest arm of the outer ring and for 5.5 GHz, the current is distributed along the outer ring. The coupling of current to the inner ring can also be noticed. Figure 7 (c) shows the simulated electric field distribution at 2.4 GHz. A dense charge distribution around the split gap is inferred.

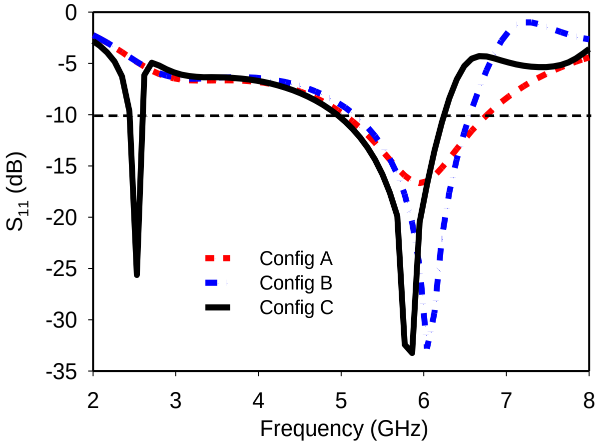

Fig. 4. Simulated input reflection coefficient characteristics of configuration A, B and C.

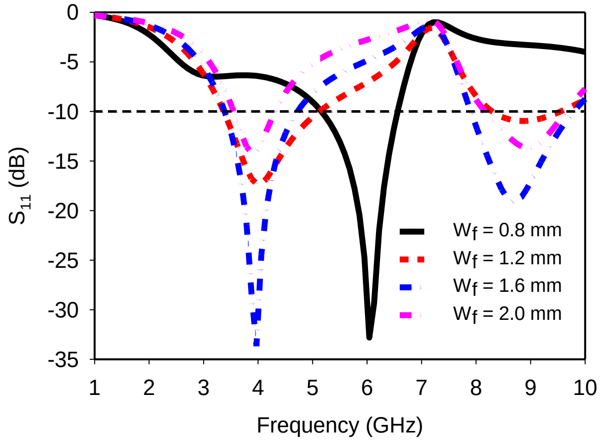

Fig. 5. Simulated input reflection coefficient characteristics of configuration B for various feed width Wf.

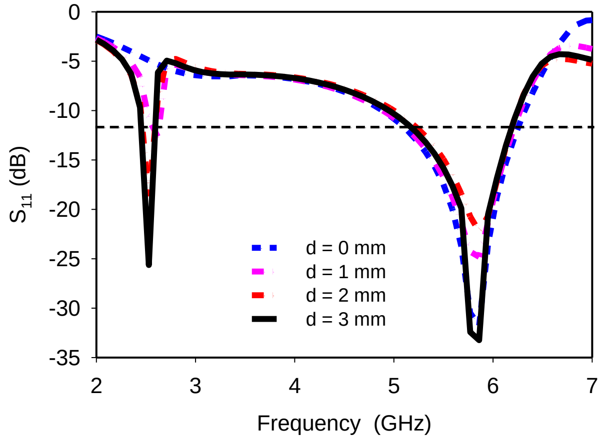

Fig. 6. Simulated input reflection coefficient characteristics of configuration C for various distance of the split, d, from the center.

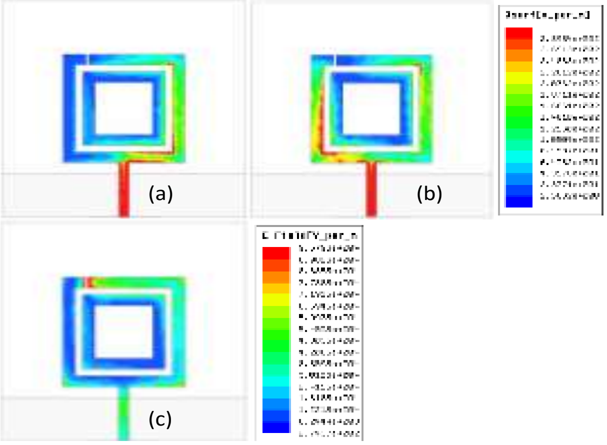

Fig. 7. Simulated surface current distribution of the proposed antenna at: (a) 2.4 GHz, (b) 5.5 GHz, and (c) simulated electric field distribution at 2.4 GHz.

IV. MEASUREMENT RESULTS

The return loss characteristics are measured using a vector network analyser. Figure 8 shows the simulated and measured reflection coefficient characteristics of the proposed antenna. The measured data exhibits a dual band resonance at 2.4 GHz, and 5.5 GHz, with -10 dB impedance bandwidth of 150 MHz (2.35 – 2.5 GHz) and 1600 MHz (4.9 – 6.5 GHz). The measured results greatly comply with the simulated results in the 2.4 GHz band; however, a discrepancy in the higher operational band at 5.5 GHz is observed. This may be attributed to fabrication tolerance and thick soldering of SMA connector. Figure 9 shows the measured radiation pattern of the proposed antenna at 2.4 GHz, 5.2 GHz and 5.8 GHz. A consistent omnidirectional pattern is observed in the H plane and a bidirectional pattern is observed in the E plane over all the operating region. A peak gain of 1.6 dBi and 2.8 dBi are inferred around 2.4 GHz and 5.5 GHz during measurement. Thus, the radiation and resonant behaviour of the antenna are found satisfactory making the antenna suitable for wireless communication devices.

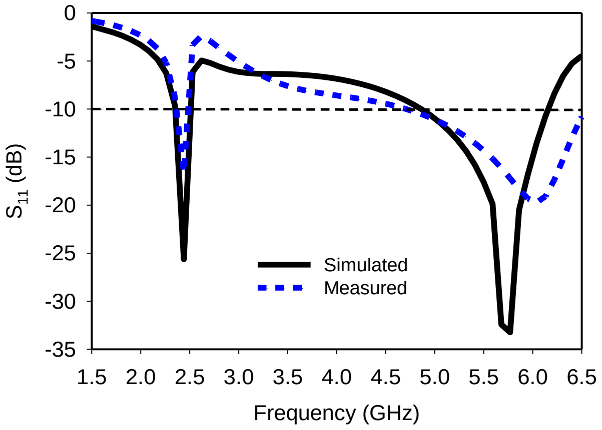

Fig. 8. Simulated and measured input reflection coefficient characteristics of the proposed antenna.

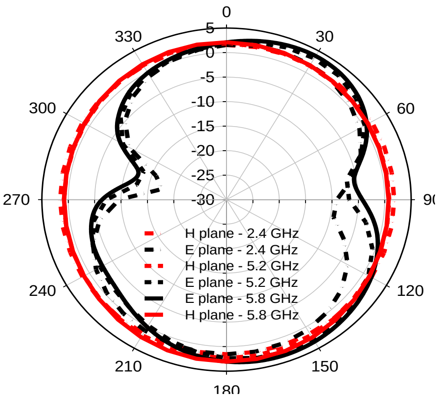

Fig. 9. Measured H plane and E plane pattern of the proposed antenna at 2.4 GHz, 5.2 GHz and5.8 GHz.

V. SPLIT RING ANALYSIS

The radiating element by itself is a split ring structure. The structure is analysed using the classic waveguide theory approach in which the structure is placed inside a waveguide and an EM wave is passed through one of its ports and measured through the other port. The transmission and reflection coefficients are noted and from which the effective material parameters (permeability and permittivity) are extracted [12]. Figure 10 shows the real parts of extracted effective permeability values for the two split ring structure with and without the split gap. It is inferred that the permeability is negative around 2.4 GHz for the structure with split and a constant permeability for the structure without the split, which confirms the metamaterial property existence.

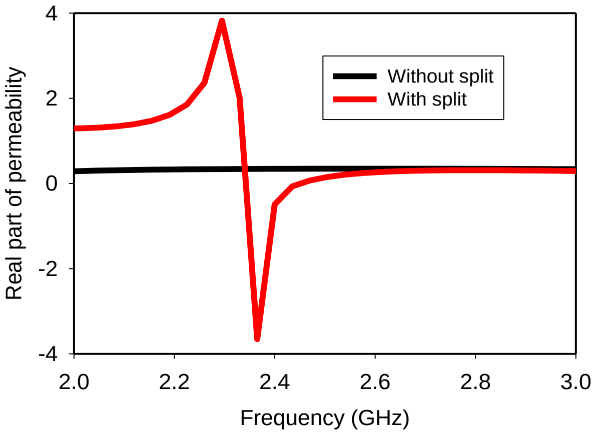

Fig. 10. Real part of extracted effective permeability of the two split ring structures.

VI. CONCLUSION

A dual band monopole antenna suitable for WLAN 2.4/5.5 GHz applications is presented in this paper. The antenna makes use of a metamaterial inspired split ring structure for achieving the dual band resonance. The antenna geometry is very simple and also compact making mass production easy. The radiation pattern and gain are consistent over all the operating bands making the proposed antenna a good choice for wireless applications.

REFERENCES

[1] Y. Xu, Y.-C. Jiao, and Y.-C. Luan, “Compact CPW-fed printed monopole antenna with triple band characteristics for WLAN/WiMAX applications,” *Electron Lett.*, vol. 48, pp. 1519-1520, 2012.

[2] X. L. Sun, L. Liu, S. W. Cheung, and T. I. Yuk, “Dual-band antenna with compact radiator for 2.4/5.2/5.8 GHz WLAN applications,” *IEEE Trans. Ant. P*, vol. 60, pp. 5924-5931, 2012.

[3] W.-C. Liua, C.-M. Wua, and N.-C. Chu, “A compact low profile dual-band antenna for WLAN and WAVE applications,” *AEU Int. J. Electron. C*, vol. 66, pp. 467-471, 2012.

[4] C.-Y. Huang and E.-Z. Yu, “A slot monopole antenna for dual band WLAN applications,” *IEEE Antennas Wireless Propag. Lett.*, vol. 10, pp. 500-502, 2011.

[5] X.-Q. Zhang, Y.-C. Jiao, and W.-H. Wang, “Compact wide tri-band slot antenna for WLAN/WiMAX applications,” *Electron. Lett.*, vol. 48, pp. 64-65, 2012.

[6] H.-Y. Chien, C.-Y.-D. Sim, and C.-H. Lee, “Dual band meander monopole antenna for WLAN operation in laptop computer,” *IEEE Antennas Wireless Propag. Lett.*, vol. 12, pp. 694-697, 2013.

[7] R. Ghatak, R. K. Mishra, and D. R. Poddar, “Perturbed Sierpinski carpet antenna with CPW feed for IEEE 802.11 a/b WLAN application,” *IEEE Antennas Wireless Propag. Lett.*, vol. 7, pp. 742-744, 2008.

[8] S. C. Basaran and Y. E. Erdemli, “A dual band split ring monopole antenna for WLAN applications,” *Microw. Opt. Technol. Lett.*, vol. 51, pp. 2685-2688, 2009.

[9] S. C. Basaran, U. Olgun, and K. Sertel, “Multiband monopole antenna with complementary split ring resonators for WLAN and WiMAX applications,” *Electron. Lett.*, vol. 49, pp. 636-638, 2013.

[10] K. Yang, H. Wang, Z. Lei, Y. Xie, and H. Lai, “CPW-fed slot antenna with triangular SRR terminated feed line for WLAN/WiMAX applications,” *Electron. Lett.*, vol. 47, pp. 685-686, 2011.

[11] H. He, Y. Liu, S. Zhang, and S. Gong “Multiband metamaterial-loaded monopole antenna for WLAN/WiMAX applications,” *IEEE Antennas Wireless Propag. Lett.*, vol. 14, pp. 662-665, 2015.

[12] D. R. Smith, S. Schultz, P. Markos, and C. M. Soukoulis, “Determination of effective permittivity and permeability of metamaterials from reflection and transmission coefficients,” *Phys. Rev. B*, vol. 65, pp. 195104-195109, 2002.

Mutual Coupling Characterization of Ultra-Wideband U-Slot Microstrip Patch Array Antennas

Mohamed M. Elsewe and Deb Chatterjee

Computer Science & Electrical Engineering Department
University of Missouri – Kansas City, Kansas City, MO 64110, USA
mme0f0@mail.umkc.edu, chatd@umkc.edu

Abstract **─** Ultra-wideband (UWB) phased arrays are increasingly used in radar and medical applications. Mutual coupling reduction between the phased array elements is critical in achieving good scan bandwidth. This study investigates the mutual coupling of a UWB U-slot microstrip patch 2-element array to find the patch orientation and U-slot topology with the least mutual coupling. Electromagnetic (EM) simulation results indicate that, for $\varepsilon_r = 2.2$ substrate, diamond patch orientation with opposite U-slot topology has the least coupling between the array elements. Results also indicate that the current density distribution on the microstrip patch has an effect on mutual coupling between the array elements. Results show good agreement between MoM and FEM EM solvers.

Index Terms **─** Arrays, FEM, L-probe, microstrip, MoM, mutual coupling, U-slot, UWB.

I. INTRODUCTION

UWB scanning phased arrays are finding increasing use in wireless communication and medical applications [1, 2]. Scan blindness due to surface wave excitations could reduce the scan bandwidth range [3]. By reducing the mutual coupling between array elements, the scan blindness effects will be reduced [3]. In this study, the mutual coupling of a UWB U-slot microstrip patch 2-element array is investigated to find the patch orientation and U-slot topology with the least mutual coupling.

U-slot patch antennas are a class of UWB microstrip patch antennas. Several feeding structure designs for the U-slot patch antenna are proposed in the literature [4, 5]. The L-shaped probe feeding structure has led to further improved impedance bandwidth for the U-slot patch antenna [5]. Moreover, its simple structure and low material and production cost [5] make it an attractive feeding method for the U-slot microstrip patch antenna.

Previous work [6, 7] analyzed the mutual coupling between the U-slot microstrip array elements using the vertical probe feeding structure. The study in [8] aimed to characterize the mutual coupling of a U-slot microstrip 2-element array for the L-probe feeding structure compared to the vertical probe feeding structure using different U-slot topologies for $\varepsilon_r = 2.2$ substrate. This paper aims to extend this study by characterizing the mutual coupling of an L-probe-fed U-slot microstrip 2-element array using different patch orientations and U-slot topologies for $\varepsilon_r = 2.2$ substrate.

II. DESCRIPTION OF MODEL

The U-slot microstrip patch antenna array is simulated and analyzed using the Method of Moments (MoM) solver in the commercially available EM simulation package, FEKO. The FEKO MoM results are validated by another EM simulation package, HFSS, which is based on the Finite Element Method (FEM).

The simulated U-slot microstrip patch antenna geometry is shown in Fig. 1. The RT/Duroid 5880 substrate material with $\varepsilon_r = 2.2$ and $\tan(\delta) = 0.0009$ is used. The method of dimensional invariance described in [9] is used to realize the U-slot antenna patch dimensions, shown in Table 1, for a 2.4 GHz design frequency. Experimental validation of the method of dimensional invariance is reported in earlier work [7].

Several simulation optimization runs were performed to arrive at the substrate height and probe position which yield best bandwidth. In FEKO, infinite substrate and ground is assumed. In HFSS, the substrate and ground (W_g and L_g) dimensions are extended by $\lambda/2$, where λ corresponds to lower bandwidth frequency, from the edge of the patch to simulate an infinite substrate and ground. In HFSS, a radiation air box boundary which is $\lambda/2$, where λ corresponds to the lower bandwidth frequency, above the patch is used. A 50-ohm coaxial feed line is used to feed the L-probe. The different 2-element patch orientations and U-slot topologies simulated are shown in Fig. 2. The inter-element spacing between the patch edges is taken to be approximately $\lambda/4$. For the diamond patch orientations,

Submitted On: December 12, 2015
Accepted On: January 31, 2016

the patches are rotated by 45°.

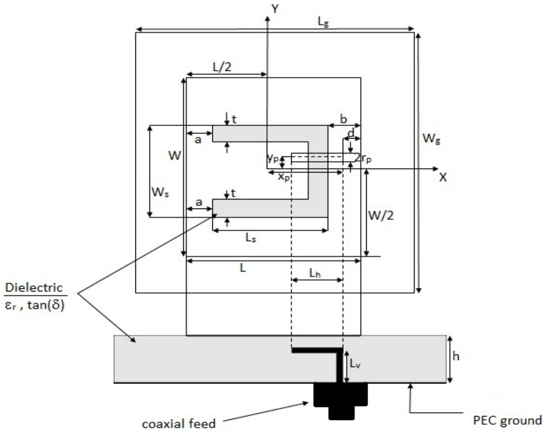

Fig. 1. Geometry of L-shaped, probe-fed, rectangular, U-slot, patch microstrip antenna.

Table 1: U-slot microstrip patch antenna dimensions

a	5.17 mm	W_s	18.09 mm	d	3 mm
b	5.17 mm	r_p	1 mm	h	14 mm
W	46.53 mm	x_p	13.8 mm	L_v	10 mm
L	33.6 mm	y_p	-1 mm	L_h	12 mm
t	2.6 mm				

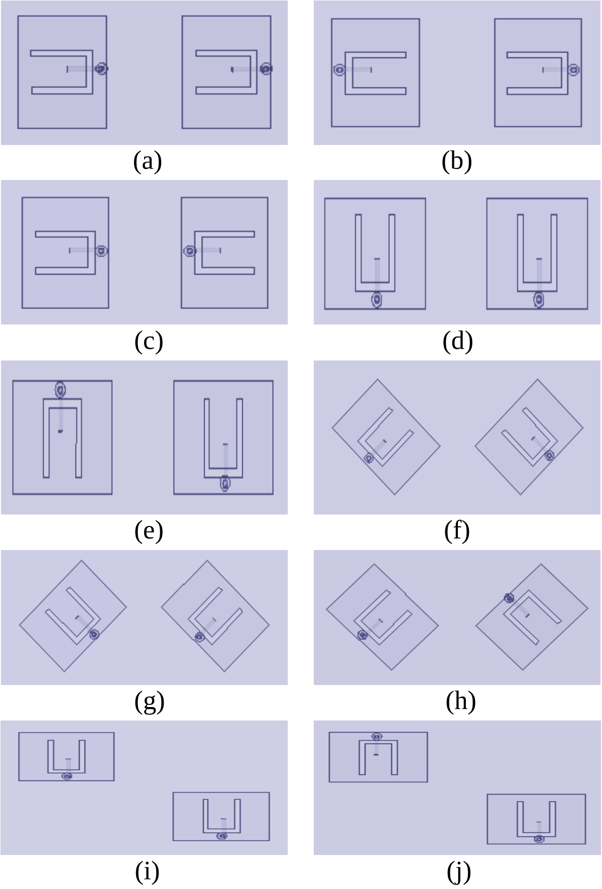
(a) (b) (c) (d) (e) (f) (g) (h) (i) (j)

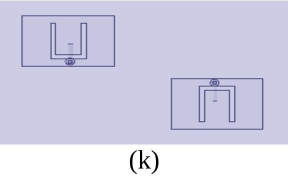
(k)

Fig. 2. Variations of U-slot topologies and patch orientations in a 2-element array: (a-c) E-plane patch orientation, (d-e) H-plane patch orientation, (f-h) diamond patch orientation, and (i-k) Diagonal patch orientation.

III. RESULTS AND DISCUSSION

In [10], the bandwidth for a single-element L-probe-fed U-slot microstrip patch antenna with ε_r = 2.2 substrate was found to be between 1.8 GHz and 3 GHz. Figure 3 shows the E-plane coupling between two L-probe-fed U-slot patch elements for 3 different U-slot topologies over the 2-3 GHz bandwidth. HFSS and FEKO simulation results indicate that topology (a) has the lowest mutual coupling in the 20-27 dB range, and topology (c) has the highest mutual coupling. Figure 4 shows the H-plane coupling between two L-probe-fed U-slot patch elements for 2 different U-slot topologies. Results indicate that topology (e) has the lowest mutual coupling in the 20-25 dB range. Figure 5 shows the diamond patch orientation coupling between two L-probe-fed U-slot patch elements for 3 different U-slot topologies. Results indicate that the opposite U-slot topology (h) has the lowest mutual coupling in the 25-45 dB range, and topology (g) has the highest mutual coupling. Figure 6 shows the diagonal patch orientation coupling between two L-probe-fed U-slot patch elements for 3 different U-slot topologies. Results indicate that no particular topology has the highest or lowest mutual coupling throughout the entire bandwidth; however, topology (j) has the lowest mutual coupling in half of the bandwidth in the 20-40 dB range. In Figs. 3-6, HFSS and FEKO results show good agreement.

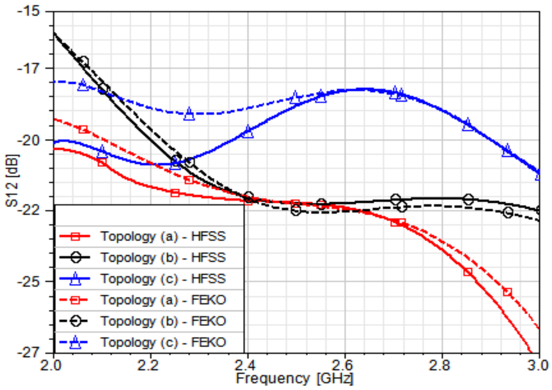

Fig. 3. E-plane patch orientation coupling for different U-slot topologies.

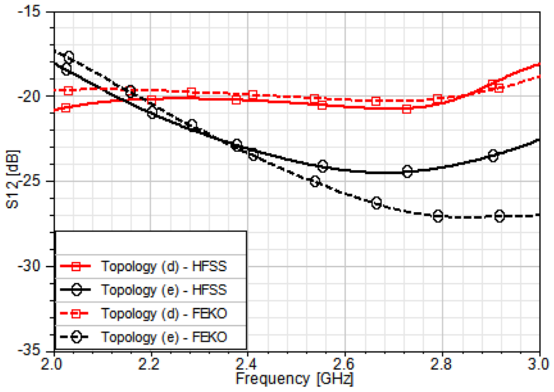

Fig. 4. H-plane patch orientation coupling for different U-slot topologies.

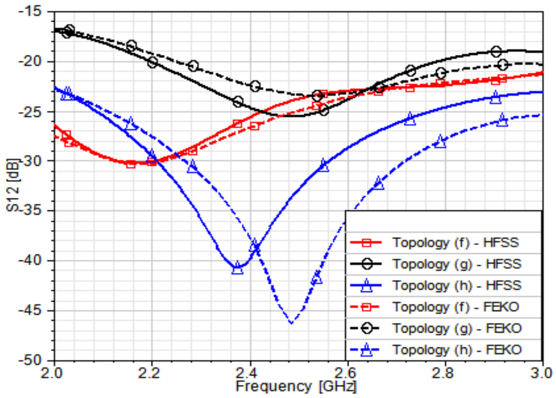

Fig. 5. Diamond patch orientation coupling for different U-slot topologies.

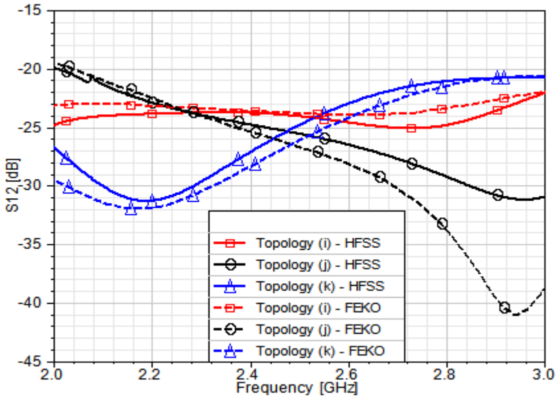

Fig. 6. Diagonal patch orientation coupling for different U-slot topologies.

Figures 7 and 8 show the current density distribution at 2.4 GHz for the U-slot topology, (h) with the least mutual coupling and the U-slot topology (c) with the highest mutual coupling, respectively. As seen in both figures more current density is concentrated around the base side of the U-slot, underneath which the L-probe feed is located. In Fig. 7, the two U-slot bases are farther apart from each other than in Fig. 8. This explains the lower mutual coupling in U-slot topology (h). Similarly, it is observed in the H-plane patch orientation that the U-slot topology (e) has less mutual coupling than U-slot topology (d) mainly because the U-slot base sides, where more current density is present, are farther apart in the case of U-slot topology (e). Also, in the diamond patch orientation, the U-slot topology (g) has the highest mutual coupling because the two U-slot base sides are closest to each other.

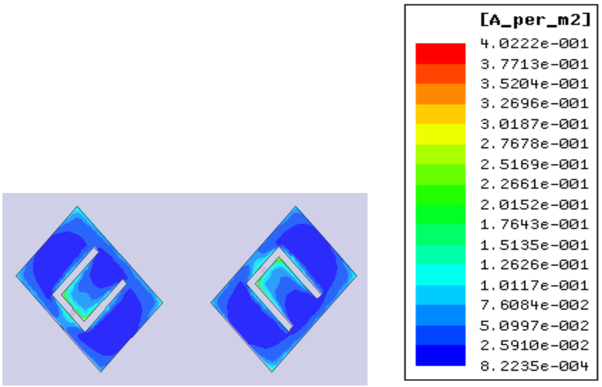

Fig. 7. Current density distribution in Diamond patch orientation for U-slot topology (h) at 2.4 GHz.

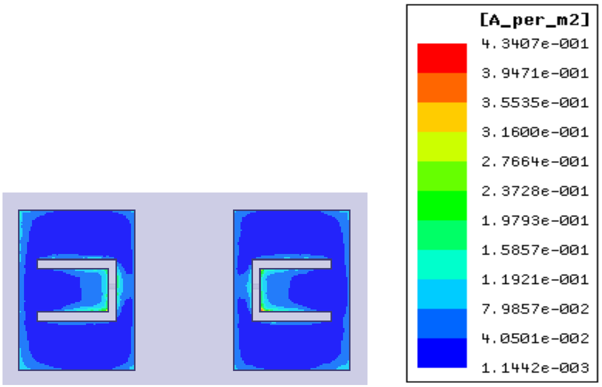

Fig. 8. Current density distribution in E-plane patch orientation for U-slot topology (c) at 2.4 GHz.

IV. CONCLUSION

In this paper, the evaluation of the mutual coupling of an L-probe-fed U-slot microstrip patch 2-element array using different patch orientations and U-slot topologies for $\varepsilon_r = 2.2$ substrate is presented. HFSS and FEKO simulation results show good agreement and indicate that the current density distribution on the microstrip patch has an effect on mutual coupling between the array elements. Results also indicate that the diamond patch orientation with opposite U-slot topology has the least coupling between the array elements. Future work will examine the scan bandwidth of such patch orientation and U-slot topology in a planar array. Also, the same study will be performed for higher substrate permittivities.

REFERENCES

[1] P. T. Nguyen, A. Abbosh, and S. Crozier, "Microwave hyperthermia for breast cancer treatment using electromagnetic and thermal focusing tested on realistic breast models and antenna arrays," *IEEE Transactions on Antennas and Propagation*, vol. 63, no. 10, pp. 4426-4434, October 2015.

[2] T. Lambard, O. Lafond, M. Himdi, H. Jeuland, S. Bolioli, and L. Le Coq, "Ka-band phased array antenna for high-data-rate SATCOM," *IEEE Antennas and Wireless Propagation Letters*, vol. 11, pp. 256-259, 2012.

[3] W. L. Stutzman and G. A. Thiele, *Antenna Theory and Design*, 3rd Edition, Wiley, New York, pp. 319, 2012.

[4] K. F. Lee, S. L. S. Yang, A. A. Kishk, and K. M. Luk, "The versatile U-slot patch antenna," *IEEE Antennas and Propagation Magazine*, vol. 52, no. 1, pp. 71-88, February 2010.

[5] K. M. Luk, K. F. Lee, and H. W. Lai, "Development of wideband L-Probe couple patch antenna," *Applied Computational Electromagnetics Society (ACES) Journal*, vol. 22, no. 1, pp. 88-96, March 2007.

[6] D. Chatterjee, "Numerical modeling of scan behavior of finite planar arrays of wideband U-slot and rectangular microstrip patch elements," *Proceedings of IEEE International Symposium on Phased Array Systems and Technology*, Boston, MA, pp. 323-328, October 14-17, 2003.

[7] R. D. Hofer, D. E. Oliver, and D. Chatterjee, "Analysis of U-slot, microstrip phased array radiator elements on electrically thick substrates," *IEEE Antennas and Propagation Society International Symposium*, Honolulu, HI, pp. 3648-3651, June 9-15, 2007.

[8] M. M. Elsewe, V. K. Dandu, and D. Chatterjee, "Assessment of computational fidelity of MoM and FEM solvers for characterizing a class of UWB microstrip antennas: 2-element case," *29th Annual Review of Progress in Applied Computational Electromagnetics*, Monterey, CA, pp. 399-404, March 24-28, 2013.

[9] V. Natarajan and D. Chatterjee, "An empirical approach for design of wideband, probe-fed, U-slot microstrip patch antennas on single-layer, infinite, grounded substrates," *Applied Computational Electromagnetics Society (ACES) Journal*, vol. 18, no. 3, pp. 191-201, November 2003.

[10] M. M. Elsewe, V. K. Dandu, and D. Chatterjee, "Ultra-wideband low profile, U-slot microstrip patch antennas: L-probe feed design guidelines," *Applied Computational Electromagnetics Society (ACES) Journal*, submitted October 2015.